Computational and Phenomenological Modeling of Atomic-Scale Transport Processes in Glasses and Glass-Forming Liquids

by

M. Cameran Beg

A dissertation submitted in partial fulfillment
of the requirements for the degree of
Doctor of Philosophy
(Chemical Engineering)
in the University of Michigan
2023

Doctoral Committee:

Professor John Kieffer, Chair
Professor Bryan R. Goldsmith
Assistant Professor Jovan Kamcev
Associate Professor Liang Qi

Mirza Cameran Beg

cbeg@umich.edu

ORCID iD: 0000-0002-8594-0864

Dedication

To my wife, Meagan.

To my parents, Sonya and Mirza.

To my siblings, Amber and Adam.

Thank you all for the love, support, encouragement, and, when necessary, welcomed distraction

throughout this once-in-a-lifetime experience.

Table of Contents

List of Figures

Abstract

This work focuses on the computational investigation and phenomenological model development of atomic-scale transport properties in glasses and glass forming liquids. Specifically, we study ion diffusion and viscous processes as they arise from phenomenologically similar elementary mechanisms. A greater understanding of ionic mobility in glasses can elucidate important materials design criteria for the development of solid-state electrolyte batteries while improvements in viscosity modeling of glass formers is vital to advancing the development and manufacturing of novel glasses. These endeavors work toward providing insight into essential characteristics of the glass transition phenomenon.

We begin with a study of diffusivity in a simple two-component model solid electrolyte using molecular dynamics (MD) simulations. This model system is composed of lattice elements, forming a covalent support structure for solute particles that exhibit weaker non-bonding interactions with the network. The solute species size is systematically varied, while the network atoms are unchanged and a constant system volume is maintained. The atomic mobility increases by orders of magnitude in conjunction with cohesive rupture between solute and network and enhanced anharmonicity, as revealed by analyzing the internal pressure, compressibility, and vibrational spectra as a function of solute size. This finding inspires using ion-exchange to enhance ionic mobility in oxide glasses. Replacing cesium in a MD simulation-generated melt-quench cesium silicate glass with the smaller sodium cation results in a 4.5 to 6-fold increase in diffusivity compared to the melt-quenched sodium silicate control. This increase results from a

greater free volume of the ion-exchanged glass. Similarly, subjecting the control glass to isotropic volumetric strains, a sodium mobility increase is observed, peaking at 25% strain, which corresponds to the tensile limit of the simulated glass. Expansion causes the potential energy topography to flatten, allowing sodium to readily access transition pathways between neighboring sites. Greater strain causes cavitation of the silica network, creating non-traversable gaps for sodium migration.

A hallmark of thermally activated transport processes in glass forming materials is the non-Arrhenius temperature dependence above T_g. This applies to ionic conductivity and viscoelasticity. Conjecturing that this behavior is rooted in a variable free energy topography associated with structural changes occurring in a system upon traversing the glass transition regime, we juxtapose the complex mechanical modulus of a sodium borate melt measured at GHz frequencies and its zero Hz viscosity. Modifying the Maxwell-Wiechert model to account for a temperature dependent activation free energy, the high-frequency and steady-state quantities are perfectly reconcilable with one another, thus validating the underlying atomic scale mechanisms. Expanding on this framework, we develop a workflow for analyzing steady-state viscosity data of 847 oxide glass formers using our new variable activation free energy (VAFE) model in case the adiabatic complex mechanical modulus is not available. We compare the performance of the VAFE model with those of the established VFT and MYEGA equations and find our model to be more robust to extrapolation and possessing more reasonable behavior in the infinite-temperature. Furthermore, our model encodes a relationship between fragility and the temperature-dependent change in the ground-state potential energy associated with structural changes in glass formers between the glassy and liquid states. It also allows one to estimate the

number of atoms onto which the activation energy is imparted per elementary viscous dissipation event.

Chapter 1 Introduction

1.1 Atomic-Scale Transport Processes in Glass Forming Systems

1.1.1 Ionic Mobility and Solid-State Electrolytes

Efficient, on-demand energy storage in the form of battery technology has become vital to

society, and its importance will only increase with the ever-growing prevalence of portable

electronic devices, the trend towards hybrid electric and fully electric vehicles, and the push for

renewable energy resources.[1,2] With respect to the latter, solar and wind energy are both variable

power sources and cannot be relied upon to consistently match power supply to demand without

grid-scale energy storage systems. Grid load leveling can be used to shift electrical energy

supply requirements from peak to off-peak times.[1,3] This means that energy generated beyond

demand can be stored in batteries and released later to supplement supply when demands are

high. Battery technology in support of these endeavors provides a clear path toward the reduction

of environmental damage, greenhouse gas emissions, and depletion of fossil fuels.[4] The

development of solid-state electrolytes is key to achieving the energy and power densities for

batteries required to outcompete gasoline and diesel powered vehicles.[5] The increased energy

density results in an improved travel range, while the increased power density enables rapid

recharging, approaching refueling rates of gasoline vehicles. Similarly important are the

improvements to battery capacity, charging rate, lifetime, and safety afforded to the smartphones,

smartwatches, tablets, laptops, and other consumer electronics. These devices have come to be

extensions of ourselves, providing us with instant access to communication, information,

navigation, entertainment, and more.

Solid-state electrolytes (SSE) are projected to replace the liquid electrolyte technology that is prevalent today. Batteries based on SSE do not bear the same fire and explosion hazards associated with organic liquid electrolytes that can leak out of the cell and catch fire or simply combust due to overheating during operation or as the result of a short circuit.[5,6] While aqueous electrolytes consisting of metal ionic salts dissolved in water also mitigate this explosion hazard, possess a high ionic conductivity, and are economically favorable to produce, these electrolytes are excluded from use in rechargeable high energy density batteries due to the inherently low electrochemical window of 1.23 volts at which water decomposes.[7] SSE boast a larger electrochemical stability window (typically on the order of 5 volts) and higher achievable energy densities than those of liquid electrolyte batteries.[4] All liquid electrolyte batteries are subject to dendrite growth on the anode that occurs over many charge-discharge cycles, which results in efficiency loss through polarization and eventual failure via short circuit. The rigid structure of solid electrolytes greatly increases their resistance to dendritic penetration.[8] Unfortunately, mechanical stiffness tends to counteract atomic mobility, and hence, finding ways to increase the ionic conductivity in SSE is a primary research focus.

Solid-state electrolytes can be broadly categorized into three groups: inorganic solid electrolytes (ISE), solid polymer electrolytes (SPE), and composite solid electrolytes (CSE). ISE are typically composed of an inorganic network cation with either an oxide, sulfide, or nitride network anion, include a conducting network modifier, such as Li_2O, and may also contain various intermediates and dopants. ISE typically have lithium transference numbers near unity largely because the anion counter to lithium is immobilized by being part of the network structure. The lithium transference number quantifies the fraction of conducting lithium ions as opposed to other conducting cations or anions in the system. A value of unity signifies that the

electrolyte is highly efficient because all ionic conduction can be attributed to the diffusion of

lithium in the electrolyte. ISE can be crystalline or amorphous, of which each exhibit specific

advantages. A subclass of crystalline ISE known as "superionic conductors" have shown

superior ionic conductivity compared to their amorphous counterparts. For example, $Li_{1+x}Al_xGe_{2-x}(PO_4)_3$ (LAGP) exhibits room temperature conductivities near 10^{-2} S/cm,[4] about two orders of

magnitude higher than competitive amorphous ISE. Superionic conducting ISE are believed to

conduct anisotropically through ordered conduction channels in the lattice, while in most other

crystalline materials, ion transport is believed to occur due to defects or disorder in the material.

Group 1 and 2 halides and select oxides have a compact crystalline structure in which interstitial

ions and vacancies enable ionic migration. **Figure 1-1** shows a model of fast lithium-ion

conductor ISE of composition $La_{0.62}Li_{0.16}TiO_3$.
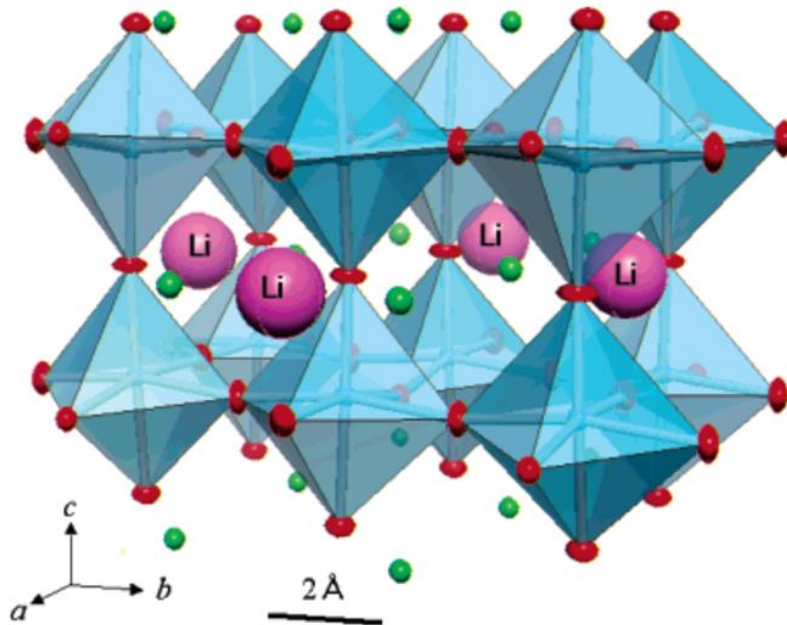
Figure 1-1 Crystal structure $La_{0.62}Li_{0.16}TiO_3$ generated using crystal parameters from neutron-diffraction data. The pink, green, and blue spheres and red ellipsoids denote Li, La, Ti, and oxygen ions, respectively.[9]

Crystalline compounds like beta-alumina contain one ionic species that provides structural

rigidity while a sublattice of energetically equivalent cation sites, separated by small energy

barriers and only partially occupied, allows for frequent jumps between sites.[10] Despite the mechanical rigidity of these crystalline lattices, ISE are brittle and possess high grain boundary resistance, and they establish poor contact with electrode surfaces that is exacerbated by electrode volume changes during cycling.[11]

SPE consist of a polymer phase with salt dissolved in it. The polymer has polar groups to form coordination bonds with the cations and anions of the salt. SPE can be crystalline, semi-crystalline, or amorphous. The general consensus is that ionic conduction occurs overwhelmingly in the amorphous phase where segmental motion of polymer chains aids the transport of weakly coordinated ions as they diffuse from site to site through the polymer matrix and that crystalline regions are an obstacle to this conduction. However, a dissenting view proposes that crystalline phase polymer chains form ordered helical channels for lithium ions to move through.[12] A schematic of these proposed conduction mechanisms is shown in **Figure 1-2**.
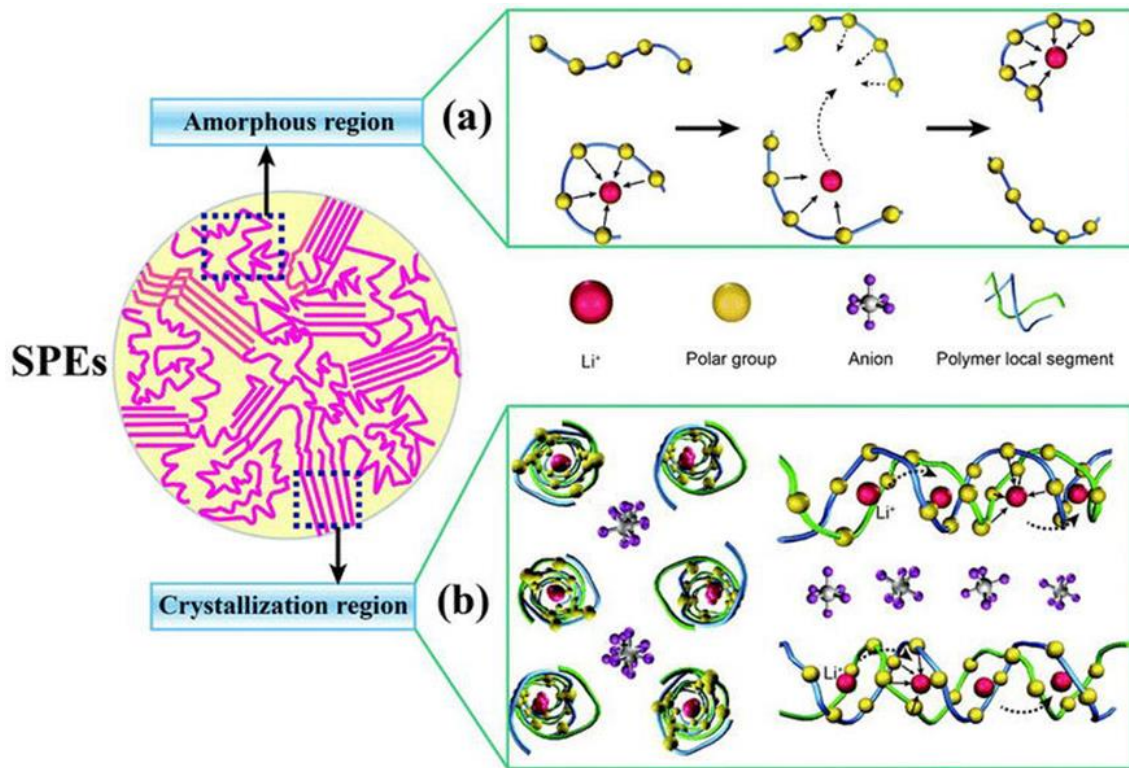
Figure 1-2 Ion transport mechanism in polymer PEO in (a) amorphous and (b) crystalline region.[13]

Polyethylene oxide (PEO) is the most thoroughly studied polymer for SPE applications due to its excellent salt solvation properties. The mechanical compliance and adhesive property of polymers help to form intimate contact with electrodes, but they possess poor mechanical and thermal stability. Lithium transference numbers are well below unity due to other mobile ions. PEO is 80% crystalline and therefore possesses a low room temperature ionic conductivity on the order of 10^{-5} S/cm. As a result, researchers pursue strategies to reduce the formation of crystalline domains, such as adding chemical plasticizers or inorganic nano-particles.[14] CSE contain both inorganic ceramic and organic polymer components, which opens the possibility of synthesizing an electrolyte that exhibits the distinct advantages offered by each of these components, while compensating for inherent disadvantages. CSE are often viewed as a polymer matrix to which inorganic filler particles or fibers are added. Fillers are classified as either passive or active. Passive fillers, such as SiO_2, Al_2O_3, and TiO_2, are not directly involved in the lithium transport process but still enhance the ionic conductivity by disrupting polymer crystallization and improving Li^+ dissociation via Lewis acid-base interactions. Active fillers, such as LAGP, Li_3N, and $LiAl_2O_3$, contain lithium and can therefore provide conduction pathways of their own.[10,11] On the other hand, crossing the interface between the matrix and the filler particles in order to take advantage of these incurs extra resistance, which may all but eliminate the advantage of conductive fillers. **Figure 1-3** depicts possible complex structures in the CSE containing poly(vinylidene fluoride) polymer and the active crystalline filler $Li_{6.75}La_3Zr_{1.75}Ta_{0.25}O_{12}$ (PVDF/LLZTO).
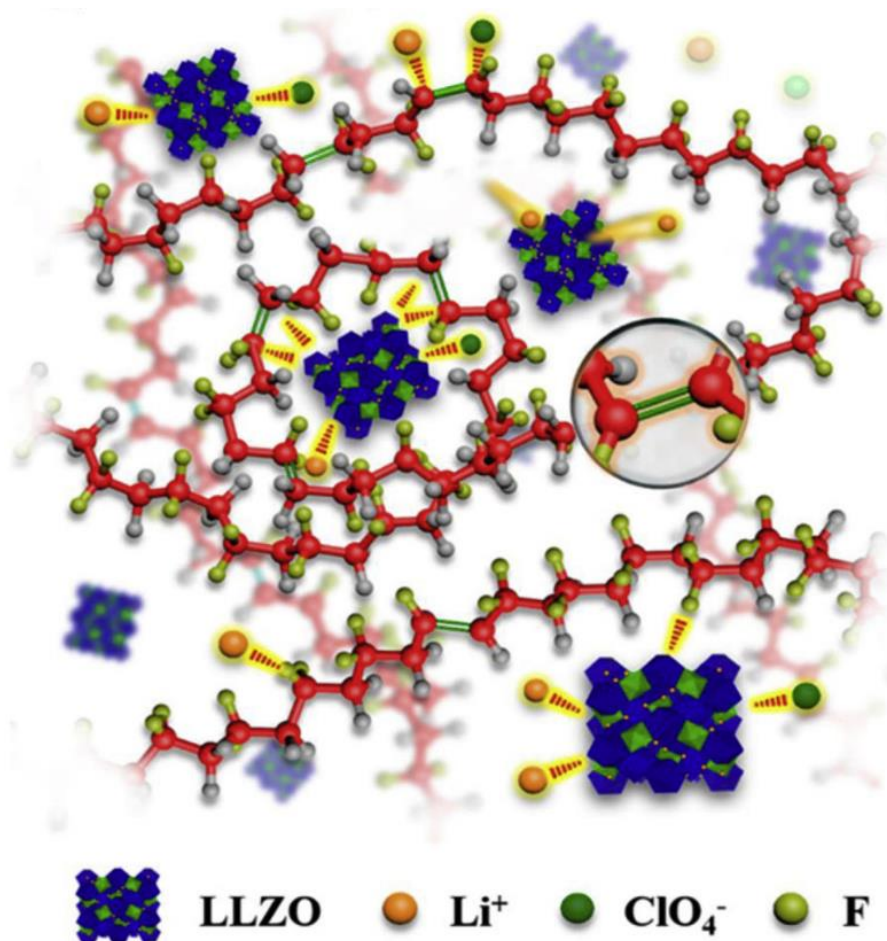
Figure 1-3 Possible complex structures in the PVDF/LLZTO CSE, where blue clusters denote LLZTO.[15]

In a recent study we demonstrated that a highly conductive interfacial layer develops around active filler particles, which extends several tens of nm into the polymer and changes its constitution. When filler particles are nanosized and spatially well dispersed, percolation across this interphase can be achieved with particle loading of only a few vol.%. The exact nature of this interphase is difficult to determine, but it appears to involve a significant degree of distortion of the polymer backbone while the chemical composition is essentially unchanged. A major draw of CSE is that their properties can be adjusted and fine-tuned through varying their chemical composition, without concern for which compositions are thermodynamically or kinetically viable, as with crystalline ISE. They lack grain boundaries that are resistive and sensitive to

corrosion, have promising ionic conductivities, and have good flexibility and electrode interfacial contact when compared to crystalline counterparts.[4]

Though some ISE compositions have been reported to have room temperature conductivities of 10^{-3} S/cm, solid state electrolytes with commercially overall attractive properties are still a work in progress, and improvements have been slow since explorations are largely based on trial and error. Practical solid-state electrolytes should have both high ionic conductivity as well as structural rigidity in order to achieve necessary energy and power densities, but little is known quantitatively about the relationship between structure and ionic mobility to date. The fact that singularly well performing materials have been discovered in each of the above SSE categories suggests that the ionic conductivity of a material cannot be simply gauged from the constituting elements and the type of bonding between them, but that structural subtleties are equally responsible for the creation of low-activation energy passageways. To identify these outstanding electrolytes more reliably requires a better understanding of what constitutes a low-activation energy pathway in a molecular structure.

1.1.2 Non-Arrhenius Temperature Relationship for Transport Processes in Glass Formers

A notable phenomenon of interest identified in the study of solid-state electrolytes is the peculiar temperature-dependence of the structure and resulting atomic transport dynamics. This can be seen in the non-Arrhenius form of the relationship between ionic conductivity and temperature when SSE are studied at elevated temperatures. The typical temperature-dependence of ionic conductivity in solids is of Arrhenius form described well by the following expression,

$$\ln(\sigma T) = \ln(A) - \frac{E_a}{k_B T}, \qquad\qquad (1.1)$$

where σ is the ionic conductivity, T is the temperature, A is often referred to as the frequency factor and is related to the entropy of activation for the elementary process, k_B is the Boltzmann

constant that acts as a proportionality factor between thermal energy and thermodynamic temperature, and E_a is the activation energy required for the process to occur. The relationship between $\ln(\sigma T)$ and $1/T$ is linear. However, the conductivity of glass forming SSE only follow the Arrhenius law at low temperatures while deviating from this linear relationship as the temperature increases, and at high temperatures the conductivity appears to saturate, resulting in non-Arrhenius ionic conductivity as a whole.[16] This type of non-Arrhenius ionic conductivity has been observed in numerous glass forming SSE systems.[17–21] Some example SSE compositions exhibiting this type of behavior are shown in **Figure 1-4**.
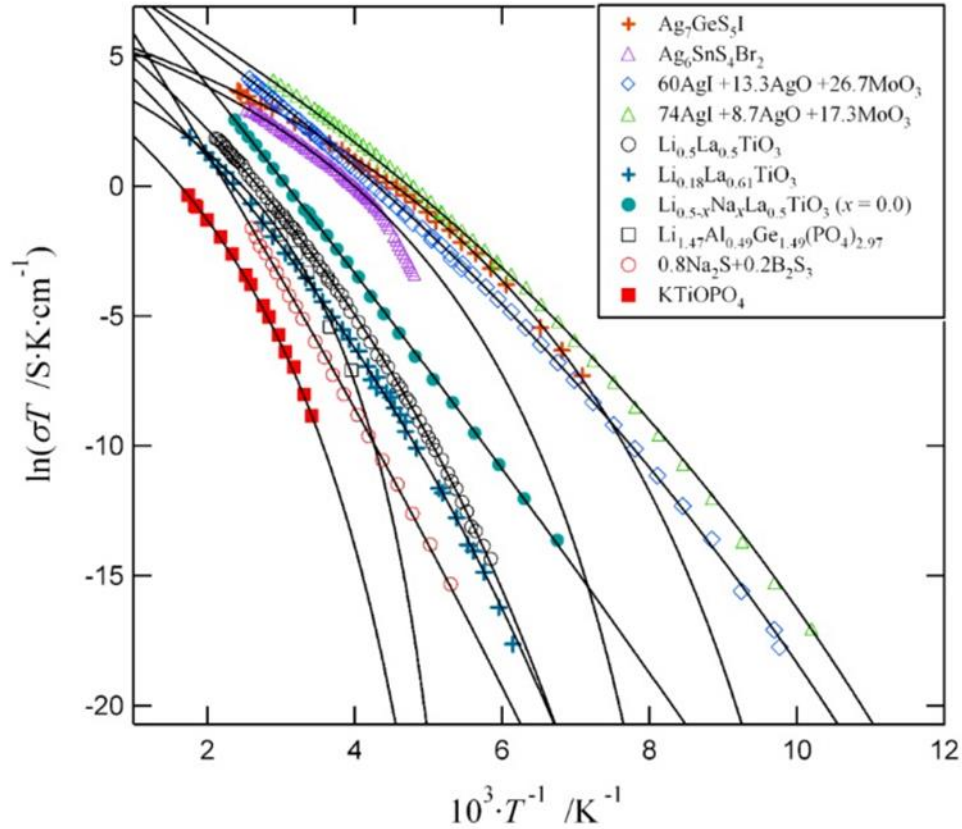
Figure 1-4 The temperature dependencies of the ionic conductivity in a selection of solid electrolytes. The symbols represent experimental data and the solid curves are fits.[16]

This behavior for ionic conductivity and, as a result of the Nernst–Einstein relation, ionic diffusivity is identical to the temperature-dependence observed for another important transport

property of these glass forming systems – viscosity. In the following work, we investigate

viscosity in addition to solid-state diffusion due to its similarities with diffusion and the

availability of extensive experimental data sets.

After considering the atomic dynamics from which these macroscopic properties arise, it should

not be surprising that they possess similar dependencies with respect to temperature. Diffusivity

and viscosity are quantitatively related via the Stoke-Einstein equation,

$$D = \frac{k_B T}{6\pi\eta r},$$
(**1.2**)

where η is the viscosity coefficient and r is the radius of the particle. This equation applies best

to spherical particles in flow characterized by a low Reynolds number, i.e., the viscous forces are

comparable or greater than inertial forces. Qualitatively, both particle diffusion and viscous

dissipation are characterized by particle hopping mechanisms and thus are emergent properties of

many of the same fundamental dynamical processes. This relationship breaks down for

supercooled liquids as the dynamics governing the two processes diverge.[22–25] As will be shown

in the following section, the viscosity-temperature profiles for glass forming liquids look very

much like mirror images of the ionic diffusivity profiles. Even though the viscosity coefficient is

a linear response rate coefficient for the transport of momentum, its magnitude depends inversely

on the atomic mobility. Consider Newton's law of viscous flow where the shear stress,

representing the flux of momentum, is proportional to the velocity gradient in the shear flow.

Considering that achievable shear flow rates are much smaller than the instantaneous velocities

of atoms moving about their potential wells, the relative velocities between two adjacent

molecular layers is but a minute bias in this motion. Inherently high atomic mobility results in a

large bias velocity for a given applied shear stress, and consequently, a low shear viscosity. This

is why the curvature temperature dependence of viscosity is inverted.

1.1.3 Viscosity and Viscous Relaxation of Glass-Forming Liquids

Accurate knowledge of the viscosity of glass forming liquids and its variation with temperature, pressure, and chemical environment is a fundamental aspect of numerous fields of study and technologies, which include macromolecular and polymeric sciences[26,27], ionic and complex liquids[28,29], geophysics[30,31], food and drug sciences[32–34], ceramics[35,36], and metallurgy[37,38]. The ability to navigate the regime of state variables in which the molecular system must be conditioned to prevent it from accessing its thermodynamically stable crystalline state is key to achieving the unique properties associated with materials that are amorphous and monolithic at all length scales. Reliable prediction of the viscosity is essential for regulating working temperatures, establishing proper annealing conditions, suppressing crystal growth, and carrying out physical processing, molding, and shaping of glass and glass-ceramics products.[39–41] Furthermore, the rapid increase in viscosity with decreasing temperature is perceived to reflect an essential characteristic of the glass transition phenomenon and has therefore spurred a distinct field of scientific study.[27,32,37,42–45] In particular, there are aspirations that a better understanding of what causes such an accentuated change in the structural relaxation rates of glass forming systems may provide insights into the nature of the amorphous state of matter, a mystery that has thus far remained impervious to conventional structural probes. To this end, it is necessary to connect viscosity with the underlying molecular scale processes. In the early 1930s, Eyring derived his model for the viscosity coefficient, which provides a formalism that can be used to quantify the elementary mechanisms of this complex process on the basis of transition state theory.[46] Calculation of viscosity requires the evaluation of the relaxation rate where the system must overcome and activation barrier from one equilibrium state to another. The relaxation rate is shown to principally depend on the factors described in the following equation,

10

$$\Gamma \propto \left(\frac{Q_a}{Q_g}\right) e^{\frac{-E_a}{k_B \cdot T}}, \tag{1.3}$$

where Q_g is the ground-state partition function, Q_a is the activated-state partition function, E_a is the activation energy required for the process to occur, and T is the temperature.[46] The difference between the natural logarithms of the activated and ground state partition functions is equal to S_a, or the entropy of activation. This is the difference in entropy, or difference in the number of equivalent energy microstates, between the activated and grounds states. The amount of energy dissipated in viscous flow is inversely proportional to the relaxation rate, so Eyring's equation for viscosity is written as,

$$\eta = h \frac{\lambda_z}{\lambda_x \lambda_y \lambda^2} e^{\frac{-S_a}{k_B}} e^{\frac{E_a}{k_B \cdot T}} = h\rho_N e^{\frac{-S_a}{k_B}} e^{\frac{E_a}{k_B \cdot T}}, \tag{1.4}$$

where h is Planck's constant and $\rho_N = \lambda_z/(\lambda_x \lambda_y \lambda^2)$. The various l-parameters represent the characteristic length scales on which the elementary relaxation mechanism takes place. Specifically, Eyring conceived of two layers of a liquid being sheared passed one another in opposite directions as a result of an applied shear stress $\pm\tau_{zx}$. Rather than sliding past one another steadily and simultaneously as a collective, the molecular entities jump individually from one equilibrium position to the next in a stochastic fashion. In due course all molecules jump eventually with an average bias in the direction of the applied shear stress. In this description, λ_z is the distance between the liquid layers, λ_x and λ_y make up the per atom contact area of the layers, and λ is the atomic jump distance of the mechanism. The length parameters λ, λ_x, λ_y, and λ_z are all on the order of the interatomic spacing and together can be combined to represent the reciprocal volume, ρ_N, involved in the jump mechanism. **Equations 1.3** and **1.4** assume that the energy and entropy of activation are constant. That is that these values, and therefore the potential energy surface of the structure they arise from, do not change as a function of

temperature. This formalism adequately describes the temperature dependence of the viscosity coefficient for simple liquids, resulting in a linear relationship between the logarithm of the viscosity and inverse temperature, $1/T$. However, this equation is unable to capture the complex viscous characteristics of most glass-forming liquids.

For most glass forming liquids, the temperature dependence of viscosity deviates from the semilogarithmic linearity of Eyring's equation in ways reflected by a steeper slope at low temperatures and a shallower slope at high temperatures. The underlying reason for the deviation from Arrhenius behavior in the temperature dependence of the viscosity has been a factor of intense scrutiny.[43,45,47,48] Austen Angell plotted viscosity data for various types of glass forming liquids vs. reciprocal temperature normalized with respect to the glass transition temperature, T_g, thereby devising the so-called Angell plot shown in **Figure 1-5**, which casts the viscosity profiles onto a set of master curves. Based on this observation, he conceived the concept of strong vs. fragile behavior to categorize the temperature dependence of the viscosity for glass forming systems.[49–53] This paradigm has enabled researchers to better gauge, label, and interpret their findings. The more the $\log_{10}(\eta)$ vs. T_g/T data deviates from linearity, the more "fragile" the liquid is said to be, while nearly linear, or Arrhenius, behavior is designated as "strong".[54] To quantify this phenomenon, various fragility indices have been suggested to date. The most commonly utilized of these is the kinetic fragility, m, which is based on the slope of the log viscosity versus inverse temperature relationship at the glass transition temperature.[55]

$$m = \lim_{T \to T_g} \frac{\partial \log_{10} \eta}{\partial \left(T_g / T \right)} \tag{1.5}$$
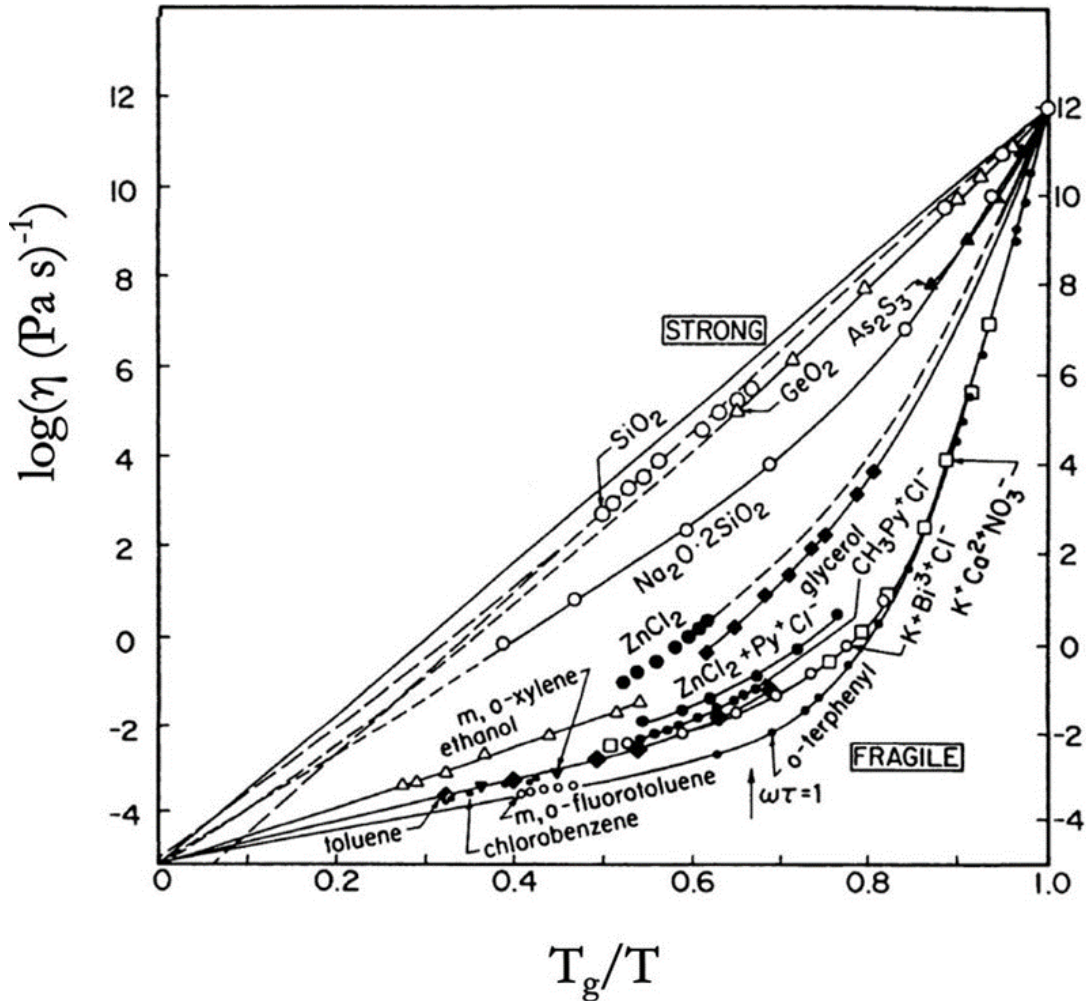
Figure 1-5 Angell Plot depicting the pattern of liquid viscosity-temperature relations for T_g-based normalization showing contrast between network and molecular or simple ionic liquid behavior.[49]

Despite the progress made towards the development of theoretical frameworks, categorization, and quantitative tools, the structural and physicochemical origin of this non-Arrhenius behavior remains an open question. Early investigations revealed correlations between fragility and the size of the heat capacity jump at the glass transition. While this remains a strong connection between kinetic and thermodynamic fragility,[20] the continued accruing of data suggests that this may not be comprehensive indicator across different types of materials.[21] Conversely, the rate of change of the excess configurational and vibrational entropy, as the liquid approaches its glass transition, appears to yield a more universal measure and stronger connection between kinetics

and thermodynamics.[21–25] Finally, the role of configurational entropy in characterizing fragility

has also been identified among the quantities used in the topological constraint theory describing

network glasses, e.g., the mean field connectivity within a coarse-grained representation of the

intermediate-range order in these structures.[26, 27] The most widely used models to date are very

successful at interpolating the viscosity-temperature relationship and have some success in

extrapolation but yield little insight into the microscopic structural and mechanistic processes

affecting viscosity in these glass-forming liquids when relaxation takes on non-Arrhenius

character.

1.2 Computational Methods and Frameworks

1.2.1 Classical Molecular Dynamics Simulations

Classical molecular dynamics (MD) is a computational method that enables the simulation of

materials at atomic-scale resolution. This refers not only to the spatial resolution but the

femtosecond temporal resolution as well. This method is complementary to experimental

characterization methods in pursuit of investigating materials properties and characteristics.

Molecular dynamics simulations are often utilized for one of two purposes: (1) property-driven

materials prediction and design or (2) materials structural and/or dynamics investigation. The

first use case utilizes the often more rapid and lower cost of computer simulation when compared

to experimental materials synthesis and characterization to search for material compositions

and/or structural motifs that possess properties of interest for an engineering design solution. In

this case, MD simulations precede experimental validation in the research and development

process. The second use case involves computer simulations as a characterization tool, often in

addition to experimental characterization methods, for known materials that have already been

synthesized. In this case, the MD simulations act as a "computational microscope" enabling the

user to peer into nanostructure of the material and probe the atomic-scale features and mechanisms from which the macroscopic properties of interest arise. This gives the ability to investigate materials on length and timescales that are beyond the resolution of experimental techniques.

The methods used in the following work are categorized as classical MD simulations, as opposed to *ab initio* MD (AIMD). Classical MD generally utilizes empirical interatomic potential energy functions to govern atomic interactions while AIMD methods use density functional theory or other quantum chemistry methods to calculate atomic interactions. The calculations for AIMD explicitly calculate electron interactions and, while often more accurate, are much more computationally expensive than the calculations for classical MD. This dramatically limits both the spatial extent and the time of the simulation that can be reasonably attained. AIMD simulations are usually limited to hundreds or thousands of atoms and picosecond timescales while classical MD can typically simulate thousands to millions of atoms and nanosecond to microsecond timescales depending on the complexity of the empirical potential used. **Figure 1-6** shows a comparison between the length and timescales of typical computational methods used in materials science and engineering.
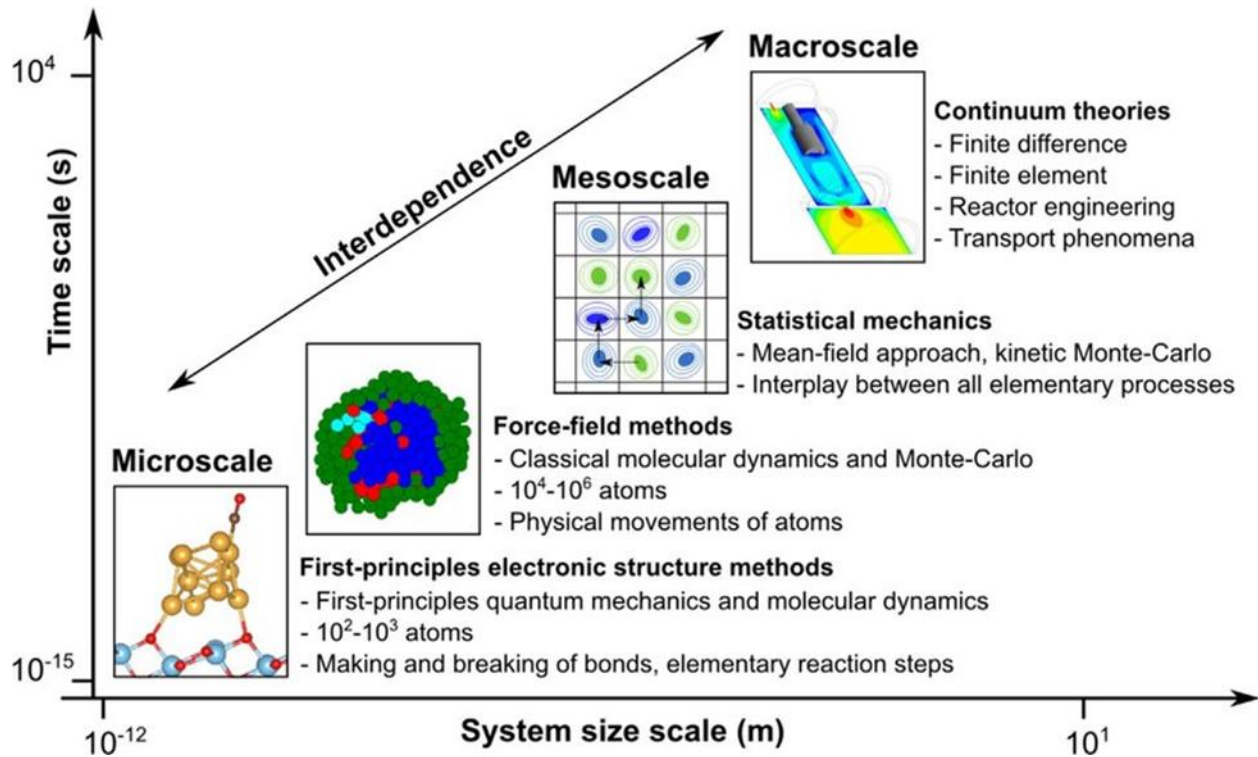
Figure 1-6 Comparison of length and time scales for computational methods utilized in materials science.[56]

Due to the many-body nature of essentially all systems of interest for materials engineering, describing the resultant dynamics of the component particles for their mutual interactions cannot be done analytically. However, leveraging the computational power of computer processors, solutions can be approximately to a high degree of accuracy using numerical methods to integrate Newton's equations of motion with respect to time based on empirical interatomic potential functions that govern the interactions of atoms within the system. A general, simplified scheme for the MD algorithm describing the steps for calculating a new velocity and position for an atom *i* based on potential energy for a given discrete time step is shown in **Figure 1-7**.

Energy calculation (force-field)

$$E_{pot}\{x_i\}$$

Forces

$$F_i = -\partial E_{pot}/\partial x_i$$

$$a_i = F_i/m_i$$

Trajectory

Numerical integration

$$v_i(t+dt) = v(t)_i + a_i\,dt$$

$$x_i(t+dt) = x(t)_i + v_i\,dt$$
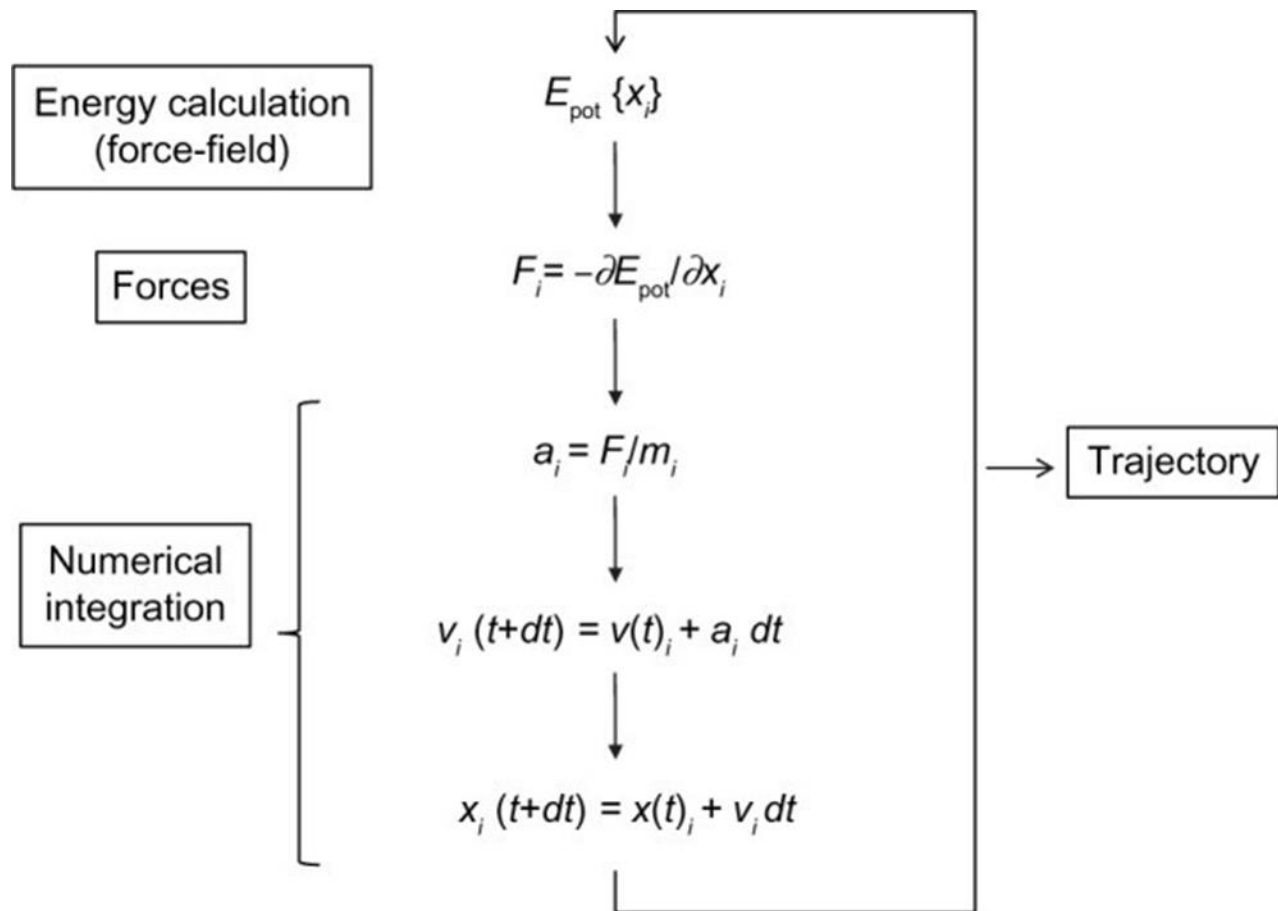
Figure 1-7 Basic MD algorithm for updating atomic velocities and positions from time t to time $t + dt$.[57]

In the scheme, E_{pot} is the interatomic-potential energy function that describes the energy of atom i based on its position X_i. The forces, F_i, on atom i are calculated from the spatial derivative of the potential energy E_{pot}. Knowing the mass of atom i and having calculated the forces on the atom, Newton's second law can be used to calculate the acceleration, a_i. Then a numerical integration method is used to integrate the velocity-time equation of motion with respect to time to yield an updated atomic position from that at time t to that at time $t + dt$. This process is used for all atoms in the system and repeated for as many discrete time steps, dt, as desired.

The interatomic potential is the vital component of MD simulations, which encodes the interactions between particles within the simulated material, enabling the emulation of specific

17

atomic species and their chemical bonding behavior to reproduce structural features and

mechanical and transport properties.
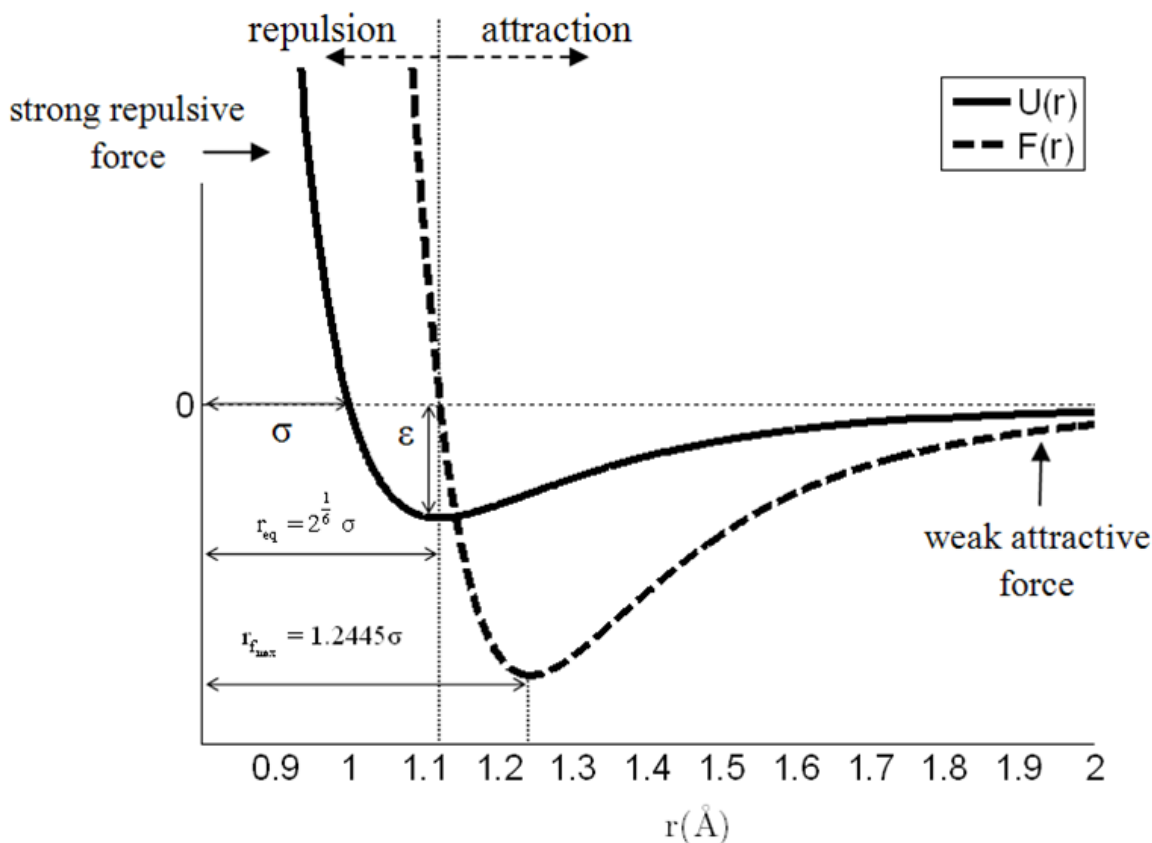
Figure 1-8 Example of Lennard-Jones interatomic pair-potential.[58] The solid line represents the energy of the bonding interaction as a function of distance. The variable σ dictates the zero-energy location while ε sets the magnitude of the energy at equilibrium. The dashed line represents the force on the atom as a function of distance due to the interaction. A positive force represents atomic repulsion while a negative force is indicative of attraction.

The interatomic potential function is generally composed of a pairwise bonding term describing

energy, and therefore forces, as a function of interparticle distance but may also include a three-

body term for angular constraints, four-body term for torsional constraints, and/or other many-

body terms. **Figure 1-8** shows how the potential energy and force varies with distance for a

Lennard-Jones pair potential, one of the oldest and simplest interatomic potentials used in

molecular simulation to represent van der Waals interactions. Both the energy and force are

weak for long distances but increase in magnitude as the distance decreases. The minimum in the

energy curve represents the most stable location as this is also the location where forces are neither attractive nor repulsive. At distances closer than the minimum energy location, the forces become positive, indicating a repulsive force. This repulsive force represents nuclear core repulsion and becomes very strong with small decreases in interatomic distance as atomic nuclei impinge on one another.

Interatomic potentials may also contain terms pertaining to non-bonded interactions such as electrostatic or van der Waals interactions. While the bonded interactions only occur locally and therefore only involve a few atoms at a time, non-bonded interactions are non-local. This means that while the energetic contribution to the energy may diminish with increasing interatomic distances, it never decreases to zero. Also, while the energy decreases with increasing distance, the number of particles with which to interact increases as the surface area of a spherical shell at that distance, $4\pi r^2$, where r is the distance from the particle. In fact, unless the potential energy contribution decays faster than r^{-3} the energy diverges in the infinite limit, removing simple truncation and tail-correction as an option.[59] This problem is avoided by utilizing the Ewald summation, or equivalent subsequently developed methods. The Ewald sum applies a fictitious charge screening, typically gaussian in form, to particles with is set cutoff distance. This artificially removes charged interactions beyond the cutoff allowing for a rapidly converging sum of charged interactions. Then the previously screened charge contributions beyond the cutoff distance are summed as a rapidly converging Fourier series in reciprocal space and the spurious self-interaction energy from this method is later corrected.[60]

Even with the increasing capability in recent years to simulate more and more atoms simultaneously, the largest simulations of $\sim 10^6$ atoms are still dwarfed by the size of real engineering materials of $\sim 10^{23}$ atoms. This means that the ratio of surface atoms to total atoms

in simulations would be approximately 5 orders of magnitude greater than for common human-scale materials. Atoms at the surface of a material are of higher energy and less stable than those within the bulk due to dangling and distorted bonds. This can have a significant effect on the structure and dynamics of small systems. While there are some reasons to simulate surfaces, most MD simulations utilize periodic boundary conditions such that atoms at one face of the simulation box are bound to atoms at the opposing face of the simulation box. In this way, a system with no surfaces is created that better approximates the bulk properties of real materials, so long as the simulation size is large enough, typically a few thousand atoms, that the periodic boundary conditions do not result in atoms interacting with themselves through the periodic boundary.

So now that we've briefly discussed how to run an MD simulation, how does one extract meaningful measurements and results from a simulated material? Microscopic quantities such as particle potential energies, forces, accelerations, velocities, and positions values that come directly from the simulation as a part of the time integration loop procedure do not correspond to any experimentally measured macroscopic properties. To enable comparison between MD simulations and experimental measurements, one must bridge the large disparity in both time and length scales. This can be accomplished using the formalism of statistical mechanics by which macroscopic thermodynamic, mechanical, and transport properties can be calculated using quantities pertaining to individual atoms that are ensemble and/or time averaged. Here, we forego any extensive discussion of statistical mechanical methods and formulae and instead briefly introduce a few select formulae that are important for later analyses in the present work, which focuses on transport properties, specifically diffusion for the sections involving MD simulation. Evaluation of diffusion coefficients is perhaps the most common approach to

characterizing atomic mobility in MD simulations. This can be accomplished based on calculating the mean squared displacement (MSD) or the velocity auto-correlation function (VACF) associated with atomic trajectories.

1.2.2 Particle Mean Squared Displacement

The ensemble-averaged MSD of particles collected over the course of a simulation yields the diffusivity based on the following relationship,

$$D = \lim_{t \to \infty} \frac{\langle |\vec{r}(t) - \vec{r}(0)|^2 \rangle}{2d \cdot t}, \tag{1.6}$$

where $r(0)$ is the particle position at the time origin, $r(t)$ is the particle position at a subsequent time t, and d is the dimensionality of the system. For adequately sampled atomic trajectories, the MSD typically exhibits a ballistic regime at short times and a diffusive regime at times when correlation between atomic jumps is effaced by randomization of trajectories. Accordingly, the diffusivity is obtained from the slope of the MSD vs. time in the diffusive regime, characterized by compelling linearity in the relationship between MSD and time. This method breaks down for temperatures near and below the glass transition temperature as the relationship is no longer linear and the movement of ions between adjacent sites becomes a rare event. **Figure 1-9** shows the MSD for sodium in simulated sodium borosilicate as a function of time for various temperatures that exemplify this behavior.
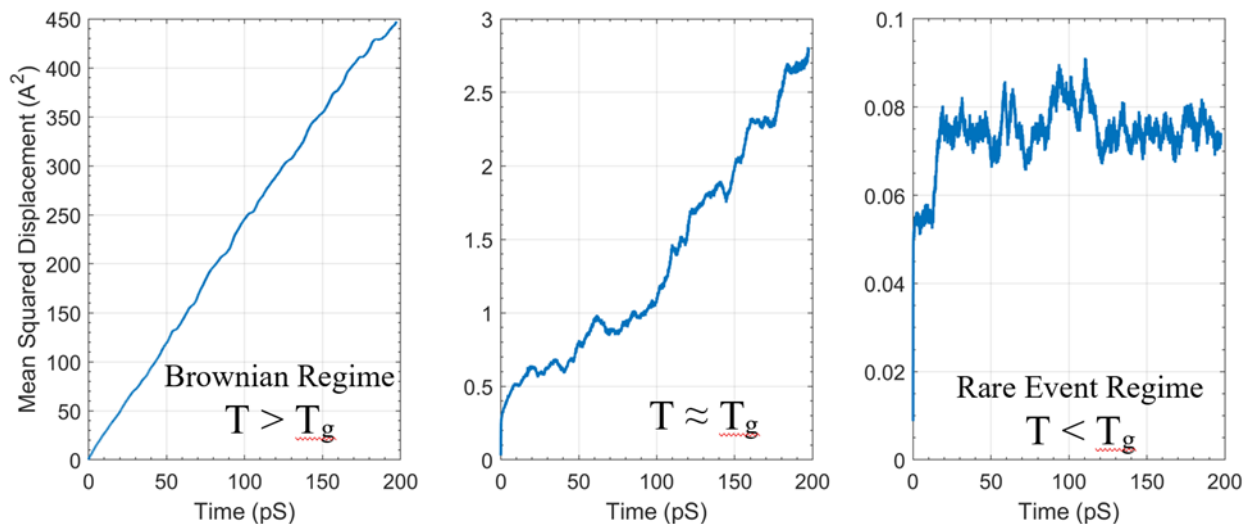
Figure 1-9 MSD as a function of time for sodium ions in simulated sodium borosilicate representing different diffusive regimes.

To calculate the MSD in MD simulations with periodic boundary conditions, particle position data for the "unwrapped" particle coordinates must be incrementally stored for the duration of the production run. Unwrapped particle coordinates refer to those for which the simulation box length is not subtracted when the particles pass through a periodic boundary and reenter the opposite side of the simulation box.

1.2.3 Particle Velocity Auto-Correlation Function

Provided knowledge of the velocity of each particle as a function of time, the MSD can be expressed by integrating these velocities over time. Further manipulation of the resulting expression yields the VACF formalism, which given adequate statistics, yields the same result as the analysis of MSD. Interestingly, though, MSD and VACF produce this information by examining different time regimes.[61] Specifically, with the VACF analysis of a dynamical processes we quantify the decay in correlation of a particle's velocity with itself over time, i.e., the loss of predictability in the particles' motion. In other words, we tally the buildup towards randomness in particle trajectories during the ballistic regime until trajectories transition from

periodic to diffusive. Accordingly, adding up incremental losses from the harmonic oscillatory

character of motion is sufficient to account for a species' capacity for random drift. Hence, MSD

and VACF are complementary in the way they assess atomic mobility, and discrepancies

between the obtained with each construct may be indicative of systemic non-idealities.

Numerically, computing the VACF involves taking the ensemble average across multiple time

origins of the inner products of each particle's velocity vector at the time origin with its velocity

vector at each subsequent timestep. The decorrelation in this value results from the transfer of

momentum between the reference particle and its surrounding particles. The time integration of

the VACF yields the diffusion coefficients as

$$D = \frac{1}{d} \int_0^\infty \langle \vec{v}(0) \cdot \vec{v}(t) \rangle dt, \tag{1.7}$$

where $v(0)$ is the velocity vector of a particle at the time origin, $v(t)$ is the velocity vector of the

same particle at a subsequent time t, and d is, again, the dimensionality of the system. A simple

example VACF and graphical depiction of the integration to calculate the diffusivity is shown in

Figure 1-10. **Equation 1.7** is one of the Green-Kubo relations that connect the integration of

time correlation functions to transport coefficients. Since the VACF can neither be collected nor

integrated to infinite time, the method relies on the oscillatory character of the VACF to

substantially subside within accessible times, typically a few picoseconds. This also allows for

more averaging since, with the same amount of velocity data, a greater number of time origins

can be used for shorter VACFs.
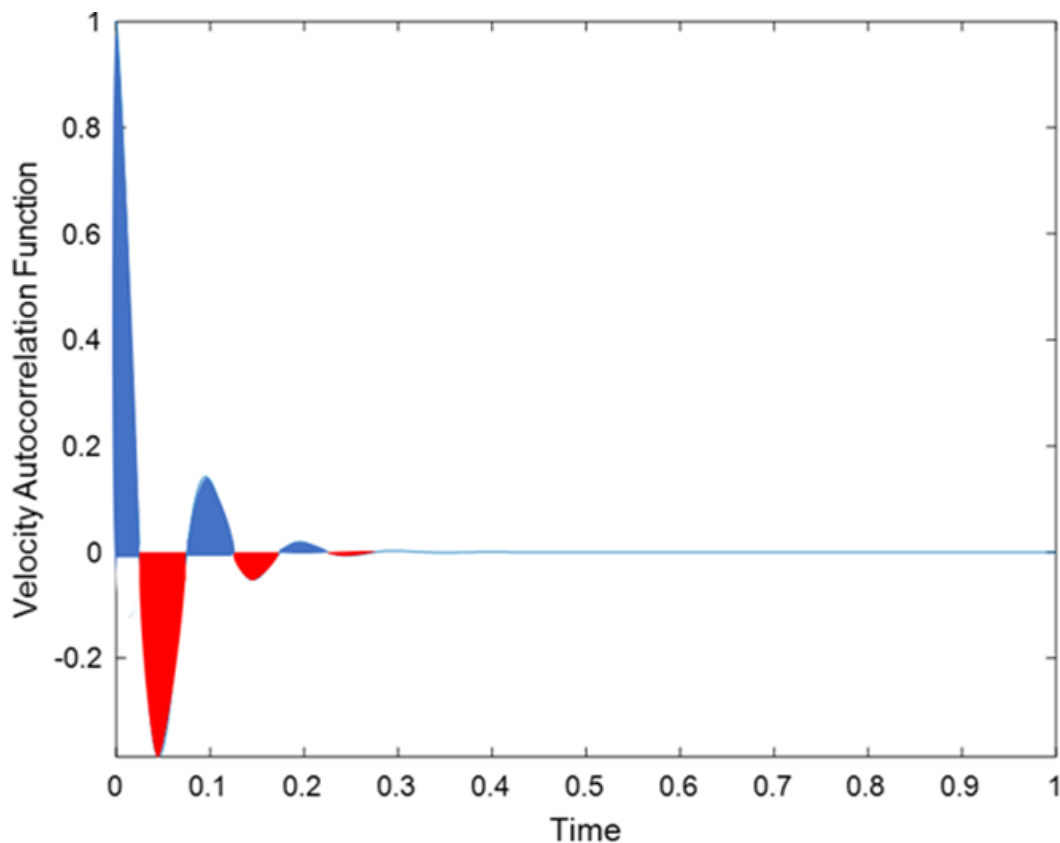
Figure 1-10 Scheme depicting the integration of a velocity auto-correlation function. Blue sections are positive contributions to the integral and red are negative.

1.2.4 The Vibrational Density of States

In the zero-temperature limit, the Fourier Transform of the VACF yields the vibrational density

of states (VDOS) for the system equivalent to that obtained using normal mode analysis

$$\varphi(\omega) = \int_0^\infty \langle \vec{v}(0) \cdot \vec{v}(t) \rangle e^{-i\omega t} dt, \tag{1.8}$$

where i is the imaginary unit and ω is the angular frequency. However, at finite temperature,

where diffusion can occur, this relationship is not strictly true. The Fourier Transform of the

VACF in this case still results in a vibrational spectrum, but it is only an approximation of the

vibrational density of states as translational motion of particles is present and the anharmonicity

of the interatomic potentials governing particle interactions is not negligible, i.e., the harmonic

approximation is not valid.[62] The zero-frequency value of the spectrum divided by the

dimensionality also yields the diffusion coefficient as it results in an expression identical to

Equation 1.7. This finite intercept at zero frequency is a consequence of damping or decay in

velocity correlation function. If not for this damping, the frequency spectrum would be

composed solely of delta functions. An example vibrational spectrum calculated from the Fourier

transform of the VACF in **Figure 1-10** is shown in **Figure 1-11**.
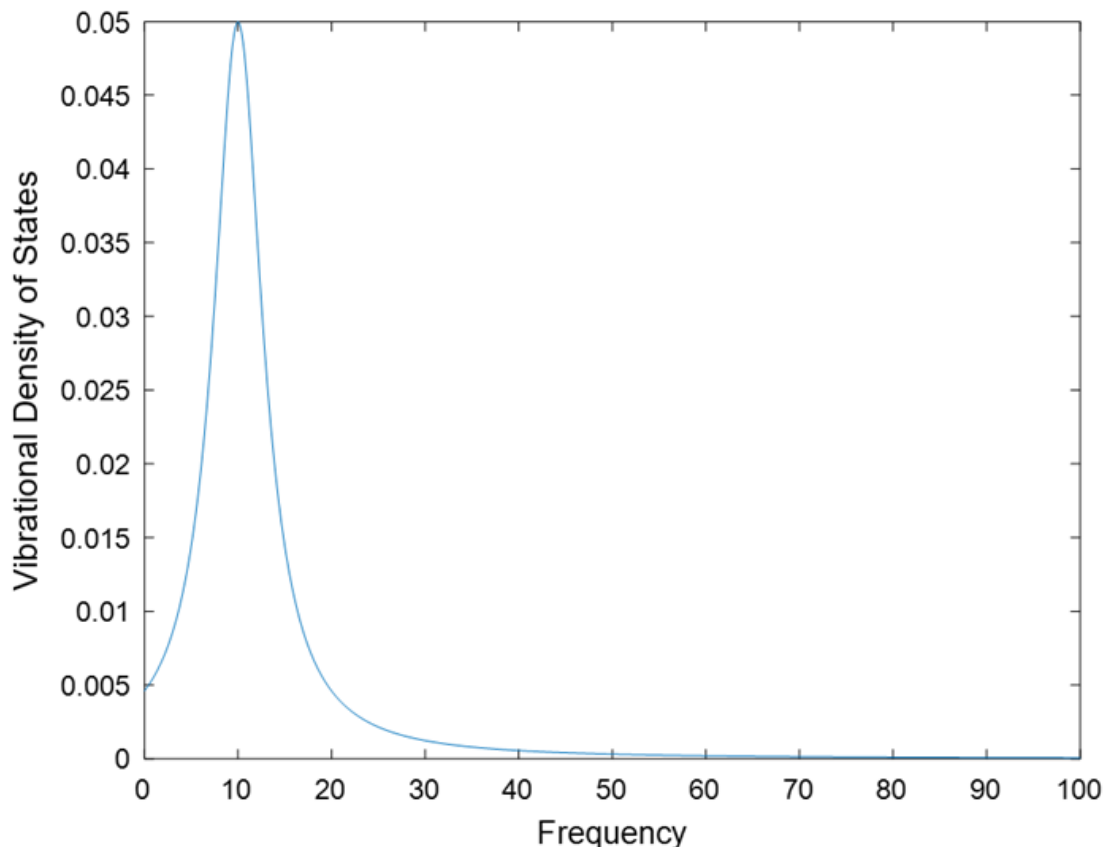
Figure 1-11 The vibrational spectrum of the VACF in **Figure 5** obtained via Fourier transform.

1.2.5 Prony Analysis

An interesting prospective method for extracting dynamical information relevant to particle

diffusion is through partitioning and analysis of the vibrational spectrum into component modes

of motion. This can be done by leveraging Prony's Method, which is a signal processing method

developed by Gaspard de Prony in France in 1795 around the same time that Joseph Fourier

presented the Fourier Series.[63] This method decomposes functions into a series of damped

complex exponentials shown as follows,

$$\sum_{k=1}^{N} \frac{1}{2} A_k e^{(-\Gamma_k \pm i\omega_{0,k})t \pm i\varphi_k}.$$ (**1.9**)

This allows for the estimation of frequency $\omega_{0,k}$, amplitude A_k, damping coefficient Γ_k, and

phase shift φ_k for each component k in the series where i is the imaginary unit. Using this

method, one can extract component modes from the VACF and VDOS. When applying the

Prony analysis to the VACF, however, the damped complex exponential terms can be simplified

by removing the phase shift and replacing the damped complex exponential with a damped

cosine function using Euler's formula. This is due to the physical nature and meaning of the

VACF. For all component modes of motion that the VACF may be decomposed into, the

temporal self-correlation that occurs at the time origin for a particle should always be the

maximum value of the function with respect time as the velocity is perfectly correlated. This

means that a shift in phase would be unphysical, and the oscillatory portion of the function can

always be represented by a simple cosine function like so,

$$\sum_{k=1}^{N} A_k e^{-\Gamma_k t} \cos(\omega_{0,k} t).$$ (**1.10**)

The Fourier transform of **Equation 1.10** yields the component spectral function, often referred to

as a Lorentzian, which can be applied to the VDOS. The form of this function is as follows:

$$\sum_{k=1}^{N} \frac{A_k}{\pi} \frac{\frac{1}{2}\Gamma_k}{\left(\omega - \omega_{0,k}\right)^2 + \left(\frac{1}{2}\Gamma_k\right)^2}.$$ (**1.11**)

An example application of this method is shown in **Figure 1-12** with MD data from a simple

simulation of a Lennard-Jones system.
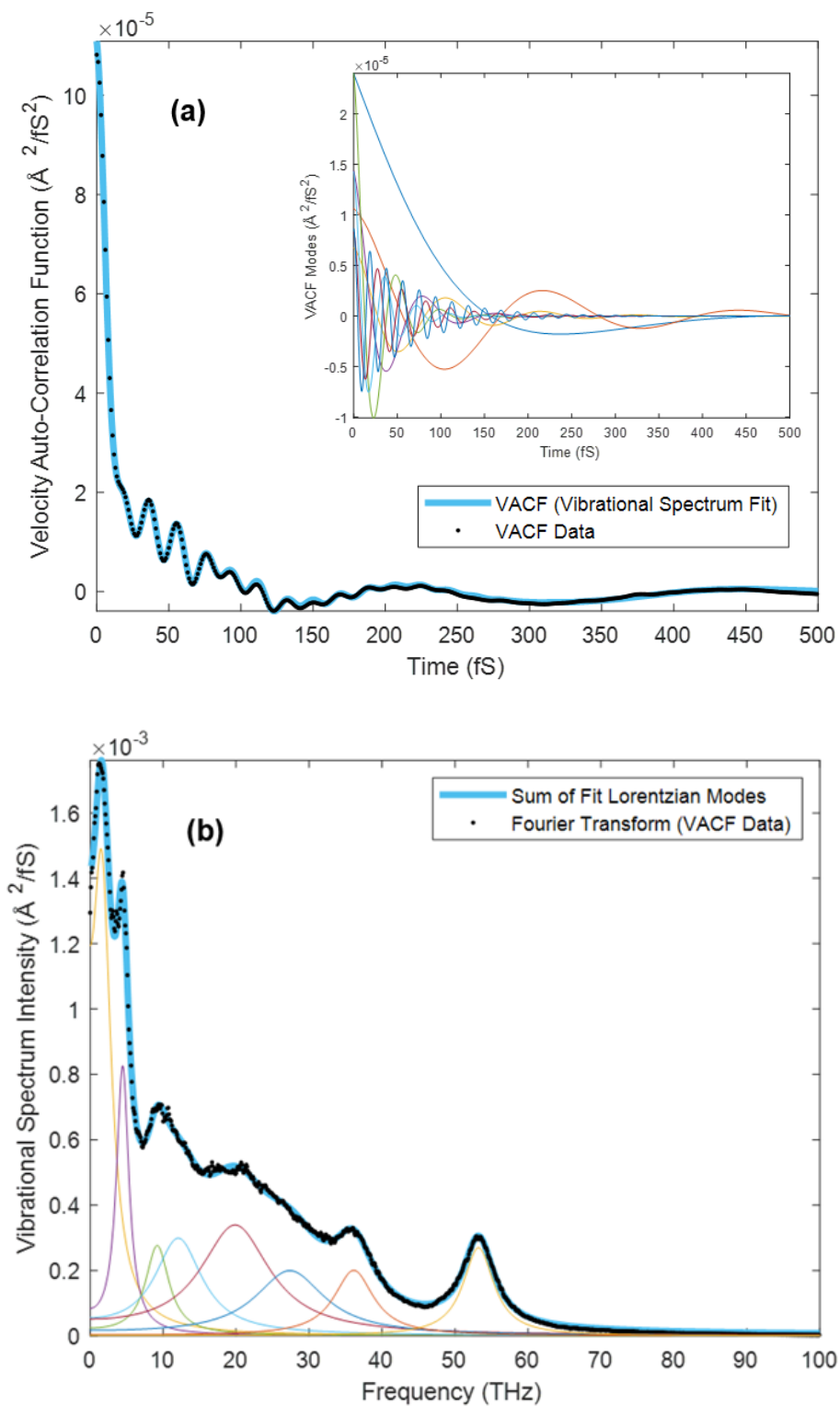
Figure 1-12 Application of Prony analysis to VACF and VDOS of a simple Lennard-Jones system. The VDOS was fit with a series of 8 Lorentzian functions (**b**) and these functions were Fourier transformed as summed to rebuild the original VACF (**a**).

The Fourier transform of the VACF is calculated to produce a vibrational spectrum. Upon deconstruction, the vibrational spectrum is partitioned into 8 component modes seen as a spectrum of Lorentzian functions. These Lorentzian functions are then inverse Fourier transformed to produce 8 damped harmonic oscillators that can be summed to reproduce the original velocity auto-correlation function demonstrating the equivalence of these functional forms and their fits in the time and frequency domains. The extraction of these component vibrational modes may be able to provide insight into the relative contribution of each mode of motion to the diffusivity of the particles and can act as a compass in directing our inspection towards the important dynamics affecting diffusion in glasses, such as the number of relevant modes, their relationship to structural vibrations, and the influence of topology and bonding character. Unfortunately, to date applications of this method to VACF and VDOS data for the purpose of elucidating dynamics of ionic transport have not been fruitful. Lorentzian fits of the VDOS do not yield unique results as fits can always be improved by increasing the number of terms in the series. While the use of 8 to 15 terms usually provides good fits throughout the bulk of the frequency range encompassed by a given vibrational spectrum, the worst-fit region is always the zero-frequency intercept value. The intercept value from all attempted fits thus far overestimates the magnitude when compared to the zero-frequency value from the Fourier transform of the VACF. Increasing the number of Lorentzian terms in the series improves the convergence at zero-frequency but never satisfactorily before the number of terms and corresponding fitting parameters cause the fitting methods to become unstable. While there may still be some value in Prony analyses of VACFs and VDOSs for the investigation of materials properties, without improvements in the fits at zero-frequency implementation of this method for analyzing ion diffusion is unreliable since the zero-frequency value of the VDOS is the location

directly corresponding to the particle diffusion coefficient. For this reason, Prony analyses are

not included in the following chapters.

1.3 References

1. Knauth, P. & Tuller, H. L. Solid-State Ionics: Roots, Status, and Future Prospects. *J. Am. Ceram. Soc.* (2010) doi:10.1111/j.1151-2916.2002.tb00334.x.

2. Hwang, J. Y., Myung, S. T. & Sun, Y. K. Sodium-ion batteries: Present and future. *Chemical Society Reviews* (2017) doi:10.1039/c6cs00776g.

3. Yang, Z. *et al.* Electrochemical energy storage for green grid. *Chem. Rev.* **111**, 3577–3613 (2011).

4. Chen, R., Qu, W., Guo, X., Li, L. & Wu, F. The pursuit of solid-state electrolytes for lithium batteries: From comprehensive insight to emerging horizons. *Materials Horizons* (2016) doi:10.1039/C6MH00218H.

5. Janek, J. & Zeier, W. G. A solid future for battery development. *Nat. Energy* **1**, 1–4 (2016).

6. Liu, K., Liu, Y., Lin, D., Pei, A. & Cui, Y. Materials for lithium-ion battery safety. *Sci. Adv.* **4**, eaas9820 (2018).

7. Kumar, G., Kartha, T. R. & Mallik, B. S. Novelty of Lithium Salt Solution in Sulfone and Dimethyl Carbonate-Based Electrolytes for Lithium-Ion Batteries: A Classical Molecular Dynamics Simulation Study of Optimal Ion Diffusion. *J. Phys. Chem. C* (2018) doi:10.1021/acs.jpcc.8b06581.

8. Cheng, X. B., Zhang, R., Zhao, C. Z. & Zhang, Q. Toward Safe Lithium Metal Anode in Rechargeable Batteries: A Review. *Chemical Reviews* (2017) doi:10.1021/acs.chemrev.7b00115.

9. Yashima, M., Itoh, M., Inaguma, Y. & Morii, Y. Crystal structure and diffusion path in the fast lithium-ion conductor La0.62Li0.16TiO3. *J. Am. Chem. Soc.* **127**, (2005).

10. Souquet, J. L. Ionic Transport in Amorphous Solid Electrolytes. *Annu. Rev. Mater. Sci.* (1981) doi:10.1146/annurev.ms.11.080181.001235.

11. Dirican, M., Yan, C., Zhu, P. & Zhang, X. Composite solid electrolytes for all-solid-state lithium batteries. *Materials Science and Engineering R: Reports* (2019) doi:10.1016/j.mser.2018.10.004.

12. Gadjourova, Z., Martín y Marero, D., Andersen, K. H., Andreev, Y. G. & Bruce, P. G. Structures of the polymer electrolyte complexes PEO6:LiXF6 (X = P, Sb), determined from neutron powder diffraction data. *Chem. Mater.* **13**, 1282–1285 (2001).

13. Gupta, H. & K. Singh, R. Ionic Liquid-Based Gel Polymer Electrolytes for Application in Rechargeable Lithium Batteries. in *Energy Storage Battery Systems - Fundamentals and Applications* (2021). doi:10.5772/intechopen.93397.

14. Wang, W., Yi, E., Fici, A. J., Laine, R. M. & Kieffer, J. Lithium Ion Conducting Poly(ethylene oxide)-Based Solid Electrolytes Containing Active or Passive Ceramic Nanoparticles. *J. Phys. Chem. C* **121**, 2563–2573 (2017).

15. Zhang, X. *et al.* Synergistic coupling between Li6.75La3Zr175Ta0.25O12 and poly(vinylidene fluoride) induces high ionic conductivity, mechanical strength, and thermal stability of solid composite electrolytes. *J. Am. Chem. Soc.* **139**, (2017).

16. Aniya, M. & Ikeda, M. A model for non-arrhenius ionic conductivity. *Nanomaterials* **9**, (2019).

17. Jadhav, H. S. *et al.* Influence of B2O3 addition on the ionic conductivity of Li1.5Al0.5Ge1.5(PO4)3 glass ceramics. *J. Power Sources* **241**, (2013).

18. Ribes, M., Taillades, G. & Pradel, A. Non-Arrhenius conductivity in glassy and crystallized fast ion conductors a manifestation of cationic disorder. *Solid State Ionics* **105**, (1998).

19. Kuwata, N., Saito, T., Tatsumisago, M., Minami, T. & Kawamura, J. Non-Arrhenius ionic conductivity in α-AgI-stabilized composites and rapid quenched glasses. in *Solid State Ionics* vol. 175 (2004).

20. Murugavel, S. Origin of non-Arrhenius conductivity in fast ion conducting glasses. *Phys. Rev. B - Condens. Matter Mater. Phys.* **72**, (2005).

21. Kincs, J. & Martin, S. W. Non-arrhenius conductivity in glass: Mobility and conductivity saturation effects. *Phys. Rev. Lett.* **76**, (1996).

22. Costigliola, L., Heyes, D. M., Schrøder, T. B. & Dyre, J. C. Revisiting the Stokes-Einstein relation without a hydrodynamic diameter. *J. Chem. Phys.* **150**, (2019).

23. Puosi, F., Pasturel, A., Jakse, N. & Leporini, D. Communication: Fast dynamics perspective on the breakdown of the Stokes-Einstein law in fragile glassformers. *J. Chem. Phys.* **148**, (2018).

24. Kumar, S. K., Szamel, G. & Douglas, J. F. Nature of the breakdown in the Stokes-Einstein relationship in a hard sphere fluid. *J. Chem. Phys.* **124**, (2006).

25. Tarjus, G. & Kivelson, D. Breakdown of the Stokes-Einstein relation in supercooled liquids. *J. Chem. Phys.* **103**, (1995).

26. Ojo, A. T. & Lee, P. I. A Mechanistic Model for Predicting the Physical Stability of Amorphous Solid Dispersions. *J. Pharm. Sci.* **110**, 1495–1512 (2021).

27. Xu, X. L., Douglas, J. F. & Xu, W. S. Thermodynamic-Dynamic Interrelations in Glass-Forming Polymer Fluids. *Macromolecules* **55**, 8699–8722 (2022).

28. Ohno, H. Functional design of ionic liquids. *Bull. Chem. Soc. Jpn.* **79**, 1665–1680 (2006).

29. Shmukler, L. E., Fedorova, I. V, Fadeeva, Y. A. & Safonova, L. P. The physicochemical properties and structure of alkylammonium protic ionic liquids of RnH4-nNX (n=1-3) family. A mini-review. *J. Mol. Liq.* **321**, 114350 (2021).

30. Tolstikhin, I. & Hofmann, A. W. Early crust on top of the Earth's core. *Phys. Earth Planet. Inter.* **148**, 109–130 (2005).

31. Gonnermann, H. M. Magma Fragmentation. *Annu. Rev. Earth Planet. Sci.* **43**, 431–458 (2015).

32. Freed, K. F. The Descent into Glass Formation in Polymer Fluids. *Acc. Chem. Res.* **44**, 194–203 (2011).

33. Mahato, S., Zhu, Z. W. & Sun, D. W. Glass transitions as affected by food compositions and by conventional and novel freezing technologies: A review. *Trends Food Sci. Technol.* **94**, 1–11 (2019).

34. Valenti, S., Cazorla, C., Romanini, M., Tamarit, J. L. & Macovez, R. Eutectic Mixture Formation and Relaxation Dynamics of Coamorphous Mixtures of Two Benzodiazepine Drugs. *Pharmaceutics* **15**, 196 (2023).

35. Kieffer, J. Structural Transitions in Glasses and Glass-Forming Liquids (Morey Award Lecture). *Ceram. Bull.* **81**, 73–78 (2002).

36. Takamori, T. & Tomozawa, M. Viscosity and Microstructure of Phase-Separated Borosilicate Glasses. *J. Am. Ceram. Soc.* **62**, 373–377 (1979).

37. Kelton, K. F. Kinetic and structural fragility-a correlation between structures and dynamics in metallic liquids and glasses. *J. Physics-Condensed Matter* **29**, 23002 (2017).

38. Yang, M. *et al.* Research progress on high-entropy bulk metallic glasses. *Sci. Sin. Mech. Astron.* **50**, 67003 (2020).

39. Varshneya, A. K. & Mauro, J. C. *Fundamentals of inorganic glasses. Fundamentals of Inorganic Glasses* (2019). doi:10.1016/C2017-0-04281-7.

40. LEWIS, M. H., METCALF-JOHANSEN, J. & BELL, P. S. Crystallization Mechanisms in Glass-Ceramics. *J. Am. Ceram. Soc.* **62**, (1979).

41. Martendal, C. P. & de Oliveira, A. P. N. Glass viscosity at crystallization temperature: an approach. *J. Therm. Anal. Calorim.* **130**, (2017).

42. Dubey, K. S., Ramachandrarao, P. & Lele, S. Thermodynamic and viscous behaviour of undercooled liquids. *Thermochim. Acta* **280**, 25–62 (1996).

43. Sidebottom, D. L. Connecting Glass-Forming Fragility to Network Topology. *Front. Mater.* **6**, 144 (2019).

44. Wang, L. M., Liu, R. P. & Tian, Y. J. On glass formation thermodynamics: Enthalpy vs. Entropy. *Acta Phys. Sin.* **69**, 196401 (2020).

45. Xu, W. S., Douglas, J. F. & Sun, Z. Y. Polymer Glass Formation: Role of Activation Free Energy, Configurational Entropy, and Collective Motion. *Macromolecules* vol. 54 (2021).

46. Eyring, H. Viscosity, plasticity, and diffusion as examples of absolute reaction rates. *J. Chem. Phys.* **4**, (1936).

47. Rosa, A. C. P., Cruz, C., Santana, W. S., Brito, E. & Moret, M. A. Non-Arrhenius behavior and fragile-to-strong transition of glass-forming liquids. *Phys. Rev. E* **101**, 42131 (2020).

48. Silva, V. H. C., Aquilanti, V., de Oliveira, H. C. B. & Mundim, K. C. Uniform description of non-Arrhenius temperature dependence of reaction rates, and a heuristic criterion for quantum tunneling vs classical non-extensive distribution. *Chem. Phys. Lett.* **590**, 201–207 (2013).

49. Angell, C. A. Structural instability and relaxation in liquid and glassy phases near the fragile liquid limit. *J. Non. Cryst. Solids* **102**, (1988).

50. Angell, C. A. Strong and Fragile Liquids Relaxations in Complex Systems. in *National Technical Information Service, US Department of Commerce* 3–11 (1984).

51. Angell, C. A., Dworkin, A., Figuiere, P., Fuchs, A. & Szwarc, H. Strong and fragile plastic crystals. *J. Chim. Phys.* **82**, (1985).

52. Böhmer, R., Ngai, K. L., Angell, C. A. & Plazek, D. J. Nonexponential relaxations in strong and fragile glass formers. *J. Chem. Phys.* **99**, (1993).

53. Angell, C. A. Formation of glasses from liquids and biopolymers. *Science (80-.).* **267**, (1995).

54. Arrhenius, S. Über die Reaktionsgeschwindigkeit bei der Inversion von Rohrzucker durch Säuren. *Zeitschrift für Phys. Chemie* **4U**, (1889).

55. Böhmer, R. & Angell, C. A. Correlations of the nonexponentiality and state dependence of mechanical relaxations with bond connectivity in Ge-As-Se supercooled liquids. *Phys. Rev. B* **45**, (1992).

56. Schlexer, P. Computational Modeling in Heterogeneous Catalysis. *Ref. Modul. Chem. Mol. Sci. Chem. Eng.* (2017) doi:10.1016/B978-0-12-409547-2.14273-8.

57. Hospital, A., Goñi, J. R., Orozco, M. & Gelpí, J. L. Molecular dynamics simulations: Advances and applications. *Advances and Applications in Bioinformatics and Chemistry* vol. 8 (2015).

58.   Damasceno, D. A., Mesquita, E. & Rajapakse, R. N. K. D. Mechanical behavior of nano structures using Atomic-Scale Finite Element Method (AFEM). *Lat. Am. J. Solids Struct.* **14**, (2017).

59.   Frenkel, D. & Smit, B. *Understanding Molecular Simulation: From Algorithms to Applications. Understanding Molecular Simulation* (2002).

60.   Allen, M. P. & Tildesley, D. J. *Computer simulation of liquids: Second edition. Computer Simulation of Liquids: Second Edition* (2017). doi:10.1093/oso/9780198803195.001.0001.

61.   Tang, J. *et al.* Activation volume dominated diffusivity of Ni50Al50 melt under extreme conditions. *Comput. Mater. Sci.* **171**, (2020).

62.   Dove, M. T. Introduction to lattice dynamics. *Introd. to lattice Dyn.* (1993) doi:10.1119/1.17708.

63.   Prony, G. R. B. *Essai Expérimental Et Analytique. Journal de L'Ecole Polytechnique,* (1795).

Chapter 2 Diffusive Behavior in a Lattice-Solute Model Solid-State Electrolyte and the Importance of Anharmonicity

Original Publications Information

The work in this chapter was published in Computational Materials Science as:

Beg, C. & Kieffer, J. Anharmonicity and the emergence of diffusive behavior in a lattice-solute model solid-state electrolyte. *Comput. Mater. Sci.* **228**, 112359 (2023).

Abstract

We have investigated atomic transport properties in a simple two-component solid-state material using molecular dynamics simulations. This model system is composed of a lattice element and a solute. The former is modeled after carbon, which forms a covalent diamond lattice that provides the supporting structure for the solute, which interacts with carbon and with itself via Lennard-Jones potentials. The size of the solute species is systematically varied while maintaining a constant system volume. The change in solute particle size is quantified using an atomic packing fraction, which is used as a mediator variable to find relationships between the internal pressure of the system, its vibrational properties, and the change in diffusivity of the mobile species. The data imply a causal relationship between structural instabilities, reflected in the internal pressure and compressibility curves, the vibrational spectra, and the onset of a diffusive regime manifest in an increase in atomic mobility by orders of magnitude.

2.1 Introduction

The fact that singularly well performing materials have been discovered in category of solid-state electrolyte suggests that the ionic conductivity of a material cannot be simply gauged from the constituting elements and the type of bonding between them, but that structural subtleties are equally responsible for the creation of low-activation energy passageways. To identify these outstanding electrolytes more reliably requires a better understanding of what constitutes a low-activation energy pathway in a molecular structure. To this end, it is helpful to begin by exploring a simpler model system that reduces the number of confounding variables and interactions that make analysis and understanding of more complex materials so elusive. Hence, the purpose of the current work is to explore how the interactions between the mobile species and the supporting structure affect the mobility of the former. This is accomplished by studying atomic diffusion in a simple lattice-solute model system using molecular dynamics (MD) simulations. We begin by using standard methods to calculate and characterize diffusion rates while varying the solute site occupancy fraction and size of the mobile species, before moving on to investigating the relationship between internal pressure and diffusion. Then we explore the vibrational spectrum for this system and how key features of the spectra relate to local particle dynamics before tying everything together through the revelation of a necessary structural condition for the emergence of high solute mobility is a solid material.

2.2 Methodology

2.2.1 Lattice-Solute System

The model system we study is designed to reduce structural complexity to a minimum and therefore consists of just two components: one species that forms a continuous covalent network,

providing a supporting structure for the second mobile species with which it interacts non-covalently. The network is composed of an 8 x 8 x 8 supercell of 4096 carbon atoms in a diamond lattice governed by a Tersoff bond order potential.[1] The solute species is a set of atoms with the mass of lithium, 6.941 amu, that interact with one another and with the network as described by a Lennard-Jones potential,

$$V_{ij} = 4\varepsilon \left(\left(\frac{\sigma}{r_{ij}} \right)^{12} - \left(\frac{\sigma}{r_{ij}} \right)^{6} \right) \qquad r_{ij} < r_c \tag{2.1}$$

where σ is the zero-crossing distance for the potential relating to the size of the particle, ε is the dispersion energy corresponding to the depth of the potential well, r_{ij} is the interparticle distance between interacting particles i and j, and r_c is the cutoff distance beyond which particles i and j do not interact. While the dispersion energy, ε, is 15 kcal/mol (62.76 kJ/mol) for all simulations, both the number of solute atoms and the other interaction parameters are varied throughout the study. The solute atoms interact with one another in a purely repulsive manner using a Lennard-Jones potential with the cutoff distance set equal to the location of the potential minimum, which is essentially a soft sphere potential.[2] This ensures that solute atoms do not exhibit the tendency to form clusters, while prohibiting spatial overlap at close distances. This system can be viewed as an interspersion of two lattices, the principal lattice being formed by the rigid network of covalent species and the sublattice being occupied by the conductive modifier, without the added complexity of a charge-compensating third species. All MD simulations are performed using the Large-scale Atomic/Molecular Massively Parallel Simulator code (LAMMPS).[3] Simulations are initialized with carbon atoms positioned at lattice positions characteristic of diamond and solute atoms generated at random positions within the supercell. A conjugate gradient energy minimization is performed to move solute atoms to a more stable low energy configuration and ensure stability upon starting the simulation.[4] Boltzmann distributed velocities are assigned to all

atoms corresponding to a temperature of 300 K. A time step of 1 femtosecond is used for time integration of the equations of motion. The system is relaxed for 700 picoseconds in the NPT ensemble, followed by another 300 picoseconds in the canonical ensemble, before a production run for 300 picoseconds also in the canonical ensemble. Temperature and pressure, where necessary, are regulated via a Nose-Hoover thermostat and barostat and with periodic boundary conditions are applied.[5–8]

To familiarize with the system, we first describe its key physical characteristics. While algorithmically all MD simulations to collect statistical measures for analysis are carried out in the canonical ensemble (constant number of particles, volume, and temperature, or NVT-ensemble), the principal parameter we change for each simulation is the size of the solute species. In isolation, the size of an atom or ion is difficult to ascertain, and hence atomic sizes are commonly derived from the space they occupy in crystalline compounds, which does not yield a universally applicable measure, but suffices in the present context, as we are only considering two elements in this study. For this purpose, we define the ideal space required for an atom as the one where it is neither attracted to nor repelled by its neighbors, that is, the lowest possible ground state where all interatomic forces are zero (not just balanced). Practically, this entails adjusting the volume of the system until the pressure vanishes. This is the volume we are using for all simulations described in the following. Furthermore, in this configuration, the radius of the carbon atom is 0.77 Å (half of the carbon-carbon bond distance). When all tetrahedral interstices are occupied by a solute atom, this turns out to also be the radius of the solute atom under the requisite zero-pressure condition since it occupies tetrahedral interstices in a diamond lattice.

38

As described by the Lennard-Jones potential, the solute-carbon interatomic spacing is predominantly determined by the σ parameter. Evidently, σ does not directly translate into the atomic radius, since in a condensed phase multiple atoms interact simultaneously. Therefore, the lowest energy fully occupied configuration and at zero pressure, $\sigma = 1.4436$ Å, corresponds to a solute particle radius of 0.77 Å, based on the size of the interstice it fills. We consider this to be the reference size of the solute species. For our parametric study we vary the size of the solute species from 0.26 Å to 0.80 Å, simply by scaling the σ parameter, thus creating structures whose internal stresses change between tensile to compressive. Note that, throughout these changes, the size of carbon atoms, the volume of the system, and therefore its density, remain constant. By scaling the size of the solute particle, while that of the covalently bonded species remains constant, we create conditions that predominantly affect the dynamics of the solute atom. This is because the covalent bond is much stronger than the solute-carbon interactions, so that the carbon-carbon distances are essentially unchanged as the solute particle size is varied. Consequently, when the solute atom is large its location becomes strongly constrained, whereas when it is small, the solute atom has nominally more space to move within and between sites. The fact that, depending on its size, the environment of the solute atom is more or less spacious, is quantified by using the concept of solute atom packing fraction ϕ_S, defined as

$$\phi_S = \frac{4\pi}{3} \frac{(N_S \cdot r_S^3)}{V} \tag{2.2}$$

where we assume a spherical shape for the atoms, N_S is the number of solute atom sites per unit cell, respectively, r_S is the solute atom's radius, and V is the volume of the crystalline unit cell. Note that this packing fraction is a nominal quantity designed to account for the local space accessible by the solute; it does not consider actual site occupation probabilities. Because of the

rigid carbon-carbon bonds, solute sites retain their shape and size, regardless of whether they are occupied or not.

2.2.2 Internal Energy and Structural Disorder

To ascertain the uniqueness of the above definition of the solute reference size, we conduct a more in-depth analysis. When determining the reference value of r_S, one choice is to initialize the conjugate gradient energy minimizations with solute atoms at their ideal lattice positions, where each solute is surrounded by a first coordination shell of 4 carbon atoms forming a tetrahedron and a second coordination shell of 6 carbon atoms forming an encompassing octahedron. This solute sublattice is identical, though spatially offset, from the carbon diamond lattice. A perfect sublattice also requires that it be fully occupied, i.e., the number of solute atoms is equal to the number of network atoms. With this starting configuration, the energy minimization procedure, performed using the Hessian-free truncated Newton algorithm, yields no significant shift in solute positions, regardless of the solute size.[9] This means that these sublattice positions are local energy minima. Alternatively, when initializing configurations with the same number of solute atoms at random positions, as revealed in **Figure 2-1**, the sublattice positions only constitute the minimum energy configuration for sufficiently large ϕ_S. In fact, for the large solute sizes, starting the energy minimization from random positions, the procedure no longer reaches the lowest possible energy because solute atoms become jammed with the covalent lattice slightly distorted. Conversely, for low ϕ_S, minimization from a random configuration produces a disordered solute structure that is characterized by a lower energy than that of the ordered sublattice.
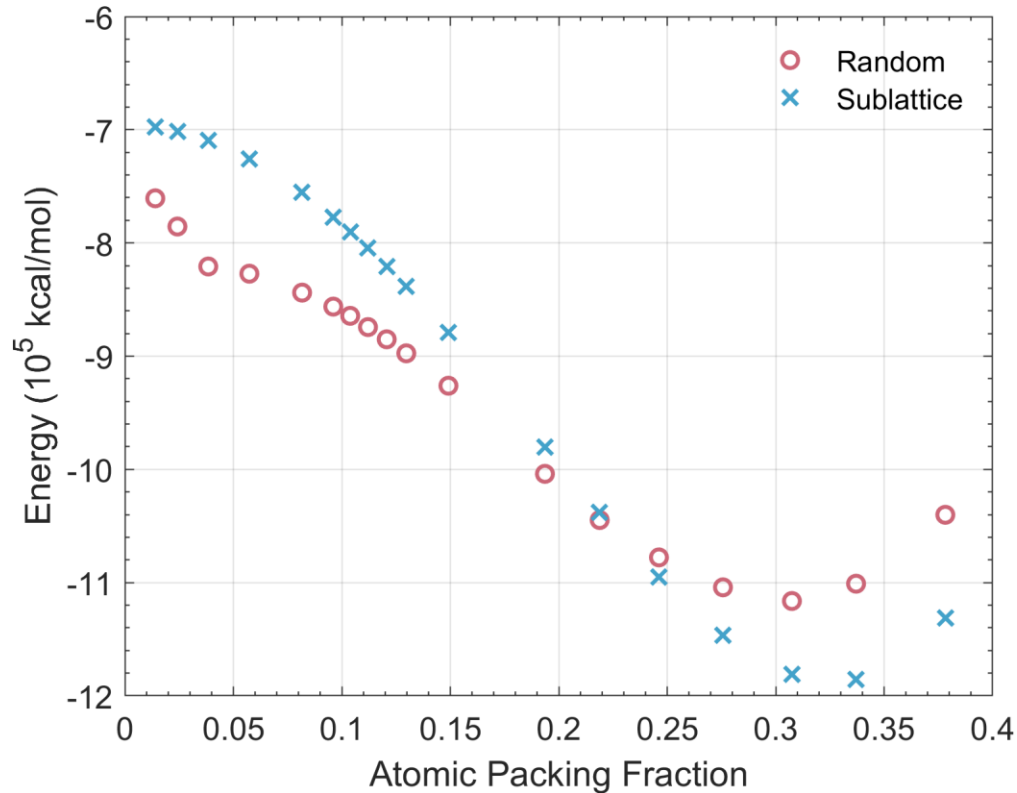
Figure 2-1 Potential energy of the system as a function of atomic packing fraction (**Equation 2.2**). Energies are calculated both for configurations where the solute species are located at lattice sites (blue) and where they are repositioned upon energy minimization from random initial positions (red).

The most stable configurations are achieved at $\phi_S = 0.337$ for the ordered sublattice and 0.307 for the random system. The atomic packing fraction for the ordered sublattice is approximately half that of a body-centered cubic (BCC) crystal lattice. This is because filling the sublattice of a diamond crystal results in particle positions equivalent to that of a BCC lattice. The crystal unit cell is not truly a BCC lattice, however, because the species of atoms that occupy each lattice position reverse in each adjacent unit cell.

2.2.3 Internal Pressure and Equation of State

Reducing the size of atoms based on the way they interact with others is equivalent to increasing the amount of void space in the structure, and consequently, lowering their number density as measured by their contributions to the virial expansion describing the system. These changes are

manifest in the calculated internal pressure, as shown in **Figure 2-2** where the pressure is plotted

vs. ϕ_S for both energy-minimized systems.
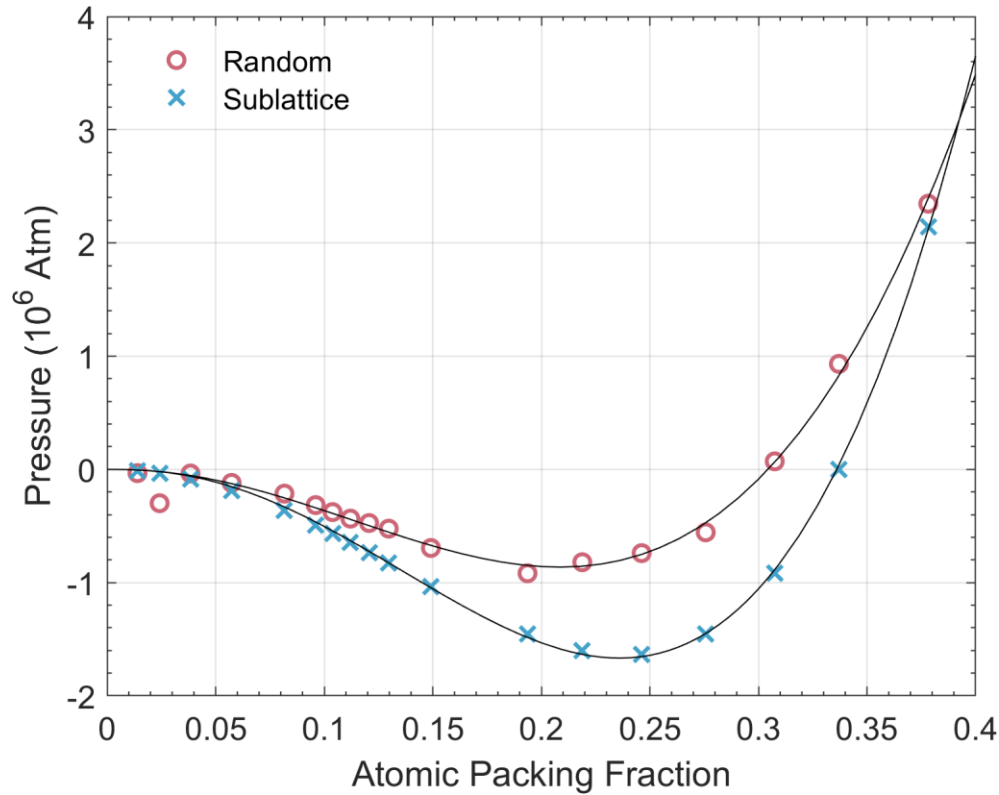
Figure 2-2 Internal pressure of the system as a function of atomic packing fraction (**Equation 2.2**). Pressures are calculated both for configurations where the solute species are located at lattice sites (blue) and where they are repositioned upon energy minimization from random initial positions (red). The black curves fitting each data set are calculated using the Anton-Schmidt equation of state (**Equation 2.3**).

Both curves have a similar shape, though the system obtained from random initial positions

possesses a shallower negative pressure region. At high ϕ_S values the repulsion between atoms

gives rise to large positive pressures, i.e., compressive stress. With decreasing ϕ_S the pressure

drops, eventually turning negative, indicating tensile stress. The zero-pressure locations where

the systems are neither under tensile nor compressive stress coincide with the minima in the

energy curves. As ϕ_S continues to decrease, the pressure reaches a minimum corresponding to the

largest tensile stress, or tensile limit. At this point, the solute ceases to contribute to the cohesive

fabric across the structure, i.e., it no longer transmits forces across the interstice in which it

resides in a balanced way. Instead, the solutes settle near one facet of the interstice, which allows them to lower their potential energy, releasing tensile interactions and causing the internal pressure to rise. In the limit of very low ϕ_S, the pressure asymptotically approaches zero as the fragments reach mechanical equilibrium.

The pressure vs. ϕ_S curves are fit using the Anton-Schmidt equation of state. This equation is chosen for its demonstrated success in reproducing the pressure-volume relationship for crystalline solids even for large deviations from the reference volume.[10,11] For our purposes, the volume ratio terms in the equation are replaced with the ratios of atomic packing fractions. The modified expression is

$$P(\phi_S) = K \left(\frac{\phi_S}{\phi_S^0}\right)^{\left(\frac{1}{6}+\gamma\right)} \cdot \ln\left(\frac{\phi_S}{\phi_S^0}\right) \tag{2.3}$$

where P is the internal pressure of the system, ϕ_S^0 is the reference atomic packing fraction at $P(\phi_S^0) = 0$, K is the bulk modulus at the reference atomic packing fraction, and γ is the Grüneisen parameter. The Grüneisen parameter is a factor describing how the vibrational frequencies of atoms in a solid change with the volume of the material

$$\gamma_i(q) = -\frac{\partial \ln \omega(q_i)_i}{\partial \ln V} \tag{2.4}$$

where q is the phonon wavevector, $\omega(q)_i$ is the frequency of the ith mode of vibration, and V is the volume.[12,13] For a harmonic system where the restoring force is linear with displacement, the Grüneisen parameter is exactly zero. The values of K, ϕ_S^0, and γ for the random system are 629 GPa, 0.3044, and 2.643 and for the ordered system they are 1299 GPa, 0.3361, and 2.829, respectively. The bulk modulus of diamond at standard conditions is 445 GPa. It is apparent that the bulk moduli for the systems presented here are considerably larger. This is because the structures we are exploring here represent stuffed diamond lattices, possessing double the atomic

number density of a true diamond. This is apparent in the values of ϕ_S^0 which are of the same order as the atomic packing fraction of pure diamond (0.34). It is known that elastic moduli increase with density so one should expect this doubling of density to result in a substantial increase in stiffness and a higher bulk modulus.[14]

By design, the solute-solute interactions are purely repulsive. By themselves, the solute species do not exhibit any cohesive quality. However, they can propagate compressive impulses, the extent to which being determined by the value of σ in the truncated Lennard-Jones potential governing solute-solute soft-sphere interactions. Here we briefly discuss the choice of the value of σ, which is based on a thorough preliminary investigation and is henceforth kept constant at a value of 1 Å. In **Figure 2-3**, the pressure vs. ϕ_S curves for systems minimized from random initial configurations with solute-solute σ values of 0.9, 1.0, and 1.1 Å are shown. Note that changes in the solute-solute σ value for the system minimized from the ordered sublattice have no effect on internal pressure for the range investigated and are therefore not displayed in the figure. This is because the solute atoms in the ordered system are placed in local minima separated by a greater distance than of the repulsive cutoff distance. Conversely, for the system minimized from a random initial configuration, it is apparent that changing the solute-solute σ value does influence the pressure for sufficiently high packing densities, those at or greater than approximately $\phi_S = 0.194$, beginning in the vicinity of the internal pressure minimum. In this range, increasing the solute-solute repulsive distance raises the overall stiffness of the structure, as impinging solute particles push one another toward the walls of their local network cavity. We show below that these effected densities are well outside the diffusive regime and the configurations of interest for this study are insensitive to the solute-solute σ value.
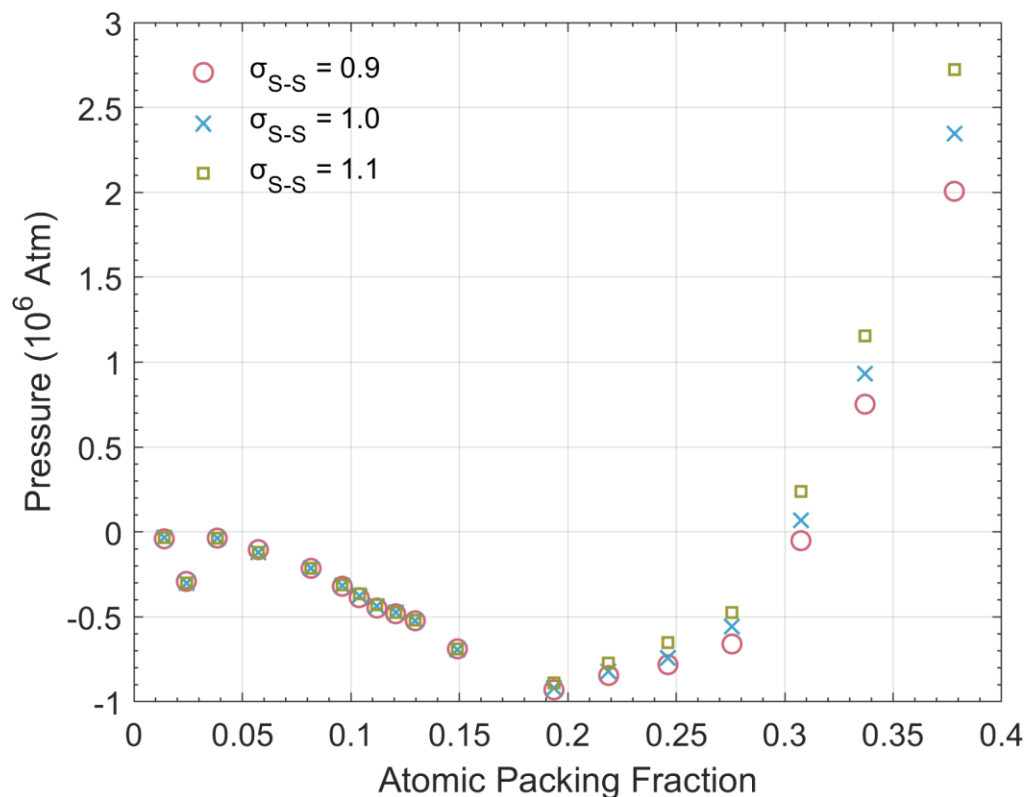
Figure 2-3 Internal pressure of the system for different atomic packing fractions as a function of the parameter, σ, in the Lennard-Jones potential. This value governs the extent of solute-solute repulsion. The solute species are at positions reached upon energy minimization from a random initial configuration.

2.2.4 Methods of Analysis

Our main interest is in the transport properties of the solute species. Perhaps the most common approach to characterizing atomic mobility in MD simulations is to evaluate the diffusion coefficients. This is accomplished based on calculating the mean squared displacement (MSD) or the velocity autocorrelation function (VACF) associated with atomic trajectories.

Mean Squared Displacement — The ensemble-averaged MSD of particles collected over the course of a simulation yields the diffusivity based on the following relationship,

$$D = \lim_{t \to \infty} \frac{\langle |\vec{r}(t) - \vec{r}(0)|^2 \rangle}{2d \cdot t}, \tag{2.5}$$

where $r(0)$ is the particle position at the time origin, $r(t)$ is the particle position at a subsequent time t, and d is the dimensionality of the system. For adequately sampled atomic trajectories, the

MSD typically exhibits a ballistic regime at short times and a diffusive regime at times when correlation between atomic jumps is effaced by randomization of trajectories. Accordingly, the diffusivity is obtained from the slope of the MSD vs. time in the diffusive regime, characterized by compelling linearity in the relationship between MSD and time. For our system of interest, particle position data for the "unwrapped" particle coordinates is stored every ten femtoseconds for the duration of the production run. Unwrapped particle coordinates refer to those for which the simulation box length is not subtracted when the particles pass through a periodic boundary and reenter the opposite side of the simulation box.

Velocity Auto-Correlation Function — Provided knowledge of the velocity of each particle as a function of time, the MSD can be expressed by integrating these velocities over time. Further manipulation of the resulting expression yields the VACF formalism, which given adequate statistics, yields the same result as the analysis of MSD. Interestingly, though, MSD and VACF produce this information by examining different time regimes.[15] Specifically, with the VACF analysis of a dynamical processes we quantify the decay in correlation of a particle's velocity with itself over time, i.e., the loss of predictability in the particles' motion. In other words, we tally the buildup towards randomness in particle trajectories during the ballistic regime until trajectories transition from periodic to diffusive. Accordingly, adding up incremental losses from the harmonic oscillatory character of motion is sufficient to account for a species' capacity for random drift. Hence, MSD and VACF are complementary in the way they assess atomic mobility, and discrepancies between the obtained with each construct may be indicative of systemic non-idealities.

Numerically, computing the VACF involves taking the ensemble average across multiple time origins of the inner products of each particle's velocity vector at the time origin with its velocity

vector at each subsequent timestep. The decorrelation in this value results from the transfer of momentum between the reference particle and its surrounding particles. The time integration of the VACF yields the diffusion coefficients as

$$D = \frac{1}{d} \int_0^\infty \langle \vec{v}(0) \cdot \vec{v}(t) \rangle dt \tag{2.6}$$

where $v(0)$ is the velocity vector of a particle at the time origin, $v(t)$ is the velocity vector of the same particle at a subsequent time t, and d is, again, the dimensionality of the system. **Equation 2.6** is one of the Green-Kubo relations that connect the integration of time correlation functions to transport coefficients. Since the VACF can neither be collected nor integrated to infinite time, the method relies on the oscillatory character of the VACF to substantially subside within accessible times, typically a few picoseconds. This also allows for more averaging since, with the same amount of velocity data, a greater number of time origins can be used for shorter VACFs. For the system at hand, 5,120,000 velocity vectors are stored where this value is the product of the number of solute particles in the system with the number of timesteps over which velocity data was collected. The accrued velocity data is post-processed in MATLAB version 9.10.0.1669831 (R2021a) where the VACF is calculated. The number of time origins used is modulated to maximize the amount of averaging while maintaining a solute VACF length of approximately 2.5 picosecond by which time sufficient decorrelation has occurred.

Vibrational Spectrum — In the zero-temperature limit, the Fourier Transform of the VACF yields the vibrational density of states for the system

$$\varphi(\omega) = \int_0^\infty \langle \vec{v}(0) \cdot \vec{v}(t) \rangle e^{-i\omega t} dt \tag{2.7}$$

where i is the imaginary unit and ω is the angular frequency. However, at finite temperature, such as in these simulations, this relationship is not strictly true. The Fourier Transform of the VACF in this case still results in a vibrational spectrum, but it is only an approximation of the

vibrational density of states as translational motion of particles is present and the anharmonicity of the interatomic potentials governing particle interactions is not negligible, i.e., the harmonic approximation is not valid.[16] The zero-frequency value of the spectrum divided by the dimensionality also yields the diffusion coefficient as it results in an expression identical to **Equation 2.6**. Diffusion can only occur in a system with an anharmonic potential because this type of potential allows for the energy-induced escape of particles while true harmonic potentials, binding particles in potential wells whose energies tend toward infinity in all directions, do not exist in nature. The vibrational frequency of an oscillator is related to the second derivative of the governing potential energy function and its mass. When the oscillator is harmonic, this second derivative of the potential energy is referred to as the force constant and is a proportionality constant between the force felt by the oscillator and its position. However, for an anharmonic potential the relationship between the force on a particle and its position within the potential is nonlinear. In this case, simple vibrational frequency analyses based on Hooke's law are not valid, and the oscillator frequency becomes amplitude dependent. For atomic systems, this means the vibrational frequency of a given atom will be a function of its kinetic energy or, viewed macroscopically, its temperature. For an atom existing in a truly static environment this would be the full story, but for real systems, the local environment around an atom is moving on average often just as much as the reference atom. Therefore, the picture becomes much more complicated due to the chaotic motion that occurs from the persistent collisions of the atom with its neighboring particles. Equivalently, this can be viewed as an atom moving through a tumultuous, dynamic potential energy surface resulting from the chaotic motion of the surrounding particles that constitute its local environment.

2.3 Results and Discussion

2.3.1 Solute Diffusivity vs. Solute Site Occupancy Fraction

To determine the extent to which solute site occupancy fraction affects diffusion, we vary the number of solute atoms between 64 and 2048, while the number of network atoms is held constant at 4096. The diffusivity is calculated using both the MSD and VACF formalisms, and the results show good agreement between the methods. From **Figure 2-4** it is apparent that the diffusivity decreases severalfold, approximately linearly, with increasing solute concentration for the range studied.
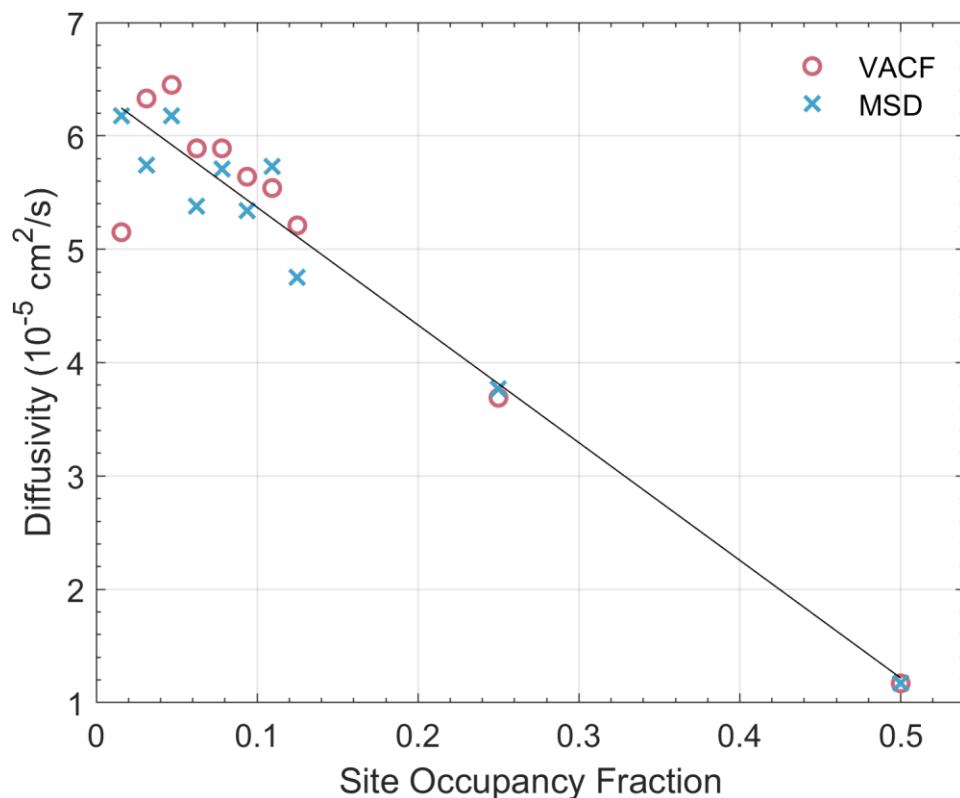
Figure 2-4 Solute diffusivity as a function of the lattice site occupancy fraction. Unit occupancy corresponds to an equal number of solute and network atoms.

This decrease in diffusivity with increasing solute site occupancy likely results from the increased probability of solute-solute collisions leading to more failed diffusive jumps and

increased solute confinement.[17] The linear relationship between diffusion coefficient and solute

concentration becomes noisier for low solute concentrations in part due to poor statistics from

the limited number of solute atoms. For the remainder of the dynamics simulations in the study,

we chose to fix the number of solute atoms at 1024, or a ratio of solute to network atoms of 0.25,

because this represents a favorable tradeoff between good statistics and lower compute time.

2.3.2 Diffusivity

We next explore how variation in the effective size of the solute particles impacts diffusion. As

is evident in the semi-log plot of **Figure 2-5**, changes in value of ϕ_S have a much greater effect

on diffusion than variation in the concentration of solute atoms, with diffusivities spanning

several orders of magnitude for the range studied.
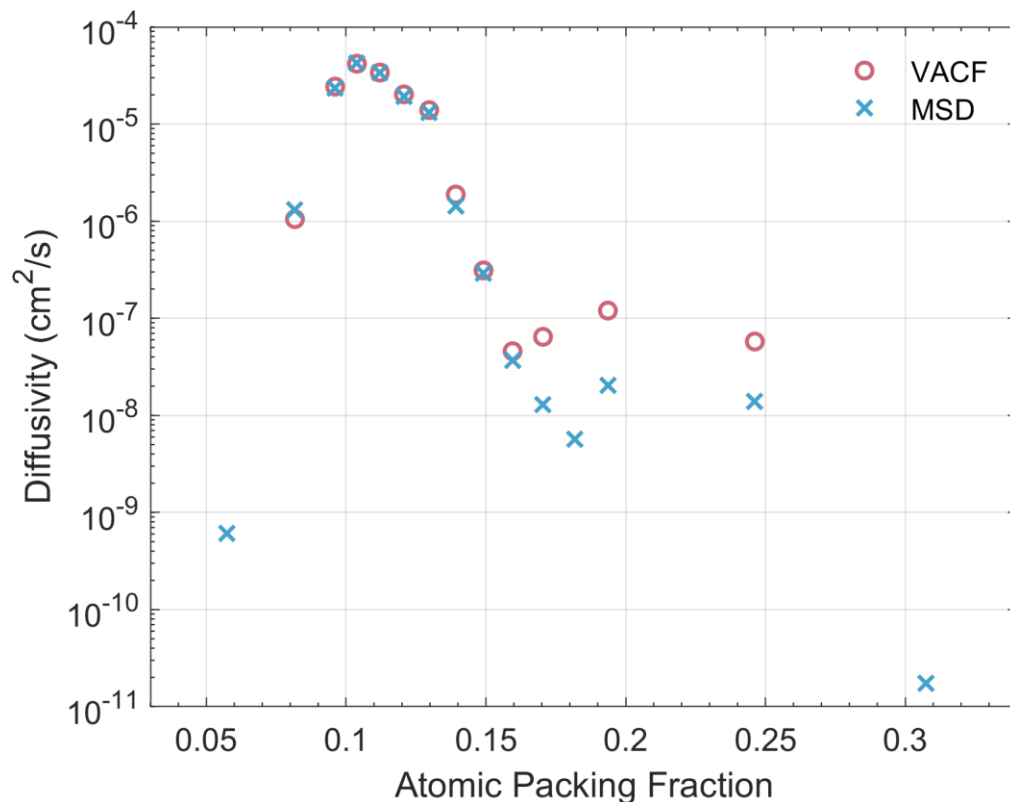
Figure 2-5 Solute diffusivity as a function of atomic packing fraction (**Equation 2.2**), calculated using both MSD (blue) and VACF (red) methods.

Specifically, descending in ϕ_S values, we observe a sharp onset of diffusion around $\phi_S \sim 0.149$. Maximum diffusivity is reached in the vicinity of $\phi_S = 0.104$. The effect of ϕ_S on atomic mobility is so pronounced because this parameter controls both the total number of particles a solute particle interacts with at a given time, as well as the overlap of those pair potentials and, therefore, the shape and depth of the effective potential well. This means that even with the pairwise bonding energy held constant, varying solute size has a dramatic effect on the potential energy landscape and therefore the energy felt by each solute particle. As is already known, the relationship between energy of activation and diffusion is of exponential form, giving a rationale for the trend seen in **Figure 2-5**.

2.3.3 Velocity Auto-Correlation Functions and Vibrational Spectra

The abrupt change in solute mobility near $\phi_S = 0.149$ is reflected in the features of the VACF and of the vibrational spectrum for the system containing 1048 mobile solute atoms and 4096 carbon network atoms as well. In **Figure 2-6 (a)** we compare a series of solute VACFs for ϕ_S values bracketing the mobility transition towards higher and lower values. At the transition, the VACF oscillates slowly and decays smoothly, whereas the farther away from the transition, the more strongly VACFs exhibit higher frequency modes that persist for longer times, giving the VACFs a visually complex appearance. This effect seems corollary to features in the corresponding vibrational spectra in **Figure 2-6 (b)**. The vibrational spectrum corresponding to the VACFs near the mobility transition possesses a single maximum with a peculiar-shaped tail stretching towards high frequencies (further discussed below). This apparent simplicity results from the presence of a large number of vibrational modes, closely stacked in frequency, and whose intensities decrease gradually the further the frequency is from that of the most prominent mode.
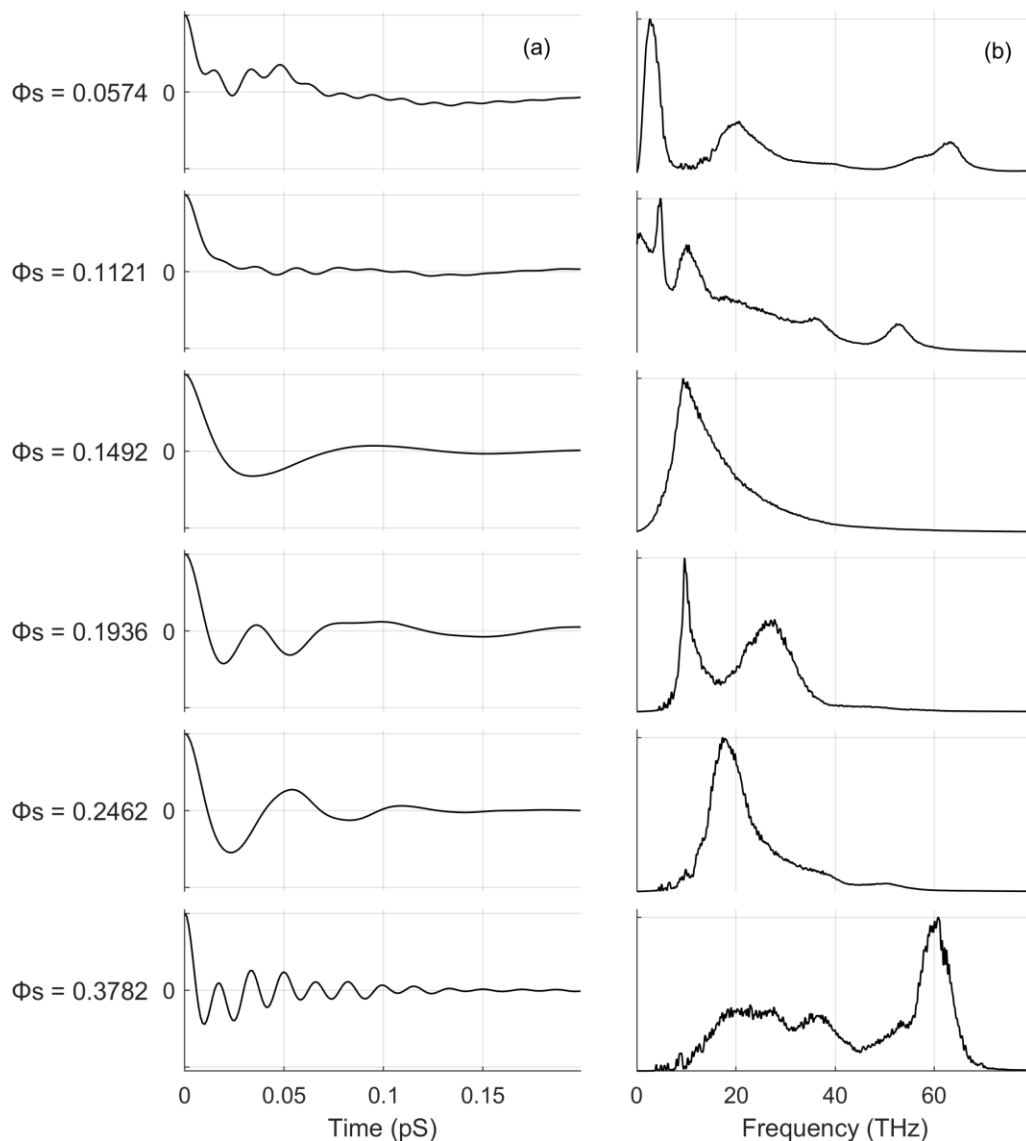
Figure 2-6 Velocity auto-correlation functions for the solute species at various atomic packing fractions (a), and corresponding vibrational spectra(b).

Conversely, the spectra corresponding to VACFs to either side of the mobility transition have multiple distinct maxima with comparably narrower band widths, suggesting that in these systems a smaller number of vibrational modes dominate the dynamics of the solute atoms. Finally, systems that exhibit the highest solute mobility, around $\phi_S = 0.104$, exhibit vibrational modes at very low frequencies, providing for a large intercept with the ordinate, which corroborates the high solute diffusivities determined for these systems.

Anharmonicity — The shape of the vibrational spectrum for the system at $\phi_S = 0.149$ stands out. To tease out the underlying reason for this spectral shape we devised a drastically simplified and dynamically transparent system consisting of a single particle, able to move in one dimension but constrained by two fixed particles on either side. This allows us to isolate the spectral elements and essential dynamics from the behavior of our complex three-dimensional many-particle simulations. In the one-dimensional system the mobile particle interacts with each of the two fixed particles via identical Lennard-Jones potentials. In effect, the single central particle simply exists within a composite potential of its two stationary neighbors. The dynamics of this system are explored using a simple MD algorithm. All simulations are initiated with the particle at a distance of 1.54 Å from either of its neighbors as this mirrors the solute-network interparticle distance at stable sublattice positions for the three-dimensional system. The particle is then given a small initial velocity to allow adequate exploration of the potential energy landscape. The system possesses no damping so this initial velocity along with the potential energy represents the total energy of the system, which is constant. Hence, the particle oscillates within the potential with a constant period forever. Therefore, the simulations were allowed to run for 50 oscillatory cycles to collect adequate velocity data to construct VACFs and vibrational spectra with good resolution. Multiple simulations are run with differing values for the σ parameter of the Lennard-Jones potential while keeping interparticle spacing constant, much like what was done previously for the three-dimensional system. The variation of σ modifies the composite potential experienced by the particle, allowing one to adjust the degree of anharmonicity and negative curvature (region of instability) it encounters. For small values of σ, the separate Lennard-Jones potentials overlap minimally producing a composite double-well potential with a high degree of anharmonicity. Upon increasing σ, the component Lennard-Jones potentials

overlap to an increasing degree causing the anharmonicity to decrease and the separate minima in the potentials to eventually merge into a single near-harmonic potential. Values for σ range from 0.5 to 1.5 Å in increments of 0.1 Å. The change in the composite potential energy with σ is shown in **Figure 2-7**.
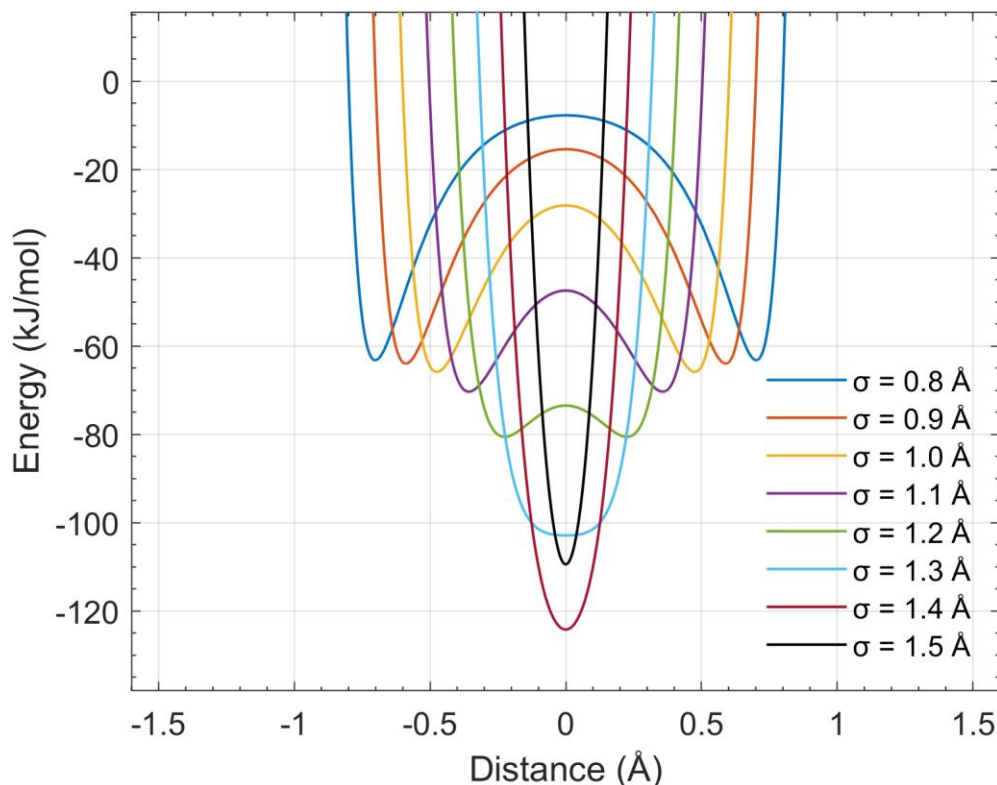
Figure 2-7 Potential energy surface for the solute species in a one-dimensional analog system, with network atoms fixed at ±1.54 Å. σ represents the size of the solute atom within this space.

Inspecting the resultant VACFs in **Figure 2-8 (a)**, a few observations can be made. Because the moving particle is not subject to friction, the VACFs are indefinitely periodic and do not decay. A single particle oscillating in a harmonic potential would produce a single pure cosine wave as its VACF. For large values of σ where the composite potential is nearly harmonic, we can see how this is true. The VACF exhibits one inflection point in between consecutive extrema. However, for decreasing values of σ and, therefore, increasing anharmonicity and regions with negative curvature in the energy landscape, the VACF deviates more and more from that of a

cosine wave. The time between extrema of the VACFs becomes greater and two additional

inflections appear between consecutive extrema, giving rise to a very gradual crossing of the

abscissa, which reflects how the particle motion during the slow traversing of the maximum in

the center of the composite potential correlates with its motion at the turnaround points.

Accordingly, the motion of the particle in the unstable regime of the oscillator is largely

decorrelated from that near the potential minima.
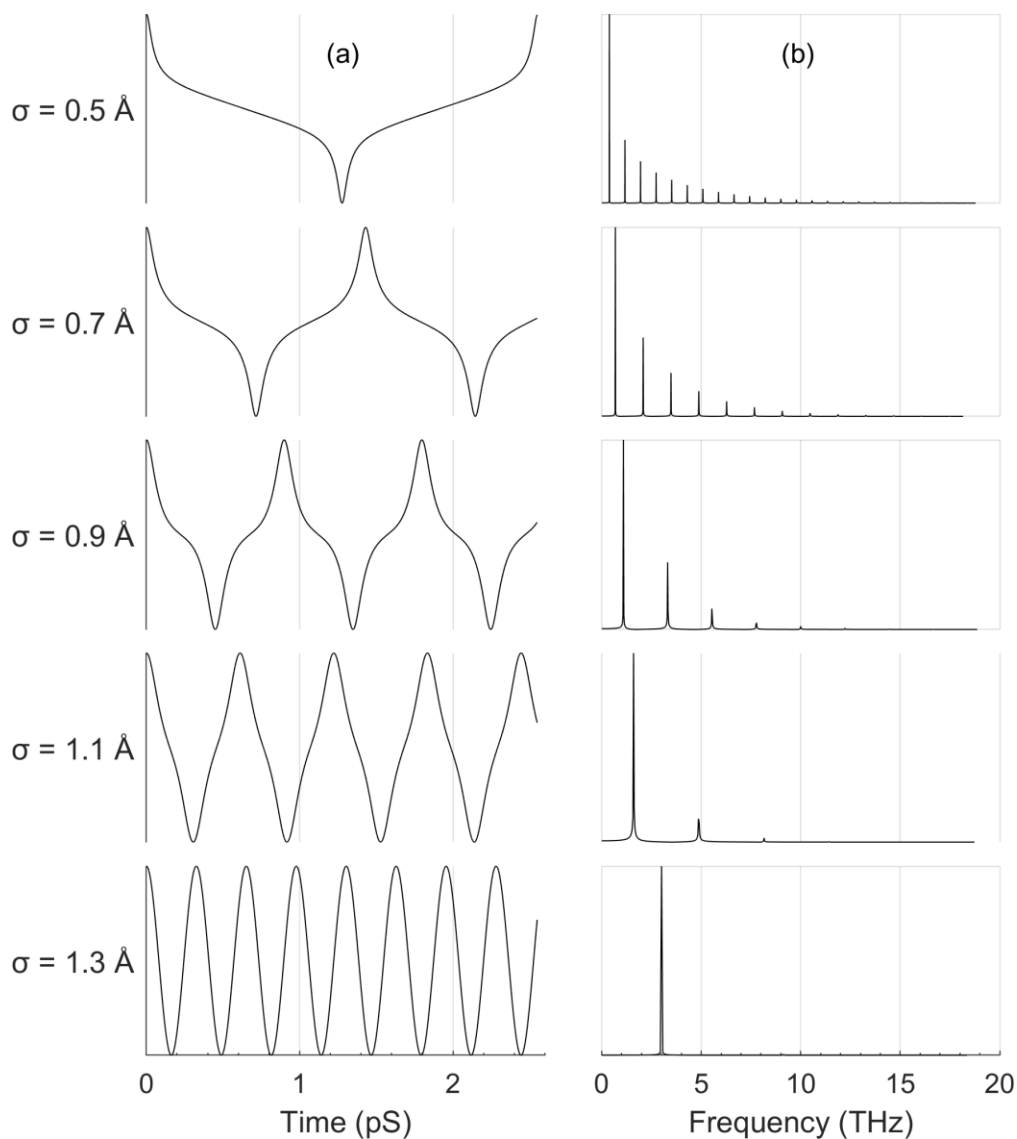
Figure 2-8 (a) Velocity auto-correlation functions for the solute species as a function of its size in the frictionless one-dimensional simulation, and (b) the corresponding vibrational spectra. Discrete peaks result from the periodic nature of the solute motion and the lack of friction.

The vibrational spectra shown on the right side of **Figure 2-8** are obtained via Fourier

transformation of the VACFs on the left. The first notable feature is that the spectra all consist of

sets of discrete, equally spaced delta functions. Secondly, the number of peaks present in each

spectrum decreases with increasing value of σ, i.e., the number of peaks decreases with

decreasing anharmonicity of the composite potential. Upon further inspection, it is apparent that

all peaks are odd integer multiples of the lowest frequency peak in each spectrum, and as a result

the spacing between subsequent peaks increases with the value of the lowest frequency peak.

The lowest frequency peak corresponds to the particle's period of oscillation within the

composite potential. All of this makes sense given that the vibrational frequency spectrum

recontextualizes motion in terms of harmonic modes. This is explicit in the formulation of the

Fourier transform. Therefore, to reconstruct periodic anharmonic motion depicted in the VACF

from a series of harmonic modes, the amplitude and frequency for each constituent harmonic

mode must take on specific values. It quickly becomes obvious that to maintain the periodic

nature of the motion, the frequency values of all constituent harmonic modes can only take on

values that are integer multiples of the fundamental frequency. Furthermore, because of the

mirror symmetry in particle motion relative to the center point, even multiples are excluded. The

set of discrete, regularly spaced peaks whose magnitudes decay towards increasing frequency

seen in the vibrational spectra for this one-dimensional system is a telltale signature of

anharmonicity in the system dynamics, referred to as higher harmonics.

Compared to this one-dimensional analogue, a three-dimensional molecular structure possesses

almost infinitely more degrees of freedom. The motion of any given atom is non-deterministic

because momentum is constantly exchanged through collisions with other atoms, and hence, the

trajectories of atoms are much more stochastic than that of our one-dimensional oscillator. To

approximate these perturbations, the two outer carbon atoms are made to oscillate sinusoidally with up to a 15% change in their relative positions, and a velocity damping coefficient of 0.01 is imposed on the motion of the mobile solute atom to compensate for the energy added by driving the system boundaries. The imposed harmonic oscillation of the surrounding carbon atoms modulates the topology of the potential energy surface by mimicking, in a simplified way, the constrained but constant motion of the local environment in solid state materials. The extent of this variation in potential energy surface is shown in the inset of **Figure 2-9**. The velocity damping also helps to continuously vary the solute particle's amplitude, and therefore period, of oscillation in a manner more consistent with the chaotic particle dynamics present in real materials. The VACF and vibrational spectrum for this system in **Figure 2-9** are much more in line with what one expects from a mobile phase in the solid state. Even with the system modifications described above, it is apparent that the VACF still does not completely decorrelate. This is primarily a limitation of the dimensionality of this system. In a one-dimensional system, the VACF can only take on a value of zero if one of the particle's velocities in the inner product is precisely zero. This is because there are no orthogonal spatial dimensions in which the particle can move so the particle's velocity can only be correlated or anticorrelated with itself, not uncorrelated. For our purpose here, which is to develop a qualitative understanding of the effect that dynamic variation of the potential shape and vibrational amplitude has on the spectrum, this does not pose an issue. It is apparent from the vibrational spectrum in **Figure 2-9**, that what had previously been a spectrum of equally spaced delta functions when the shape of the potential energy surface and the vibrational amplitude was constant has become a continuous distribution of frequencies analogous to those of our three-dimensional many-particle simulations.
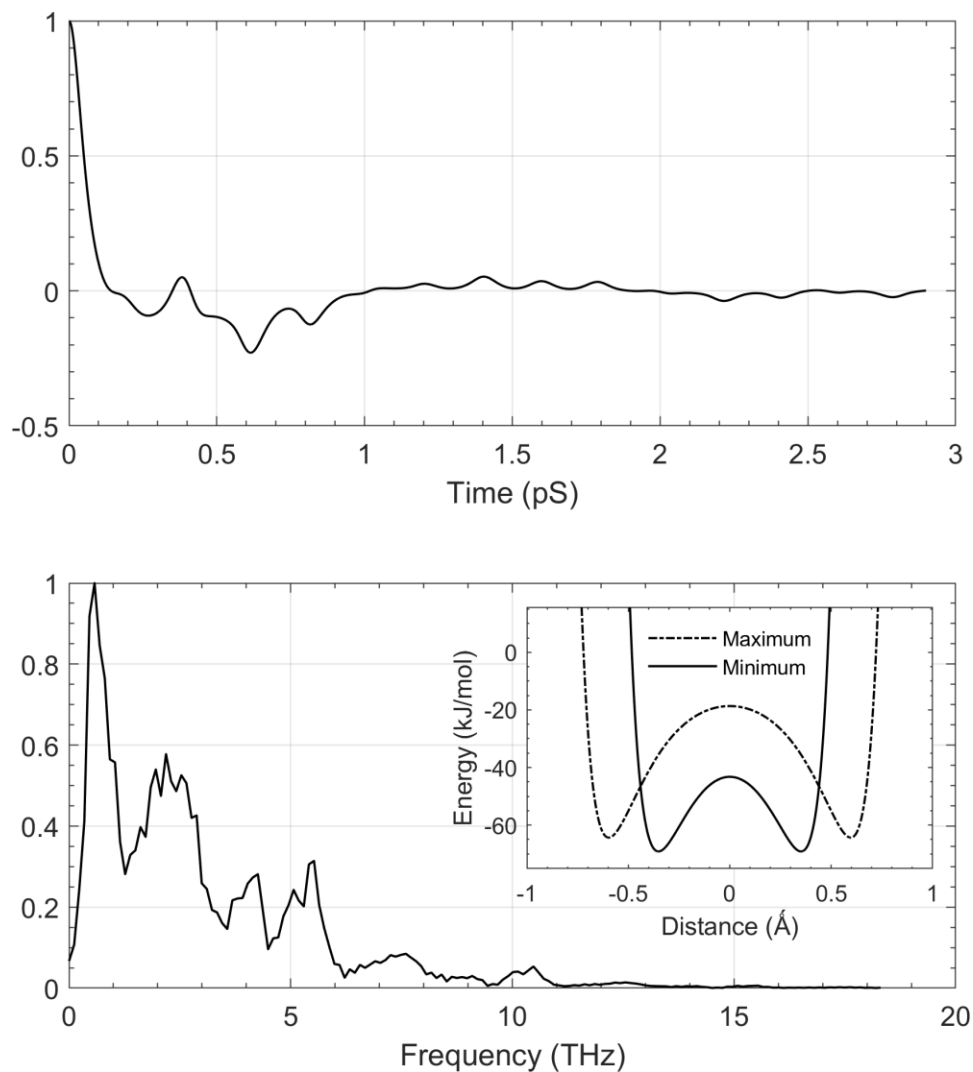
Figure 2-9 Velocity auto-correlation function (top) and vibrational spectrum (bottom) for the solute particle in the one-dimensional analog system with applied velocity damping. Inset: Extent of potential energy surface modulation due to a sinusoidal oscillation by network atoms.

Based on these observations, we submit that many of the higher frequencies present in the spectra for the three-dimensional simulations correspond to higher harmonic modes of a lower fundamental frequency representative of a specific oscillatory amplitude and local potential energy surface state. This is also consistent with the notion that oscillatory particle motion that is more harmonic in nature, produces spectral peaks that appear more symmetric while more anharmonic oscillatory motion produces asymmetric spectral peaks with tails towards high frequencies.

Another aspect that may be inferred from the behavior of the one-dimension model to that of our more complex three-dimensional system is that, as apparent in **Figure 2-7**, for sufficiently small particle sizes local potential minima are deep and located too far apart for particles to travel between without being imparted with large kinetic energies, resulting in low diffusivity. Conversely, for sufficiently large particles would-be local potential minima are located so close together that they actually merge, confining the particle and resulting in a jammed system that also exhibits low diffusivity. It is only for a specific range of intermediate particle size that the local potential minima are both shallow enough and close enough that particles can move between adjacent potential minima with relative ease resulting in high diffusivity. In fact, the adjacent minima merge (the composite possesses no negative curvature) between the values of σ equals 1.2 and 1.3 Å in the one-dimensional system. This corresponds to the minimum in the pressure vs. ϕ_S curve ($\phi_S \sim 0.214$ or $\sigma \sim 1.24$ Å) for the three-dimensional system; the location pertaining to the onset of instability.

2.3.4 Cohesive Rupture as the Reason for the Onset of Diffusion

Now, we revisit the pressure vs. ϕ_S curves for the energy-minimized configurations both starting solute atoms at sublattice positions and random positions. Since we have an analytical expression for the internal pressure relationship to atomic packing fraction in the form of the Anton-Schmidt equation of state, taking the derivative with respect to the atomic packing fraction for both systems at an arbitrary value of ϕ_S, yields a measure akin to the bulk modulus, $K(\phi_S)$. The inverse of this quantity corresponds to the compressibility, $\beta(\phi_S)$. However, it is important to keep in mind that these measures do not describe the system as a whole; instead, they single out the system's mechanical response to changes in the solute-network interactions. Important for the following discussion, the compressibility exhibits negative values in certain regions of ϕ_S.

Generally, a negative compressibility is physically not meaningful, as it implies an increase in volume as a result of applying a compressive stress, and they are therefore associated with regions of instability (e.g., the two-phase region predicted by the van der Waals equation of state). In the present context, we attribute negative compressibility to instabilities in the cohesive quality of the solute species inside the network interstices. The pressure and compressibility curves are overlaid in **Figure 2-10** as a function of atomic packing fraction.
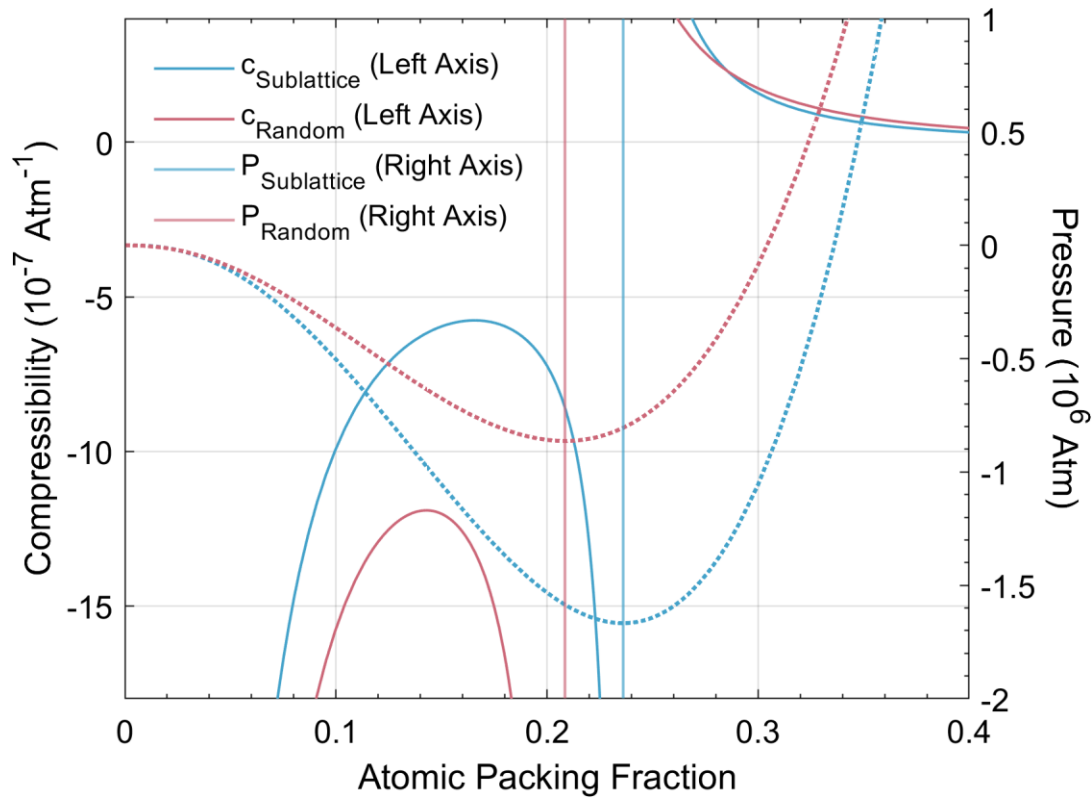
Figure 2-10 System compressibility as a function of atomic packing fraction (solids lines, left axis) for the solute at lattice positions (blue) and at energy-minimized positions reached from a random initial configuration (red) overlaid with corresponding internal pressure curves (dotted lines, right axis).

Moving from high to low packing fraction, the minimum in the pressure curve represents the transition to instability at which point cohesive rupture begins to occur. Specifically, this rupture pertains to solute-network bonds such that the solute atoms snap toward one side of their local network cavity resulting in local density fluctuations in the system. The transition to instability becomes more obvious when looking at the compressibility curves since the compressibility

diverges at the pressure minimum. Meanwhile, the inflection points in the pressure curves represent the location within this unstable region where the system transitions to the high-diffusivity regime. Consequently, the mobility transition occurs at the maximum in the compressibility vs. ϕ_S curve. Diffusivity is maximized towards lower ϕ_S values with respect to this compressibility maximum. Accordingly, the solute mobility is highest when (1) the compressibility is negative, i.e., its contribution to cohesion in the structure deteriorates, and (2) when local density fluctuations in ϕ_S, for as long as they create more space for the solute, further destabilize the configuration (compressibility becomes more negative with decreasing atomic packing fraction). In other words, not only does decreasing the packing fraction result in lower internal tensile stress because it is easier for solutes to leave their local potential energy minima in the centers of the interstices, but that past the mobility transition this effect is self-catalyzed because the energy landscape changes in such a way that the solutes attain the mobility to do so more easily. Similarly, the trends that can be observed in **Figure 2-5** corroborate the above arguments: the inflection point in the log diffusivity vs. ϕ_S relationship coincides with that in the pressure vs. ϕ_S relationship, and thus with the maximum in the compressibility vs. ϕ_S curve. The vibrational spectrum for the value of ϕ_S nearest the inflection point, $\phi_S = 0.149$, in **Figure 2-6**, is the one with the single asymmetric peak, whose high-frequency wing is evocative of closely stacked higher harmonics from a range of fundamental modes. As mentioned previously, diffusion can only occur in a system with an anharmonic potential. Our analysis suggests the onset of diffusion occurs at a packing fraction where the vibrational spectrum of the system shows the strongest evidence for anharmonicity, i.e., $\phi_S = 0.149$, which also coincides with the inflection point in the pressure as a function of ϕ_S. Solute particles in the system at this packing fraction appear to possess large vibrational amplitudes, greatly exploring their local potential

61

energy wells and spending significant time in highly anharmonic, negatively curved regions of the potential energy surface. As the packing fraction is decreased further, these dynamics cease, and their corresponding signature in the vibrational spectra are no longer present. This shift in dynamics is due to the cohesive rupture of the system as solute atoms break bonds with some of their neighboring carbon atoms and are pulled toward one side of their local network cavity, captured more closely by their remaining carbon neighbors, constituting a dramatic evolution of the potential energy landscape.

2.4 Conclusions

To better understand atomic transport mechanisms, we studied this phenomenon in a simple model system consisting of a covalently bonded species that forms a continuous three-dimensional network and mobile species that occupies and moves about the interstices of this network. This approach reduces the structural complexity from that of actual materials that are being considered as potential solid electrolytes, with the expectation to expose the essential attributes of atomic mobility. We observe that the solute diffusivity decreases linearly with the site occupancy fraction, likely due to solute-solute collisions. By systematically varying the size of the mobile solute particles, while keeping that of carbon in the supporting structure constant, different diffusive regimes have been identified. At large solute sizes, the diffusivity of this species is limited by the comparably large energy barriers corresponding to narrow apertures in the network it must cross to move from one interstice to the next. Similarly, the diffusivity of very small solutes is diminished, because the energetics of this species has transitioned from cohesive to adhesive, which is associated with large activation barriers for the solute to overcome to even migrate within an interstice. The interesting behavior in terms of the solute mobility is observed in between these two extremes. The thermodynamic quantity best

associated with this transition is the internal pressure of the system. Descending from high to low solute packing fractions, the internal pressure decreases from positive values, where each solute particle overfills its interstice, to negative values, where solutes experience a net tensile pull from the carbons. The internal tensile limit is crossed at the pressure minimum, $\phi_S = 0.236$, below which solute detaches at least from some of the supporting network elements. For as long as the curvature in the internal pressure vs. packing fraction is positive, fluctuations in the solute sub-system density would tend to reconstitute the cohesive state. Below the inflection point, $\phi_S < 0.149$, the solute sub-system would tend towards separation, i.e., it has entered the adhesive regime.

In this context, we found that solute diffusivity starts to rise at $\phi_S = 0.149$, coinciding with the inflection point in the pressure vs. packing fraction. The vibrational spectrum for the configuration at $\phi_S = 0.149$ is different from the spectra at other packing fractions in that it possesses a single broad continuous peak with a tail towards high frequency. Further analysis reveals that the features of this spectrum are indicative of the motion of particles exploring locations on the potential energy surface characterized by highly anharmonic particle dynamics. However, the maximum solute diffusivity occurs at $\phi_S = 0.104$. Note that below the minimum in the pressure curve, $\phi_S < 0.236$, the compressibility of the system is negative, which signifies that the configurations of solute species inside the network interstices are unstable, i.e., cohesive rupture begins to occur. Here, rupture means breaking of some solute-network bonds such that the solute atoms snap toward one side of their local network cavity. The onset of solute diffusion occurs well within instability region and coincides with the maximum in the compressibility vs. ϕ_S curve. Furthermore, the solute mobility peaks when (1) the compressibility is negative, i.e., as the free volume available to the solute increases (corresponding to a shrinking solute size) the

pressure in the system increases (corresponding to a reduction in tensile stress due to decohesion between solute and network elements), and (2) decohesion is self-catalyzed because the compressibility becomes more negative with decreasing atomic packing fraction, i.e., the increase in free volume is accompanied by decreasing changes in the tensile stress due to distance-related reduction in solute-network interactions. However, further reduction in solute packing fraction causes particle mobility to rapidly plunge, because the solute adheres to the facet of network interstice. Hence, the optimal condition for high solute mobility is a potential energy surface characterized by extensive anharmonicity and strong but not complete solute-network decohesion.

2.5 References

1. Tersoff, J. Empirical interatomic potential for carbon, with applications to amorphous carbon. *Phys. Rev. Lett.* **61**, 2879–2882 (1988).

2. Hansen, J. P. Phase transition of the Lennard-Jones system. II. High-temperature limit. *Phys. Rev. A* **2**, (1970).

3. Thompson, A. P. *et al.* LAMMPS - a flexible simulation tool for particle-based materials modeling at the atomic, meso, and continuum scales. *Comput. Phys. Commun.* **271**, (2022).

4. Polak, E. & Ribiere, G. Note sur la convergence de méthodes de directions conjuguées. *Rev. française d'informatique Rech. opérationnelle. Série rouge* **3**, (1969).

5. Parrinello, M. & Rahman, A. Polymorphic transitions in single crystals: A new molecular dynamics method. *J. Appl. Phys.* **52**, (1981).

6. Shinoda, W., Shiga, M. & Mikami, M. Rapid estimation of elastic constants by molecular dynamics simulation under constant stress. *Phys. Rev. B - Condens. Matter Mater. Phys.* **69**, (2004).

7. Martyna, G. J., Tobias, D. J. & Klein, M. L. Constant pressure molecular dynamics algorithms. *J. Chem. Phys.* **101**, (1994).

8. Tuckerman, M. E., Alejandre, J., López-Rendón, R., Jochim, A. L. & Martyna, G. J. A Liouville-operator derived measure-preserving integrator for molecular dynamics simulations in the isothermal-isobaric ensemble. *J. Phys. A. Math. Gen.* **39**, (2006).

9. Nash, S. G. A survey of truncated-Newton methods. *J. Comput. Appl. Math.* **124**, (2000).

10. Anton, H. & Schmidt, P. C. Theoretical investigations of the elastic constants in Laves phases. *Intermetallics* **5**, 449–465 (1997).

11. Mayer, B. *et al.* Ab-initio calculation of the elastic constants and thermal expansion coefficients of Laves phases. *Intermetallics* **11**, (2003).

12. Grüneisen, E. Theorie des festen Zustandes einatomiger Elemente. *Ann. Phys.* **344**, 257–306 (1912).

13. Vočadlo, N. L. & Price, G. D. The Grüneisen parameter - computer calculations via lattice dynamics. *Phys. Earth Planet. Inter.* **82**, 261–270 (1994).

14. Proserpio, D. M., Hoffmann, R. & Preuss, P. Possible Hard Materials Based on Interpenetrating Diamond-like Networks. *J. Am. Chem. Soc.* **116**, (1994).

15. Tang, J. *et al.* Activation volume dominated diffusivity of Ni50Al50 melt under extreme conditions. *Comput. Mater. Sci.* **171**, (2020).

16.   Dove, M. T. Introduction to lattice dynamics. *Introd. to lattice Dyn.* (1993) doi:10.1119/1.17708.

17.   Park, G. *et al.* Quantitative Measurement of Li-Ion Concentration and Diffusivity in Solid-State Electrolyte. *ACS Appl. Energy Mater.* **4**, (2021).

Chapter 3 Equivalent Ionic Mobility Enhancements in a Model Sodium Silicate Glass from Ion-Exchange and Isotropic Straining

Abstract

We have computationally explored the use of ion-exchange to enhance ionic mobility in a model sodium silicate glass using molecular dynamics simulation. The glass is formed from the melt as cesium silicate before replacing the larger cesium ions with sodium. This results in 4.5 to 6-fold increases in sodium ion diffusivity for glass at temperatures between 400K and 600K when compared to a standard melt-quenched sodium silicate glass. The increase in sodium mobility appears to result from the increased volume of the ion-exchanged glasses that does not relax out, at least on molecular dynamics timescales, so long as the material is below its glass transition temperature. To remove the variable of volume relaxation and directly investigate the effect of increasing volume on sodium ion diffusion, we also explore the dynamics of a melt-quenched sodium silicate glass at 600K subject to variable isotropic volumetric strains. Volumetric strains up to approximately 0.25 result in increased sodium mobility of the same magnitude as ion-exchange. Strains greater than this cause the diffusivity of sodium to decline due to the initiation and escalation of the silica network rupture. The increases in sodium mobility are caused by the weakening of ionic bonding with surrounding oxygen atoms resulting in a reduced tensile stress on the sodium, and thus, a reduced curvature and depth of their equilibrium site potential wells. Our results indicate that robust glass networks suitable for low temperature ion-exchange and stable against volume relaxation make good candidates for high ionic conductivity solid-state electrolytes.

3.1 Introduction

We investigate the efficacy of using ion-exchange as a method to improve ionic mobility in inorganic glass solid-state electrolytes (SSEs). We chose an alkali silicate glass for this case study as this relatively simple binary glass is a common component in many inorganic and composite SSEs. Specifically, we are using molecular dynamics simulations to explore exchanging a larger modifier alkali cation with which the glass was formed with a smaller alkali cation. This is essentially the inverse of the chemical strengthening process, in which a glass is formed containing smaller modifying ions which are then exchange with larger ions to produce a compressive stress at the surface of the glass which increases the stress the glass can undergo before failure occurs.[1–3] Electrolyte ion-exchange experiments on various classes of SSEs in previous studies with the goal of improving ionic conductivity have yielded mixed results.[4–13] In previous studies of NASICON-type inorganic crystalline SSEs, some results have shown decreases in conductivity when replacing sodium with lithium while more recent results have indicated the opposite.[5,14] The difference in these results appears to be related to the method of ion-exchange utilized. The ion-exchange using molten salt requires higher temperatures, which may enable greater structural relaxation after ion-exchange. Furthermore, this method accomplishes lower ion-exchange ratios in the range of about 50% replacement, which causes suppression of ionic mobility due to the mixed-alkali effect. The study producing enhanced ionic conductivity used a liquid organic solvent carrier containing dissolved bis(trifluoromethane) sulfonimide lithium (LiTSFI) to carry out the exchange with effectively total sodium replacement at a lower temperature that largely restrains structural changes. In a study involving ion-exchange within a metal-organic framework (MOF) of tetrabutylammonium cations with lithium, increased ionic conductivity was demonstrated. These investigators used a similar

method of low-temperature solvent-mediated ion-exchange preserving the MOF structure and producing a high exchange ratio.[13] Ion-exchange methods to increase conductivity in inorganic glass electrolytes have been studied as well primarily for aluminum, zirconium, phosphate, and/or titanium containing modified silicate glasses in which sodium is generally replaced with lithium or silver cations.[4,6–12] The results for these studies were mixed. Ion-exchange to incorporate smaller cations can produce enhanced ionic mobility so long as the ion-exchange procedure is able to be performed below the glass transition temperature (T_g) of the material. It has been reported that when ion-exchange is carried out below T_g, there is no suppression resulting from the mixed-alkali effect even when the exchange is not carried out completely. The mobility reduction when the glass contains a mixture of alkali cations appears to result from network structural developments that can only occur when the material has been exposed to the required thermal energy (temperatures above T_g). In these studies the authors were replacing potassium with sodium to create soda-lime silica and replacing sodium with lithium to make lithium aluminosilicate.[7,15] However, the presence of mixed mobile ion-based conductivity reduction has been reported in an aluminosilicate glass where sodium was replaced with silver even when the process was carried out well below T_g.[11] It has been suggested that reduced ionic conductivity is caused by an induced low temperature relaxation not only at sites containing silver ions but at sites still occupied by sodium as well. There is a decrease of the oxygen coordination number for sodium and increase surrounding silver, which forms a covalent bond with nonbridging oxygen atoms in these systems.[16]

In a previous work, we explored the effect of varying the size of a mobile solute species on its diffusivity within a crystalline diamond lattice.[17] This simple two-component solid-state material was simulated using molecular dynamics (MD) methods. The carbon atoms of the diamond

lattice were covalently bound to one another, and the solute atoms existed in the interstices, interacting with the carbon network via a Lennard-Jones potential. The size of the solute species was varied systematically while the volume of the system was held constant. A relationship between the internal pressure of the system, its vibrational properties, and the diffusivity of the solute species was evident. Orders of magnitude increase in solute mobility was found to relate to structural instabilities that were reflected in the calculated solute-specific internal pressure, solute-specific compressibility, and features of the vibrational spectra.

Following these findings and the body of literature suggesting ionic mobility can be enhanced through ion-exchange, in the present work, we use atomistic simulations to investigate atomic transport in a more realistic sodium silicate glass. Specifically, we explore the effect of large to small alkali ion-exchange in a silicate glass before homing in on the essence of enhanced mobility inducing structural effects in ion-exchanged, as opposed to melt-quench, glasses by analyzing ion mobility within isotropically strained glasses.

3.2 Methodology

To investigate the influence of exchanging the cationic species on the ionic conductivity in an inorganic amorphous solid electrolyte, we explore alkali silicate glasses via MD simulation. The silicate glasses were composed of 20 mol% alkali oxide where the cation is either sodium or cesium. Simulations are performed using the Large-scale Atomic/Molecular Massively Parallel Simulator (LAMMPS) maintained by Sandia National Lab.[18] The potential chosen to govern intermolecular interactions is ReaxFF due it its ability simulate chemical reactions and dynamic bonding with a good balance between fidelity and computational expense. ReaxFF dynamically calculates bond orders based on interatomic distances. This enables the modulation of bond, angular, and torsional energies as a function of local environment, which allows for simulation of

70

chemical reactions. [19–23] The electronegativity equalization method (EEM) is used to simulate charge transfer when calculating Coulomb interactions.[24] ReaxFF has been shown capable of simulating and quenching high temperature sodium silicate melts to the glassy state and producing reasonable structural features that are in general agreement with experimental data.[25,26] The force field parameterization used in the following was developed by merging extensively tested force fields originally used by Psofogiannakis et al. for the purpose of simulating hydration of copper containing high-silica zeolites.[27]

The following alkali silicate simulations contain 4080 atoms and are initialized with sodium or cesium, silicon, and oxygen atoms in random positions within the supercell with period boundary conditions. The initial volumes of these simulations were chosen to correspond approximately to experimental room temperature densities of 20 mol% sodium or cesium silicate glasses, i.e., about 3.0 and 2.38 g/cm^3, respectively. A conjugate-gradient energy minimization is performed to avoid atomic core overlaps producing a more stable configuration for subsequent finite temperature time integration. Boltzmann distributed velocities are assigned to all atoms corresponding to a temperature of 4000 K. This high temperature is chosen to facilitate an increased rate of exploration of configuration space. The simulations are run in the NVT ensemble at 4000K for 125 ps, 125 ps at 3000K, and another 125 ps at 2500K before quenching. Quenching occurrs at a rate of 0.8 K/ps from 2500K to 1500K in the NPT ensemble with an applied external pressure of 1000 atm to ensure that a condensed phase is maintained. At 1500K, the alkali silicates are relaxed for 500 ps while the external pressure is slowly reduced to 0 atm before further quenching to 300K at a rate of 0.8K/pS. At each temperature where diffusion data is collected, the alkali silicate is allowed to relax for another 500 ps before a subsequent 100 ps production run. A time step of 0.5 femtoseconds is used for time integration of the equations of

motion in all simulations. Larger timesteps used with the ReaxFF potential can result in instability due to the incorporation of the electronegativity equalization method and dynamic bonding.

For solid-state electrolyte applications, we are primarily interested in the transport properties of the alkali cationic species. The most common method for characterizing atomic mobility in MD simulations is the calculation of diffusion coefficients. This calculation generally utilizes the mean squared displacement (MSD) of the particles of interest over the course of a simulation. The ensemble-averaged MSD of particles collected over time yields the diffusivity based the equation,

$$D = \lim_{t \to \infty} \frac{\langle |\vec{r}(t) - \vec{r}(0)|^2 \rangle}{2d \cdot t}, \tag{3.1}$$

where $r(0)$ is the initial particle position, $r(t)$ is the particle position at subsequent times t, and d is the dimensionality of the system. For adequately sampled atomic trajectories, the MSD typically exhibits a ballistic regime at short times when the particle is "caged" within its local network cavity and a diffusive regime at times when correlation between atomic motion deteriorates due to "cage-breaking" events that result in aperiodic trajectories. The diffusivity is obtained from the slope of the MSD vs. time within the diffusive regime. Though the system possesses periodic boundary conditions, for this calculation, particle coordinates are "unwrapped" such that the simulation box length is not subtracted when the particles pass through a periodic boundary and reenter from the opposite side of the simulation box and position data is stored every ten femtoseconds for the duration of the production run.

3.3 Ion-Exchange Simulations

Atomic diffusivity data is collected for the sodium and cesium cations within the alkali silicates at 300K, 400K, 500K, 600K, and 1000K. The alkali diffusivities within the sodium silicate and

cesium silicate glasses quenched from the molten state are used for comparison with the ion-exchanged glass, which is generated from the melt as a cesium silicate glass, but the cesium atoms are subsequently replaced with sodium atoms at the low temperatures of interest. The ion-exchange method utilized for these simulations represents a perfect exchange efficiency where transport limitations are not an issue. This is because in molecular simulations, one can simply replace one species of atoms with another. In this case, cesium is replaced by sodium simply by changing the mass and characteristic parameters of the interaction potential. After the ions are exchanged, the simulated glasses are relaxed for 500 ps before the 100 ps production run for data collection.

The resultant diffusivities are plotted versus inverse temperature for the sodium, cesium, and ion-exchanged sodium ions in the silicate glasses in **Figure 3-1**. As hypothesized, the ion-exchanged sodium ions possess higher diffusivities than the sodium ions in the melt-quenched glass, and both are more diffusive than the larger and much more massive cesium ions. The diffusivity for the alkali ions is Arrhenius in character with respect to changes in temperature for the temperature range between 400K and 600K or for values of 1/T in the range between about 1.5 and 2.5K^{-1}. For the simulations at 300K (1/T = 3.33K^{-1}), cationic diffusion becomes a rare event on simulation timescales resulting in a breakdown in the validity of Equation 1. For the simulations at 1000K (1/T = 1K^{-1}), the alkali cations diffuse readily, but the diffusivity values do not align with the Arrhenius relationship present at lower temperatures. This is because the glass-forming silicates are above T_g for these simulations, where the supercooled liquid undergoes significant structural rearrangements that are part of the glass transition process.
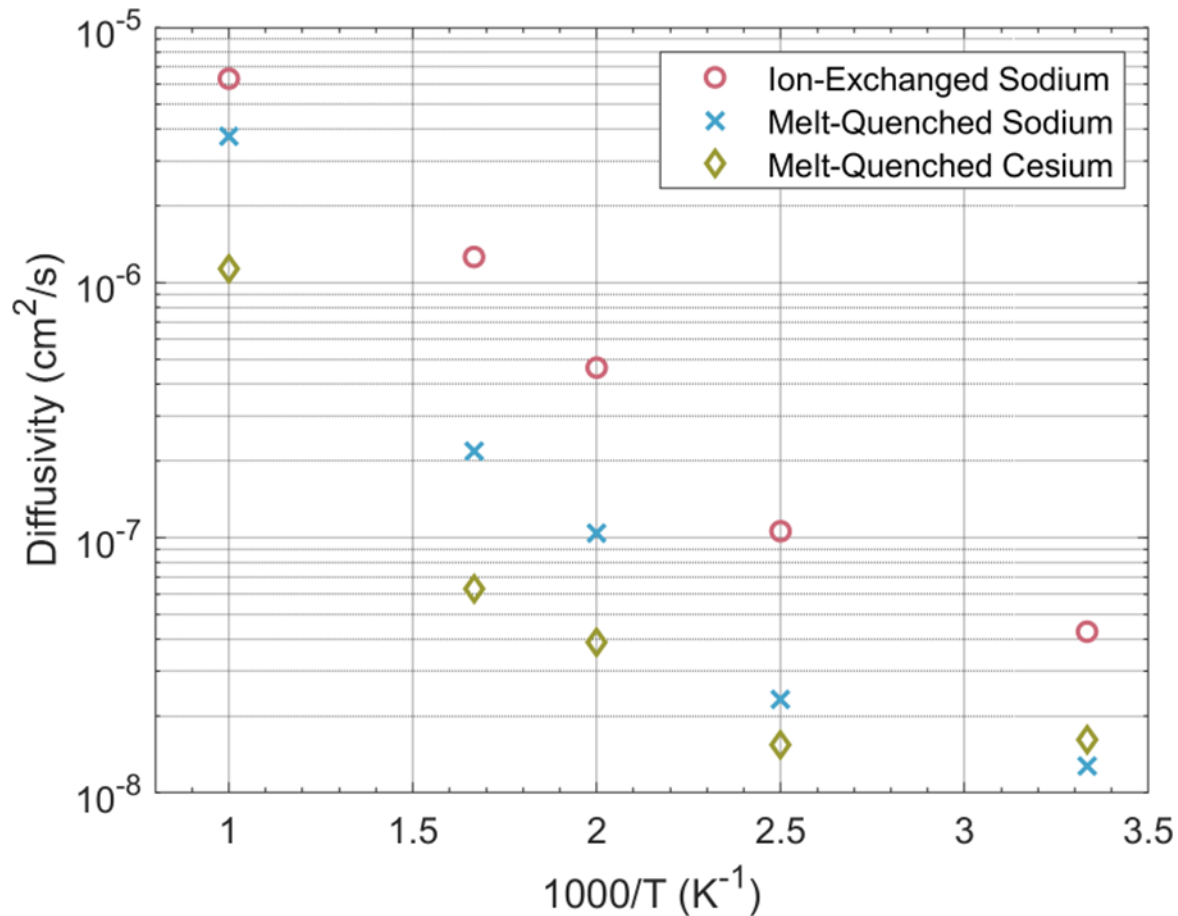
Figure 3-1 Ion diffusivities as a function of inverse temperature for the ion-exchanged sodium silicate (circles), melt-quenched sodium silicate (Xs), and melt-quenched cesium silicate (diamonds) glasses.

Exchanging the cesium ions with sodium causes a contraction of the network and an increase in the number density of the ion-exchanged glasses. This happens because the sodium ions are smaller, possessing a higher charge density, than the replaced cesium ions. This results in an initial tensile force on the surrounding network that upon relaxation causes the observed contraction in volume. Importantly, this volume contraction still resulted in densities that are about 13% to 15% lower than that of the sodium silicate specimens produced from the melt, with the exception of the 1000K ion-exchanged glass (above T_g) for which the density was only an 8.6% contraction after 2 nanoseconds and the structure continued to relax. For the other ion-exchanged sodium silicate glasses, the diffusivity of the sodium ions within the Arrhenius

temperature range is increased by about 4.5 to 6-fold over that of the sodium silicate quenched from the melt.

As noted, there is always some degree of relaxation that occurs following the ion exchange. Relaxing out the initial tension from replacing the cesium atoms with sodium is simple enough on MD timescales and is largely complete after approximately 10 ps. However, beyond this period of relatively rapid contraction, further relaxation that occurs at a much slower rate is evident subsequently over a period of nanoseconds for the ion-exchanged simulation at 1000K. While lower temperature simulations do not appear to further relax, at least not on the timescale of nanoseconds, whether significant relaxation would occur for these systems on experimental timescales of seconds and hours, unattainable in simulations, is not obvious. The difference in sodium ion diffusivity between the ion-exchanged and from-melt sodium silicate glass appears to result primarily from the increased free volume in the ion-exchanged glass. The extent of structural relaxation of the network that occurs after ion-exchange may result from our particular choice of binary glass-former. In this simple sodium silicate glass, the modifying cation is an important structural element that aids in supporting the network from collapse. The degree of relaxation after ion-exchange may be reduced with this use of a more structurally robust but complicated glass composition containing multiple network formers, some of which, like boron, are capable of incorporating alkali oxides with reduced network depolymerization by forming partially charged bridging oxygens. To remove the added variable of relaxation after ion-exchange and directly probe the effect of increasing free volume, we next investigate how sodium ion mobility is affected by applying an isotropic volumetric strain to a quenched sodium silicate glass.

3.4 Isotropic Expansion Simulations

In the following, we report on the effect of increased free volume on ion mobility, where a 20 mol% sodium silicate glass is strained isotropically resulting in a uniform volume expansion. This is analogous to our previous work involving variation of solute size within a constant volume diamond lattice, but in the simulations described here all atomic interactions remain unchanged and instead the volume of the glass network itself is varied.[17] Effectively, this means that all atomic 'sizes' are fixed but the bonds between them are strained. The LAMMPS "fix deform" method is used to accomplish this. The "deform" method allows for the volume and/or shape of the simulation box to be changed during a molecular dynamics run. For the present simulations, the shape of the simulation box is conserved but the three orthogonal dimensions of the simulation box are expanded identically at each timestep in a manner analogous to applying a constant rate of strain. Each strain simulation is initialized from the 20 mol% sodium silicate glass at 600K in the canonical ensemble. The glass is strained over 10 ps to its new volume and then maintained at that volume for a 500 ps relaxation before a 100 ps production run during which data is collected. Volume strains between –0.2 and 1.0 are simulated in increments of 0.05. This corresponds to uniaxial strains between about -0.07 and 0.26. The negative strains correspond to compression, which are included for comparison.

Before discussing the effect on cation diffusivity, let us inspect the effect of the applied volumetric strains on the potential energies and internal pressures of the sodium silicate glass. This provides insight into the cohesive energy of the structure and the tensile or compressive forces within the network. **Figure 3-2** shows the potential energy of the sodium silicate as a function of the applied strain. A near-parabolic energy-volume relationship, similar to those often reported from first-principles structure calculations, is apparent in the immediate vicinity of

the unstrained glass between strains of about –0.2 to 0.2.[28] However, for strains larger than 0.25, the harmonic energy-volume relationship breaks down as strains become large enough to begin breaking network bonds, resulting in significant changes to the structure of the network.
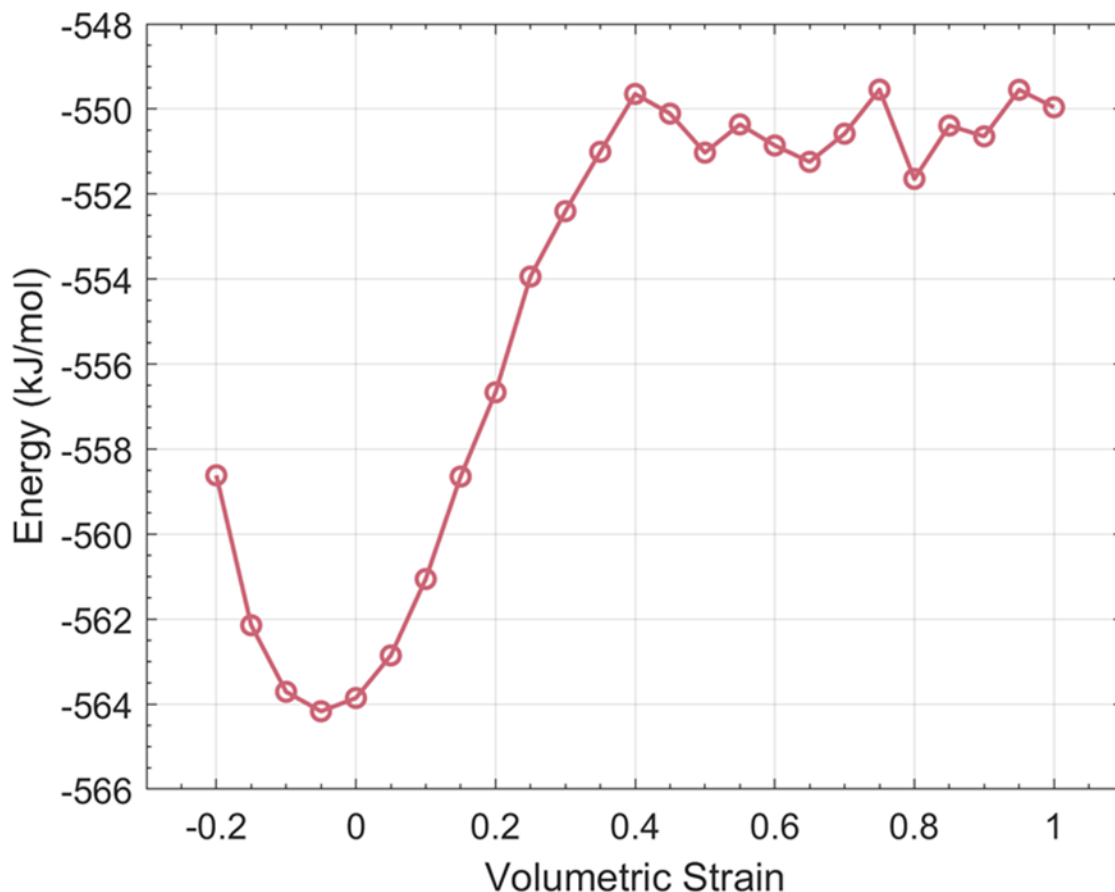
Figure 3-2 The potential energy as a function of isotropic volume strain for a simulated sodium silicate glass.

The relationship between internal pressure and strain in **Figure 3-3** supports this. As one would expect, negative strain, or compression, results in an increase in internal pressure and positive strains cause tension that results in negative internal pressures. However, strains greater than 0.25 while still resulting in negative internal pressures, lead to decreasing magnitudes with increasing strain. Once again, this is due to the onset of network bond breaking at a strain of 0.25 and gradual destruction of the network with increasing strains. The shape of the pressure-strain relationship here is similar to that of our previously studied two-component model system.[17]
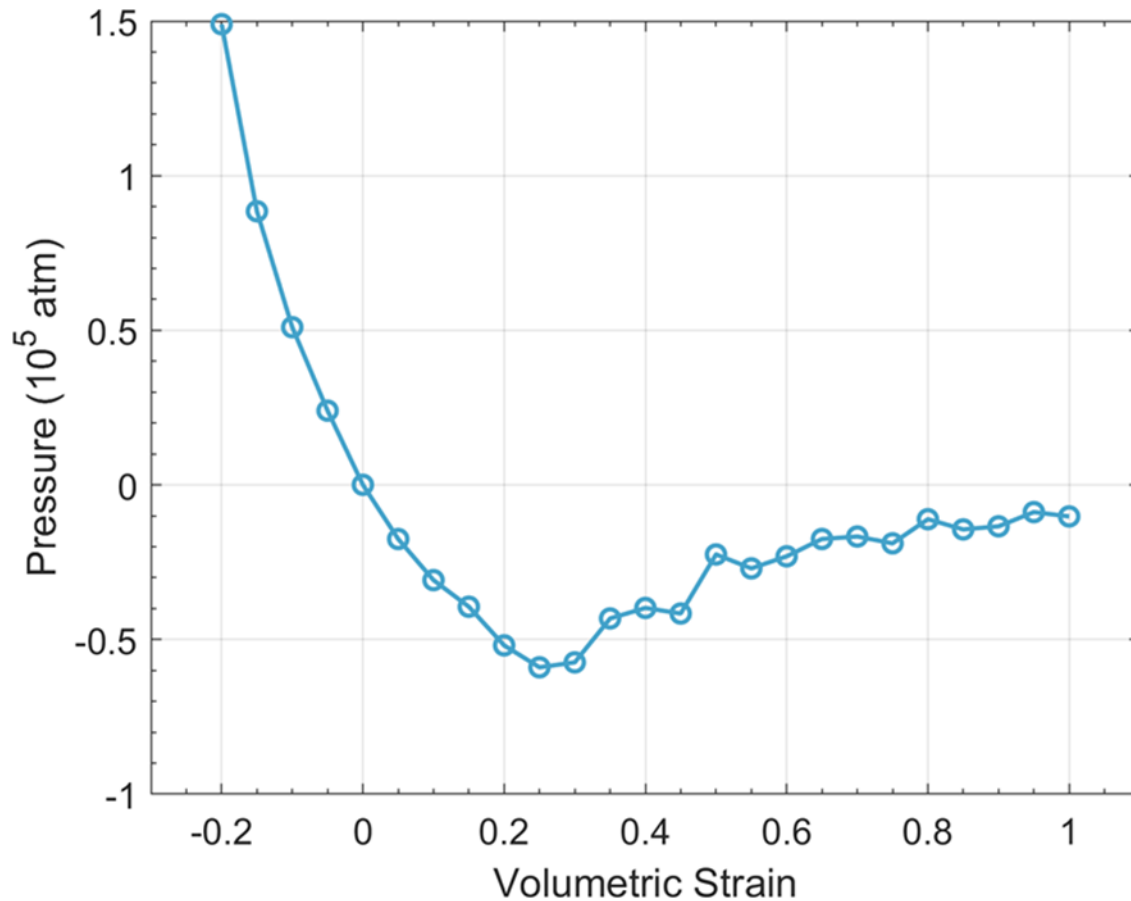
Figure 3-3 The internal pressure as a function of isotropic volume strain for a simulated sodium silicate glass.

However, past the pressure minimum, where increasing strain results in increasing pressure the curve is much more irregular and jagged than our prior results. This observed difference is due to network slippage, i.e., when the most strained bond at any given moment breaks it allows for a larger cavity in the structure to open and in its surroundings the stress momentarily relaxes out. Meanwhile another bond in the network becomes the weakest link until it too breaks, giving rise to local relaxation, and so forth. This repeated straining and breaking of covalent network bonds is different from our previous study, where the only bond energies affecting is relationship are solute-network bonds of Lennard-Jones type and the covalent network bonds remain unaffected. These solute-network Lennard-Jones bonds are more analogous to the ionic bonding of the sodium atoms with the network in the present system. However, the energy of ionic bonds

decreases to a much lesser extent with increasing distance than that of the network bonds, which largely obscures their contribution to the pressure-strain relationship in **Figure 3-3**.

Now, we turn our attention to the effect of volumetric strain on the sodium cation diffusivity. This relationship is shown in **Figure 3-4** for the sodium silicate glass at 600K for all strains simulated. As one may expect, the compressed glasses possess lower sodium ion diffusion than the unstrained glass, decreasing by a little over an order of magnitude with a volumetric strain of –0.2. As for the expanded glasses, they demonstrate an increase in sodium ion mobility.
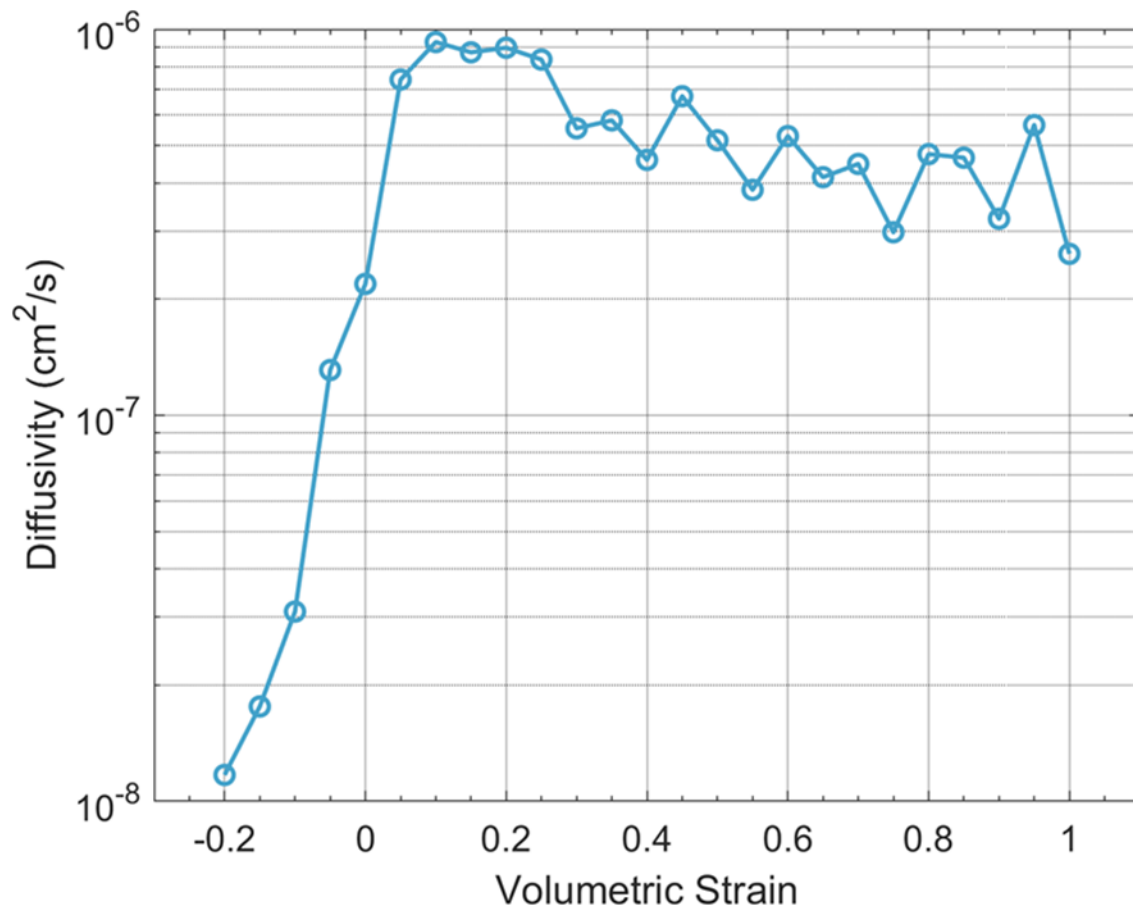
Figure 3-4 The sodium ion diffusivity (logarithmic scale) as a function of isotropic volume strain for a simulated sodium silicate glass.

From 0 to about 0.1 strain, there is a 4.25-fold increase in diffusivity. The diffusivity plateaus at a maximum between strain values of 0.1 and 0.25 before decreasing in a seemingly linear but noisy fashion with increasing strain. There is an interesting correspondence between the potential

energy (**Figure 3-2**), internal pressure (**Figure 3-3**), and diffusivity (**Figure 3-4**) as strain is

varied. For small strains, there is a decreasing amount of energy stored in the form of potential

energy, the internal pressure decreases (tension), and the sodium ion diffusivity increases.

However, at a strain value of 0.25 the potential energy ceases to follow the parabolic relationship

as a function of volume, the internal pressure, though still negative, shifts from decreasing with

strain to increasing with strain, and the diffusivity-strain relationship similarly inverts from

increasing to decreasing with increasing strains. This behavior suggests that so long as the

network structure through which the sodium ion travels remains intact, there is a direct and

positive relationship between volumetric strain and diffusivity due to, at least in part, the internal

tension that weakens the bond energies. This weakening of bond energies results in a lower

energy requirement for sodium ions when hopping between sites within the network. Once again,

we see similarities here with our previously studied two-component lattice-solute model

system.[17] Increasing volumetric strain, analogous to decreasing solute particle size, initially

results in substantial increases in solute or modifier cation mobility. However, while the prior

model system shows a dramatic drop off in mobility when the solute becomes small enough to

get trapped against the network wall, the sodium ion in the silicate glass discussed here becomes

less diffusive as strains are increased past the tensile limit of the network but not dramatically so.

The reason for this is that sodium never becomes trapped and instead can still diffuse within the

progressively ruptured network, but as the network breaks down to greater extents, the sodium

ions become more limited in terms of directions in which they can diffuse due to a growing

number of cavities in the network fabric that are too large to allow for diffusive ion hopping.

To further analyze the observed behavior, we focus on the distribution of forces felt by each

constituent species within the strained glasses. This is accomplished by collecting the per-atom

pressures over the course of 1 ps using the "compute stress/atom" command in LAMMPS.[29] This method is based on calculating the symmetric six component per-atom stress tensor where here we are only interested in the virial contribution to the normal stresses. This includes the bonding, pairwise, multibody, and long-range Coulomb interactions. The atomic stresses are calculated as a product of stress and volume since atomic volumes are not well defined. These values can be divided by the per-atom volume that we take here to be the quotient of the cell volume and number of atoms as a crude approximation. This has no effect on the relative stresses during comparison. Finally, we convert the three per-atom normal stresses to a pressure through the summation of their negative magnitudes and division by the number of components, in this case three. This is analogous to the calculation of a hydrostatic pressure, but negative magnitudes are used here to reconcile the difference in sign convention between atomic stresses and system pressures in MD simulations. The distribution of per-atom pressures for sodium, silicon, and oxygen are shown in **Figure 3-5** for strains of –0.1, 0, 0.2, and 0.75. This gives an indication of species specific per-atom pressures in the cases of compression, no strain, strain with an intact network, and strain past the onset of network rupture. For all species, the pressure distributions narrow with increasing strain values. This can be understood in terms of the geometric constraints covalent atomic bonds are subject to at different densities. Under tension these bonds stretch without much flexibility in terms of their spatial orientation, whereas under compression the corresponding strain can be accommodated not only by shortening the bonds, but the structure can buckle at pivotal joints, giving rise to a larger variation in the angles between adjoining bonds. Hence, in a compacted structure there exists a greater number of local force transmission motifs resulting in a broader spread in the per-atom pressure. Though distributions

for all species span both positive and negative pressure values, the mean and majority values of the sodium and silicon distributions are negative while oxygen shows the opposite trend.
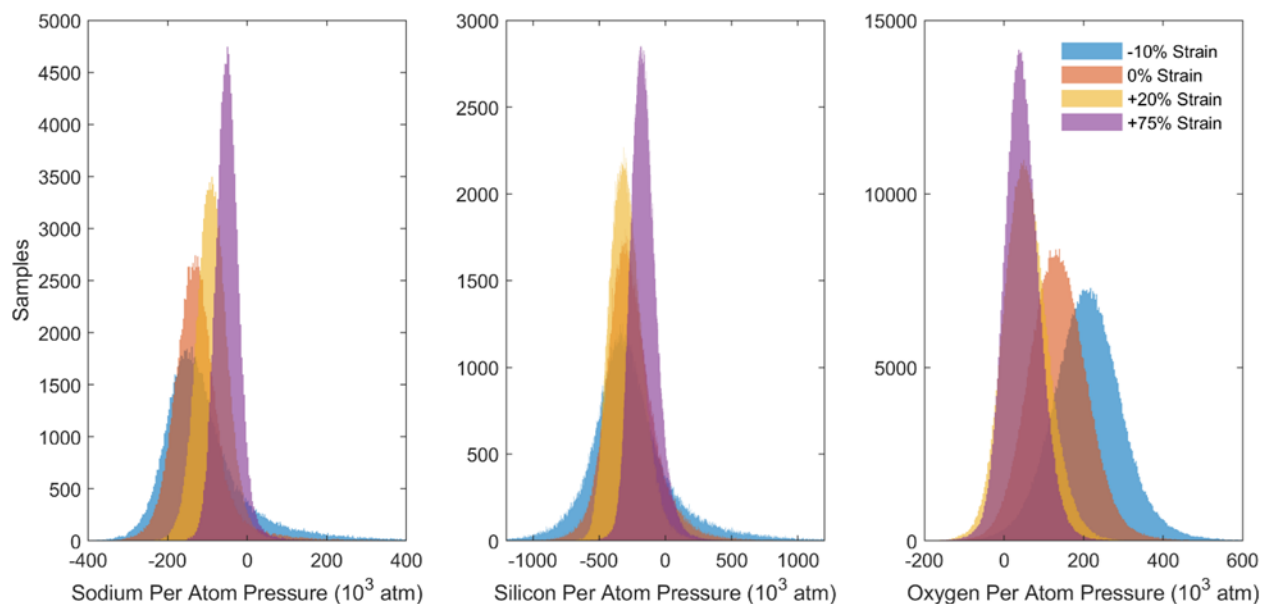
Figure 3-5 Distributions of sodium, silicon, and oxygen per-atom pressures for volumetric strains of -0.10, 0.0, 0.20, and 0.75. Samples refer to the number of atoms with a similar per-atom stress across 1ps.

This means the sodium and silicon atoms are primarily under tension while the oxygen atoms are primarily under compressive stress. This would suggest that, within the structural environment of these sodium silicate glasses, the oxygen-oxygen repulsion is an important factor in supporting the structure from collapsing into a denser configuration while the sodium and silicon atoms maintain structural cohesion by stabilizing against expansion. Turning our attention to the effect of strain on the per-atom pressures of each species, sodium possesses the simplest relationship where it appears that increasing strain continuously reduces the magnitude of negative pressure on the sodium atoms. In the case of silicon, there are only minor reductions in the negative pressure magnitudes until some network bonds have broken, as is the case for 0.75 strain. Interestingly, the oxygen atoms only show reductions in pressure for strain values corresponding to stretched network bonds prior to the initiation of bond breaking at 0.25.

Using these per-atom pressure values, we were able to reconstruct the internal pressure-strain curve from **Figure 3-3** on a species-specific per-atom basis by averaging the per-atom pressures for each species at a given strain. These species-specific pressure curves are shown in **Figure 3-6**. The sodium pressure curve exhibits a minimum, corresponding to the largest-magnitude negative pressure, at zero strain. The magnitude of pressure on sodium atoms decreases under both volume compression and expansion. Importantly, however, the reduction in tensile stress on sodium as a result of volume compression is caused by increased Coulombic repulsion with the adjacent silicon atoms now in closer proximity. The reduction in tensile stress on sodium when the glass is volumetrically expanded results from weakened ionic bonding with surrounding oxygen atoms that facilitates sodium ion hopping due to the decreased energy required to escape potential wells in the potential energy surface. This region of the sodium pressure curve between the minimum at 0 strain and the inflection point at about 0.25 strain coincides with the region of strains characterized by enhanced diffusivity in **Figure 3-4**. This sodium pressure-strain curve more closely aligns with previous results from our lattice-solute model system as changes in the internal pressure for that system results solely from interaction between the network and mobile solute species.[17] Minor differences in the features of the two pressure relationships arise from the differences in the bonding types of the mobile species, i.e., Lennard-Jones versus ionic. Unlike the Lennard-Jones potential, which tends to act over the distance of a few angstroms, ionic bonding resulting from Coulombic interactions are long-range in nature and the forces generated decrease proportional to the square of the interatomic distance.
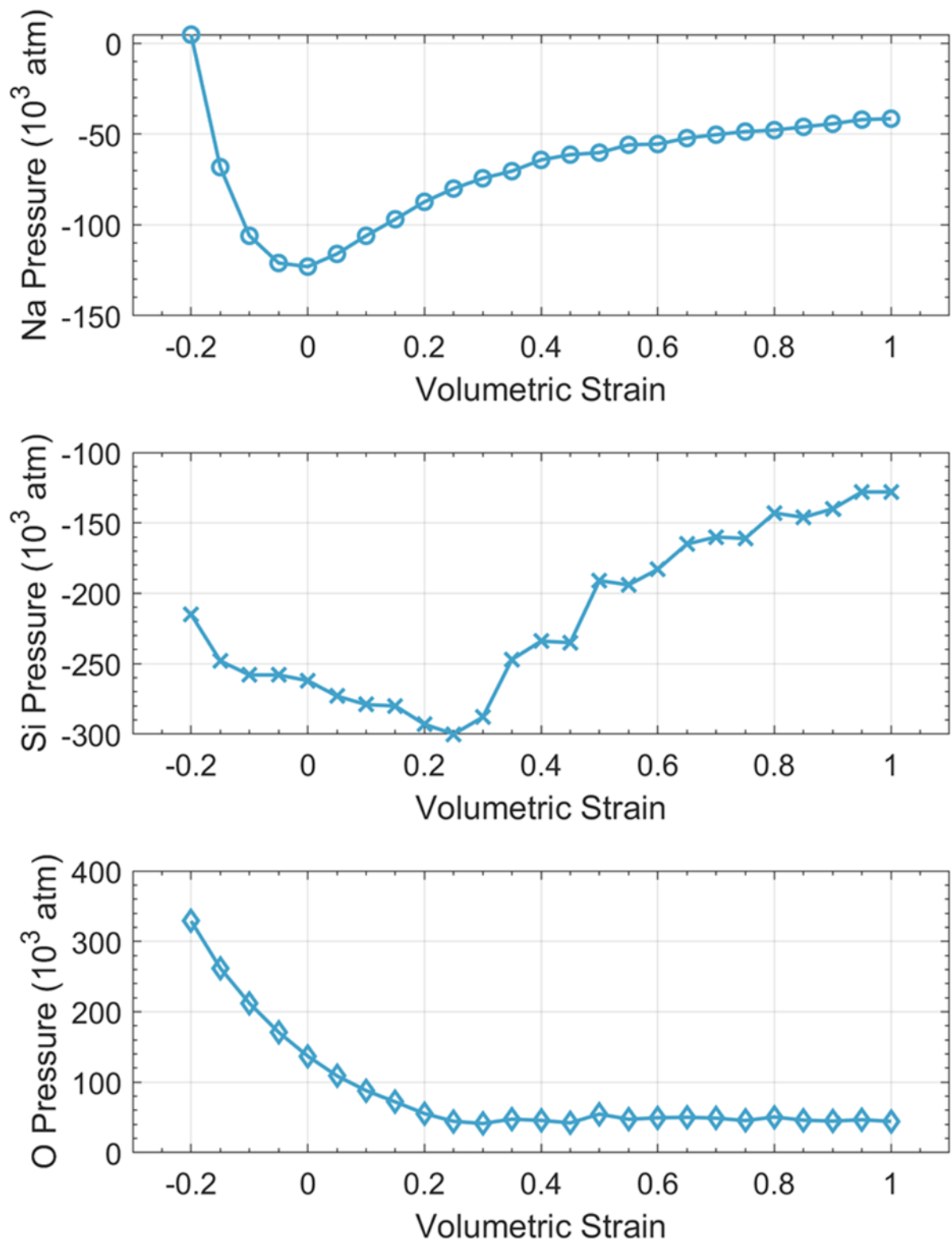
Figure 3-6 Species-specific per-atom pressure as a function of isotropic volume strain for sodium (circles), silicon (Xs), and oxygen (diamonds).

This is the reason for the less abrupt reduction is tensile stress on sodium atoms when the glass is subjected to large strains compared to the trends observed in our previous work. For the present sodium silicate glass, at strains greater than 0.25, the tensile stress continues to decrease and the jump distances between stable sodium sites on average increases. Furthermore, network bonds have begun to break, creating cavities in the network structure that create gaps large enough to prohibit diffusion. The breakdown of the network is more apparent when inspecting the silicon pressure curve, which exhibits its largest negative magnitude at 0.25 strain, the tensile limit of the network. For smaller strains than this, the tensile stress on silicon increases with increased volumetric strain. However, for larger strains, the tensile stress decreases in a jagged fashion with increasing volumetric strain. The jagged character of this decrease is because the polar covalent bonding of the network constituents is short range in nature, unlike the ionic bonding of the sodium ions. The jagged decrease in pressure magnitude represents the cycle of network bond stretching, breaking, remaining bonds relaxing, then stretching, and breaking within increasing strain. Contrary to the cases of sodium and silicon, the oxygen per-atom pressure curve shows a decrease in the pressure magnitude with increasing strain as the oxygen-oxygen repulsion decreases and the silicon-oxygen bonds are stretched. Then, once the network bonds begin to break, the per-atom oxygen pressure remains relatively constant upon further strain. This occurs because the network no longer expands continuously in an isotropic fashion and does not allow nearby oxygen atoms to spread further apart since the tearing of the network allows the separated fragments to relax to higher local densities. Essentially, the oxygen atoms that share bonds with the same silicon atom and adjacent silicon atoms maintain a roughly constant distance from one another.

3.5 Conclusions

To investigate the efficacy of increasing the local volume available to diffusing sodium ions on their mobility within a solid-state electrolyte, we first simulate the ion-exchange of cesium with sodium in a melt-quench formed cesium silicate glass using the ReaxFF reactive potential in LAMMPS to perform the molecular dynamics simulations. We compare these results to those obtained for simulated melt-quenched sodium silicate and cesium silicate glasses. The ion-exchanged sodium silicate exhibits 4.5 to 6 times higher sodium cation diffusivities than the melt-quenched sodium silicate glass, so long as the ion exchange is performed on samples below their glass transition temperature. The increases in sodium ion mobility appear to be associated with an increase in free volume within the ion-exchange glasses. The ion-exchanged sodium silicate glasses below T_g are 13% to 15% less dense than their melt-quenched counterparts at the same temperature. The expanded volumes associated with these ion-exchanged glasses may be retained to a greater extent with this use of a more complex glass composition containing multiple network formers some of which, like boron, can incorporate alkali oxides with a lower than commensurate degree of network depolymerization due the formation of four-coordinated boron. Glasses of this type may be more resistant to structural changes initiated by exchanging differently sized ions. To remove the effect of relaxation after ion-exchange as a variable and directly probe the effect of increasing free volume on ion mobility, we also explore the effect of applying of an isotropic volumetric strain to a melt-quenched sodium silicate glass on sodium ion mobility. We compare the sodium ion diffusivities, system potential energies, and system internal pressures as a function of volumetric strain at 600K. The sodium ion mobility increases significantly with increasing volumetric strain for strains between 0 and 0.25. Upon exceeding these strains, diffusivities begin to decrease with increasing strain. As revealed by the trends in

the potential energy as a function of strain, this reversal in the cation diffusivity occurs because the network bonds begin to break, no longer increasing volume uniformly within the structure and instead creating cavities in the structure that inhibit diffusion. The calculated per-atom species-specific pressures or stresses as a function of strain reveal whether components are under compression or tension and how this changes with volumetric straining of the glass. Oxygen atoms tend to be under compressive stress while sodium and silicon tend to be under tension. There is a reduction in tensile stress on sodium when the glass is volumetrically strained. This results from weakened ionic bonding with surrounding oxygen atoms and facilitates sodium ion hopping due to the decreased energy required to escape their potential wells. This region of the sodium per-atom pressure curve between the minimum at 0 strain and the inflection point at about 0.25 strain coincides with the strains characterizing the enhanced diffusivity region in **Figure 3-4**. Ion-exchange of a large ionic species with a similarly charged smaller species results in enhanced ionic conduction so long as the structure is able to resist densification. The mechanism of mobility enhancement for an ion-exchanged glass is similar to that of a volumetrically strained glass in that the tensile stress on sodium ions is reduced and undulations in the potential energy surface are attenuated. Our findings suggest that low temperature ion-exchange, replacing a large modifier cation with a smaller one, is a viable strategy for improving ionic conductivity in solid-state electrolytes based on robust inorganic glasses that are stable against volume relaxation.

3.6 References

1.   Gy, R. Ion exchange for glass strengthening. *Materials Science and Engineering B: Solid-State Materials for Advanced Technology* vol. 149 (2008).

2.   Karlsson, S., Jonson, B. & Stålhandske, C. The technology of chemical glass strengthening - A review. *Glass Technology: European Journal of Glass Science and Technology Part A* vol. 51 (2010).

3.   Tandia, A., Vargheese, K. D. & Mauro, J. C. Elasticity of ion stuffing in chemically strengthened glass. *J. Non. Cryst. Solids* **358**, (2012).

4.   Thakkar, R. & Chudasama, U. Ionic conductance of Lithium Exchanged Phases in Amorphous and Crystalline Zirconium Titanium Phosphate. *Acta Chim. Slov.* **57**, 250–256 (2010).

5.   Mouahid, F. E. *et al.* Na-Li exchange of Na1+xTi2-xAlx(PO4)(3) (0.6 <= x <= 0.9) NASICON series: a Rietveld and impedance study. *J. Mater. Chem.* **11**, 3258–3263 (2001).

6.   Tomandl, G. & Schaeffer, H. A. Relation between the mixed alkali effect and the electrical conductivity of ion-exchanged glasses. *Phys. Non-Crystalline Solids* 480–485 (1977).

7.   Dubiela, M., Rolingb, B. & Füting, M. Ac conductivity and ion transport in K+-for-Na+ ion-exchanged glasses: exchange experiments below and above the glass transition temperature. *J. Non. Cryst. Solids* **331**, 11–19 (2003).

8.   Braunger, M. L., Escanhoela, C. A. & Ziemath, E. C. Electrical conductivity of Ag–Na ion exchanged soda-lime glass. *Solid State Ionics* (2014).

9.   Funabiki, F. Electrical conductivity of Ag+/Na+ ion-exchanged titanosilicate glasses. *Solid State Ionics* **160**, 281–288 (2003).

10.   Tsujimura, T. Li-ion conductive phosphosilicate glass ceramics synthesized by ion exchange. *Solid State Ionics* **262**, 829–832 (2014).

11.   Yano, T., Nagano, T., Lee, J., Shibata, S. & Yamane, M. Ionic conduction and dielectric relaxation in Ag+/Na+ ion-exchanged aluminosilicate glasses: mixed mobile ion effect and KWW relaxation. *Solid State Ionics* **150**, 281–290 (2002).

12.   Tsujimura, T., Koike, A. & Kuroki, Y. Li-Ion Conductive Phosphate Glass Synthesized by Using Ion Exchange. *ECS Trans.* **45**, 135–141 (2012).

13.   Xu, W. *et al.* A Metal-Organic Framework of Organic Vertices and Polyoxometalate Linkers as a Solid-State Electrolyte. *J. Am. Chem. Soc.* **141**, (2019).

14.   Zhu, L. *et al.* Enhancing ionic conductivity in solid electrolyte by relocating diffusion ions

to under-coordination sites. *Sci. Adv.* **8**, (2022).

15. Ingram, M. D., Davidson, J. E., Coats, A. M., Kamitsos, E. I. & Kapoutsis, J. A. Origins of anomalous mixed-alkali effects in ion-exchanged glasses. *Glas. Sci. Technol. Glas. Berichte* **73**, (2000).

16. Dubiel, M., Brunsch, S., Kolb, U., Gutwerk, D. & Bertagnolli, H. Experimental studies investigating the structure of soda-lime glasses after silver-sodium ion exchange. *J. Non. Cryst. Solids* **220**, (1997).

17. Beg, C. & Kieffer, J. Anharmonicity and the emergence of diffusive behavior in a lattice-solute model solid-state electrolyte. *Comput. Mater. Sci.* **228**, 112359 (2023).

18. Thompson, A. P. *et al.* LAMMPS - a flexible simulation tool for particle-based materials modeling at the atomic, meso, and continuum scales. *Comput. Phys. Commun.* **271**, (2022).

19. Chenoweth, K., Van Duin, A. C. T. & Goddard, W. A. ReaxFF reactive force field for molecular dynamics simulations of hydrocarbon oxidation. *J. Phys. Chem. A* (2008) doi:10.1021/jp709896w.

20. Van Duin, A. C. T., Dasgupta, S., Lorant, F. & Goddard, W. A. ReaxFF: A reactive force field for hydrocarbons. *J. Phys. Chem. A* (2001) doi:10.1021/jp004368u.

21. Senftle, T. P. *et al.* The ReaxFF reactive force-field: Development, applications and future directions. *npj Computational Materials* (2016) doi:10.1038/npjcompumats.2015.11.

22. Aktulga, H. M., Fogarty, J. C., Pandit, S. A. & Grama, A. Y. Parallel reactive molecular dynamics: Numerical methods and algorithmic techniques. *Parallel Comput.* (2012) doi:10.1016/j.parco.2011.08.005.

23. Liu, L., Liu, Y., Zybin, S. V., Sun, H. & Goddard, W. A. ReaxFF-lg: Correction of the ReaxFF reactive force field for London dispersion, with applications to the equations of state for energetic materials. *J. Phys. Chem. A* **115**, (2011).

24. Mortier, W. J., Ghosh, S. K. & Shankar, S. Electronegativity Equalization Method for the Calculation of Atomic Charges in Molecules. *J. Am. Chem. Soc.* **108**, (1986).

25. Deng, L. *et al.* Structural features of sodium silicate glasses from reactive force field-based molecular dynamics simulations. *J. Am. Ceram. Soc.* (2020) doi:10.1111/jace.16837.

26. Yu, Y., Wang, B., Wang, M., Sant, G. & Bauchy, M. Reactive Molecular Dynamics Simulations of Sodium Silicate Glasses — Toward an Improved Understanding of the Structure. *Int. J. Appl. Glas. Sci.* (2017) doi:10.1111/ijag.12248.

27. Psofogiannakis, G. M., McCleerey, J. F., Jaramillo, E. & Van Duin, A. C. T. ReaxFF reactive molecular dynamics simulation of the hydration of Cu-SSZ-13 zeolite and the

formation of Cu dimers. *J. Phys. Chem. C* **119**, (2015).

28.   Narejo, G. & Perger, W. F. First-principles computation of second-order elastic constants and equations of state for tetragonal BaTiO3. *Chem. Phys. Lett.* **493**, (2010).

29.   Thompson, A. P., Plimpton, S. J. & Mattson, W. General formulation of pressure and stress tensor for arbitrary many-body interaction potentials under periodic boundary conditions. *J. Chem. Phys.* **131**, (2009).

Chapter 4 Enhanced Viscoelastic Model: Reconciliation of Viscosity Measures Differing in Frequency by Ten Orders of Magnitude

Original Publications Information

The work in this chapter was published in the Journal of Non-Crystalline Solids as:

Abstract

We conduct a comparative analysis of the mechanical response of a moderately fragile sodium borate melt, juxtaposing the adiabatic complex modulus measured at GHz frequencies using Brillouin light scattering and the steady-state shear viscosity measured at zero Hz. The two data sets are perfectly compatible with one another by fitting both components of the high-frequency complex modulus using a modified Maxwell-Wiechert model, transforming the loss modulus to viscosity, and extrapolating to zero frequency. This procedure yields an excellent fit to the steady-state viscosity under the condition that the static and relaxational moduli, as well as the activation energy for viscous dissipation are temperature dependent, as modulated by the logistic function, which accounts for the structural changes in the material as it transitions from liquid to glass. Accordingly, fragility of a glass forming liquid can be regarded as a measure to the rate of change with temperature in the energy landscape topography.

4.1 Introduction

The viscosity of glass forming liquids has been of foremost interest to the researcher investigating the fundamental scientific phenomenology underlying the emergence of the amorphous state of matter, and equally, to the practitioner of glass manufacture. Viscosity, and its change with temperature, has been recognized as the key factor that determines whether a liquid subject to rapid cooling crystallizes or forms a glass. Furthermore, creating glass objects with complex shapes to tight dimensional specifications requires precise control of the viscosity during the operation. Unsurprisingly, the nature of viscosity has been a subject of persistent investigation throughout the century of modern glass science.[1–13] Both from a practical and fundamental point of view, the focus of attention is the manner in which viscosity deviates from the Arrhenius law.[14] In the mid-1980s, Austen Angell famously coined the concept of strong vs. fragile behavior to categorize the temperature dependence of the viscosity for glass forming systems,[15–19] and with this he created a standard allowing researchers to gauge, label, and interpret their findings.

As a materials characteristic, viscous dissipation is understood to be the consequence of processes that are manifest at the atomic or molecular level. Phenomenologically, the viscosity coefficient describes the rate of momentum transport in response to an imposed strain rate, and as such, transition state theory (TST) provides a formalism based on statistical thermodynamics to quantify the underlying elementary mechanisms. This entails evaluating the relaxation rate, which involves the probability density for the system to overcome the activation energy barrier that allows one of the mechanistic entities to advance from one equilibrium configuration to another in response to the imposed constraint. Among other components, detailed below, this rate comprises the grouping $\left(Q_a / Q_g \right) e^{-E_a/k_B T}$, where Q_a and Q_g represent partition functions

associated with the activated and ground states, respectively, k_B the Boltzmann constant, and E_a the potential energy difference between these two states, or activation energy for short. The ratio Q_a/Q_g amounts to e^{S_a/k_B}, where S_a is the entropy difference between the activated and ground states. Ultimately, the amount of energy dissipated in viscous flow is inversely proportional to the relaxation rate, so that the viscosity coefficient becomes $\eta \propto e^{E_a/k_B T}$, which constitutes the dominant temperature dependent term. Hence, when graphing the logarithm of the viscosity vs. reciprocal temperature, one would expect a straight line, indicative of Arrhenius behavior,[14] which is exhibited by strong liquids in the Angell categorization.

However, in most glass forming liquids, the temperature dependence of viscosity deviates from this behavior in ways reflected by a steeper slope at low temperatures (high values of $1/T$) and a gentler slope at high temperatures (low values of $1/T$). The more the $\log_{10}\eta$ vs. T_g/T data curves away from linear behavior, the more fragile the liquid is said to be. Accordingly, various fragility indices to quantify the phenomenon, such as $m = \lim_{T \to T_g} \left(\partial \log_{10}\eta / \partial (T_g/T) \right)$, were quickly introduced. However, clarity with respect to the structural and physicochemical origin of this non-Arrhenius behavior has been slower in coming, and open questions still remain to date. Considering the above enumeration of the dominant factors controlling the relaxation rate, it is not surprising to see explanations involving the energy landscape topography becoming most generally accepted. Early investigations revealed correlations between fragility and the size of the heat capacity jump at the glass transition. While this remains a strong connection between kinetic and thermodynamic fragility,[20] the continued accruing of data suggests that this may not be comprehensive indicator across different types of materials.[21] Conversely, the rate of change of the excess configurational and vibrational entropy, as the liquid approaches its glass transition, appears to yield a more universal measure and stronger connection between kinetics and

thermodynamics.[21–25] Finally, the role of configurational entropy in characterizing fragility has also been identified among the quantities used in the topological constraint theory describing network glasses, e.g., the mean field connectivity within a coarse-grained representation of the intermediate-range order in these structures.[26, 27]

Based on these developments, the importance of the energy landscape topography for explaining the non-Arrhenius behavior of the viscosity in glass forming liquids, specifically quantification of the changes that take place in this landscape throughout the glass transition regime, is evident. Here we present an analysis that is consistent with the perspectives document in the aforementioned literature, in particular stressing the need to account for the significant changes in the energy landscape topography that occur between liquid and glass. Our analysis focuses on the anatomy of the relaxation rate, i.e., the reciprocal of the characteristic relaxation time, identifying the relevant contributions emerging from TST by juxtaposing these quantities measured at 0 Hz and ~20 GHz.
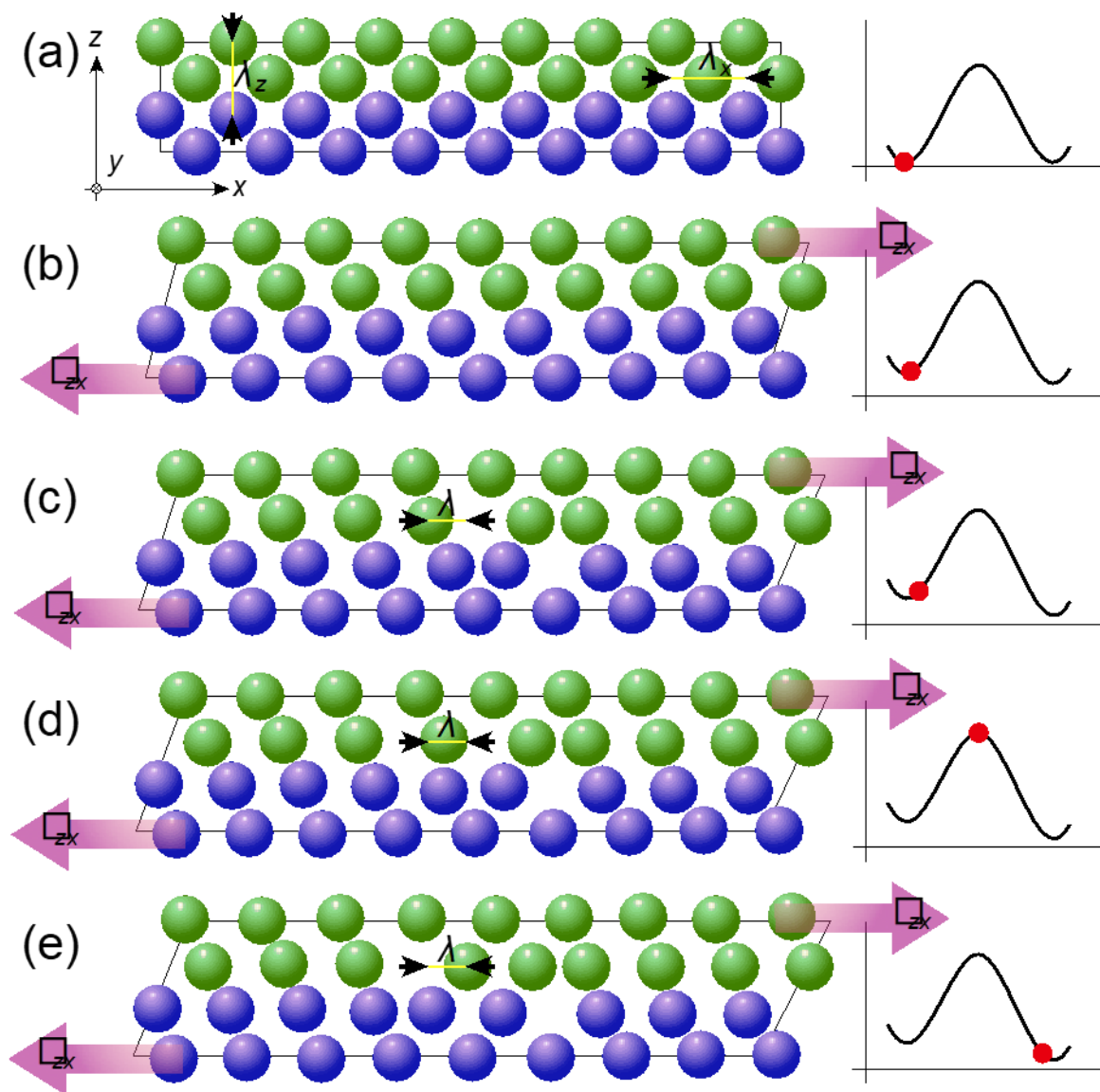
Figure 4-1 Schematic illustrating of an atomic jump event that leads to strain energy dissipation during shear flow in a liquid. Atomic positions approximate the inherent structure of the liquid for clarity. The diagrams on the right show the system potential energy associated with each configuration along the phase space coordinate aligned with the jump orientation.

4.2 Theoretical Background

4.2.1 Dissipation Mechanisms and Transition State Theory

In the 1930s, Eyring was the first to derive an expression for the viscosity coefficient based on TST.[28] According to TST, in an equilibrium liquid at a given temperature T, mobile molecular moieties, or atoms for short, jump between neighboring sites at a rate given by

95

$$k = \frac{k_B T}{h} \frac{Q_a}{Q_g} e^{-E_a/k_B T}, \tag{4.1}$$

where h is Planck's constant and the other quantities have already been defined above. We ignore Wigner's tunneling correction for now, considering that $h\nu \ll k_B T$, and we assume that the sticking coefficient is unity. Eyring then considered two adjacent layers of a liquid configuration, subject to a shear stress τ_{zx}, that acts in the positive x-direction on the top layer and in the negative x-direction on the bottom layer, as illustrated in **Figure 4-1**. Here, the normal orientation of the plane onto which the stress is applied points in the z-direction. Hence, the net force the applied stress exerts on each atom is $\tau_{zx}\lambda_x\lambda_y$, where λ_x and λ_y delineate the effective area attributed to each atom. Now, assuming that λ is the distance by which the atom is displaced during the jump event, which need not be identical to λ_x, but is of the same order of magnitude, this applied stress skews the activation barrier by the amount $\pm(\tau_{zx}\lambda_x\lambda_y\lambda)/2$, where the positive sign applies when the particle jumps opposite to the direction of the applied stress, while the negative sign reveals how the applied stress assists in the particle jump when both occur in the same direction. The net balance of this stress bias results in a preferred displacement of particles in the direction of the applied constraint, expressed by

$$k = k_+ - k_- = \frac{k_B}{h}\frac{Q_a}{Q_g}\left(e^{-\left(E_a - (1/2)\tau_{zx}\lambda_x\lambda_y\lambda\right)/k_B T} - e^{-\left(E_a + (1/2)\tau_{zx}\lambda_x\lambda_y\lambda\right)/k_B T}\right) =$$

$$\frac{k_B}{h}\frac{Q_a}{Q_g}e^{-E_a/k_B T}\sinh\left(\tau_{zx}\lambda_x\lambda_y\lambda/2k_B T\right). \tag{4.2}$$

Expanding the hyperbolic sine function as a power series and truncating after the first power, since $\tau_{zx}\lambda_x\lambda_y\lambda \ll k_B T$, yields

$$k \simeq e^{-E_a/k_B T}\frac{Q_a}{Q_g}\frac{\tau_{zx}\lambda_x\lambda_y\lambda}{h}. \tag{4.3}$$

This rate applies to every atom in a given layer and, even though the jumps of the atoms are not synchronized, over time they all jump with the same frequency. Hence, the product of jump

frequency and displacement yields the drift velocity of each atom and, consequently, of the entire layer relative to the adjacent ones. Hence, this drift velocity represents the velocity differential between two adjacent atomic planes, i.e., $\delta v = k\lambda$. Furthermore, $\delta v / \lambda_z$ represents the velocity gradient in z-direction, which appears in Newton's law for viscous flow,

$$\tau_{zx} = \eta \frac{\delta v}{\lambda_z} \Rightarrow \eta = \tau_{zx}\lambda_z/\delta v = \tau_{zx}\lambda_z/k\lambda. \tag{4.4}$$

Substituting **Equation 4.3** in **Equation 4.4** yields,

$$\eta = \tau_{zx}\lambda_z \left(\frac{Q_a}{Q_g} e^{-E_a/k_B T} \frac{\tau_{zx}\lambda_x\lambda_y\lambda^2}{h} \right)^{-1} = \frac{h\lambda_z}{\lambda_x\lambda_y\lambda^2} \frac{Q_g}{Q_a} e^{E_a/k_B T}. \tag{4.5}$$

In this expression, the various length parameters, λ_x, λ_y, λ_z, and λ are approximately of the order of the interatomic spacing, and they appear in the expression as a grouping that roughly delineates the reciprocal of the volume in which the fundamental mechanism of the atomic jump plays out. We therefore replace the grouping with a number density ρ_N. Furthermore, for an (NVT) ensemble we have

$$S/k_B = \ln(Q) + U/T, \tag{4.6}$$

where U is the system's internal energy, which allows us to replace $Q_a/Q_g = e^{S_a/k_B}$ under the condition that the process is isothermal and the total energy of the system does not change during a particle jump, which is typically the case. Note that Q_a has one degree of freedom fewer than Q_g. Also, we omit the Δ-symbol in front of both E_a and S_a for brevity and because it is needed later, but the reader should keep in mind that both of these quantities describe a difference between ground state and activated state. We finally get for the viscosity coefficient,

$$\eta = h\rho_N e^{-S_a/k_B} e^{E_a/k_B T}. \tag{4.7}$$

It is interesting to note that in Newton's law, $\sigma = \eta\dot{\varepsilon}$, which is considered a linear response law describing the momentum flux (or stress), $\sigma = (1/A) \, dp/dt$, that results from an imposed strain

rate, $\dot{\varepsilon}$, η is considered a rate coefficient, despite the fact that it has the physical dimension of a reciprocal rate. This is the consequence of the physical dimensions of the flux considered here. Moreover, as we outline in the following, it is important to not lose track of the fact that η is also a composite quantity in which the mechanistic rate coefficient appears in the denominator.

In his initial derivation of **Equation 4.5**, Eyring did not provide a detailed explanation of how elementary jumps can take place in a dense liquid. There ought to be a space to which the atom or molecule can jump. In subsequent publications, he and his coworkers address this issue and propose a mechanism by which upon collision of two molecules they form a short-lived complex and exchange positions via rotation ("… given enough space …"), before dissociating again.[29, 30] Later, when expanding his model to account for bulk viscosity, Eyring allows for the creation of 'holes' in the structure, which requires an additional amount of energy that compounds with the activation energy for motion.[31] This can be thought of as equivalent to the intrinsic vacancy formation in crystals, except that they are less palpable in amorphous structures and, as the authors show, the free space needed to effect bulk viscosity is much smaller than the size of a particle.[31] Similarly, relaxation and viscous dissipation in amorphous metals have been attributed to facilitation by point-like defects.[32, 33]

Indeed, the detailed mechanism of atomic displacements during viscous flow likely involves the temporary creation of void space in the structure. This extra space could be generated in an entirely reversible fashion, i.e., depending solely on elastic deformations and allowing for the structure to be restored after completion of the event. Hence, the necessary energy, or at least a significant fraction thereof, would not be dissipated but returned in the form of mechanical work. **Figure 4-1** shows a simplified cartoon of such a scenario. It is therefore important to analyze the

atomic-scale mechanisms underlying viscous processes in a medium using viscoelastic theory, even if this medium is well inside its liquid regime.

4.2.2 Relation to Linear Viscoelasticity

The standard approach for describing linear viscoelasticity is the Maxwell-Wiechert (MW) model,[34] which consists of a number of Maxwell elements connected in parallel, as illustrated in **Figure 4-2**. Each Maxwell element by itself contains a provision for viscous dissipation (dash pot) and elastic storage (spring) of energy. The dynamics of each Maxwell element is expressed by the differential equation

$$\frac{d\sigma_j}{dt} + \Gamma_j\sigma_j = M_j\dot{\varepsilon}, \tag{4.8}$$

where σ_j is the stress transmitted by element j, Γ_j is the relaxation rate associated with the dissipative mechanism represented by this element and M_j the associated elastic modulus. The relaxation rate can be written as

$$\Gamma_j = \Gamma_{0,j}e^{S_{a,j}/k_B}e^{-E_{a,j}/k_BT}, \tag{4.9}$$

where $\Gamma_{0,j}$ is the attempt frequency, $S_{a,j}$ the activation entropy, and $E_{a,j}$ the activation energy of the jth mechanism. Comparison with **Equation 4.7** allows us to equate $\Gamma_{0,j} = M_j/(h\rho_{N,j})$, which ascribes this factor a value ranging between $10^{13} - 10^{15}$ s^{-1}. Furthermore, we have the equalities $\Gamma_j = M_j/\eta_j = 1/\tau_j$, where τ_j is the characteristic relaxation time pertaining to this mechanism. The ratio M_j/ρ_N may be material specific but is not known *a priori*. We allow for the number density $\rho_{N,j}$ to also be mechanism specific, i.e., different mechanisms may be characterized by different spatial focus of energy.

The number of elements needed to accurately describe an observed behavior depends on the complexity of the material. For a material that dissipates energy as well as supports a static load,

i.e., from a mechanical point of view one that is considered a viscoelastic solid, the minimal model involves two elements, of which one, the leftmost one in **Figure 4-2**, possesses a zero relaxation rate. This element is purely elastic. Each remaining Maxwell element represents a different relaxation mechanism, each characterized by a particular attempt frequency and activation free energy. Conversely, a liquid does not require the purely elastic element, unless it is subject to isotropic compressive strain. Under steady state conditions, such as apply to rotating cylinder viscometry, **Equation 4.8** simplifies to Newton's law,

$$\Gamma_j \sigma_j \equiv \sigma_j \left(M_j / \eta_j \right) = M_j \dot{\varepsilon} \Rightarrow \sigma_j = \eta_j \dot{\varepsilon}, \tag{4.10}$$
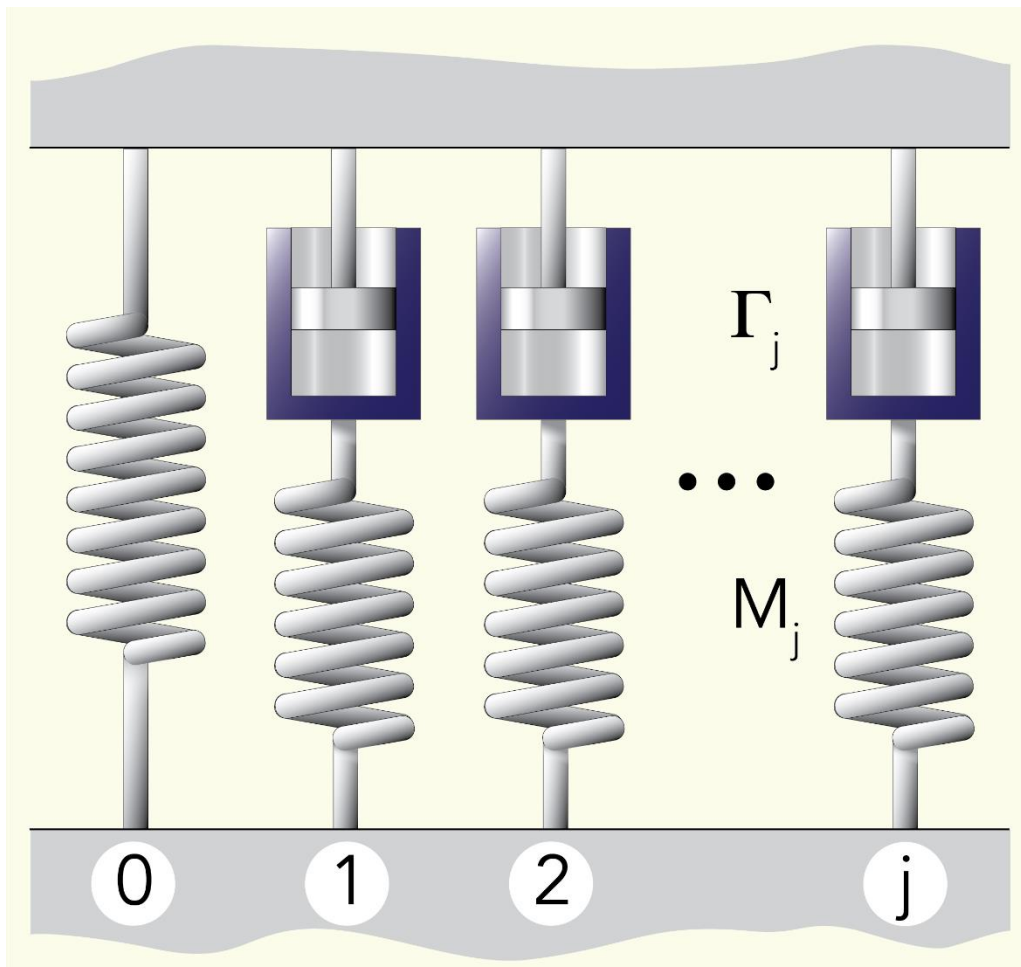
Figure 4-2 Illustration of the Maxwell-Wiechert model for linear viscoelasticity. Load is transmitted via several Maxwell elements in parallel.

which means that probing the response of a viscoelastic liquid this way does not reveal the elastic component of the process. To access the complete set of characteristic measures it is indicated to employ oscillatory probing. In this case, the solution of **Equation 4.8** yields

$$\sigma_j = \frac{\omega^2 + i\omega\Gamma_i}{\left(\omega^2 + \Gamma_j^2\right)} M_j \varepsilon \Rightarrow \frac{\sigma_j}{\varepsilon} = M_j^* = M_j' + iM_j'' = \frac{\omega^2 M_j}{\left(\omega^2 + \Gamma_j^2\right)} + i\frac{\omega\Gamma_j M_j}{\left(\omega^2 + \Gamma_j^2\right)}, \tag{4.11}$$

where ω is the probing frequency. Accordingly, the stress resulting from an imposed oscillatory strain is described by a complex mechanical modulus, of which the real component represents the ability of the system to reversibly store elastic energy, and is called the storage modulus, while the imaginary component measures the amount of energy that is dissipated into heat and is referred to as the loss modulus. As can be seen after regrouping the term for the imaginary component of the complex modulus, the loss modulus is related to the real component of a frequency dependent complex viscosity according to

$$M_j'' = \omega \frac{M_j/\Gamma_j}{\left(1 + \omega^2/\Gamma_j^2\right)} \equiv \omega\eta'. \tag{4.12}$$
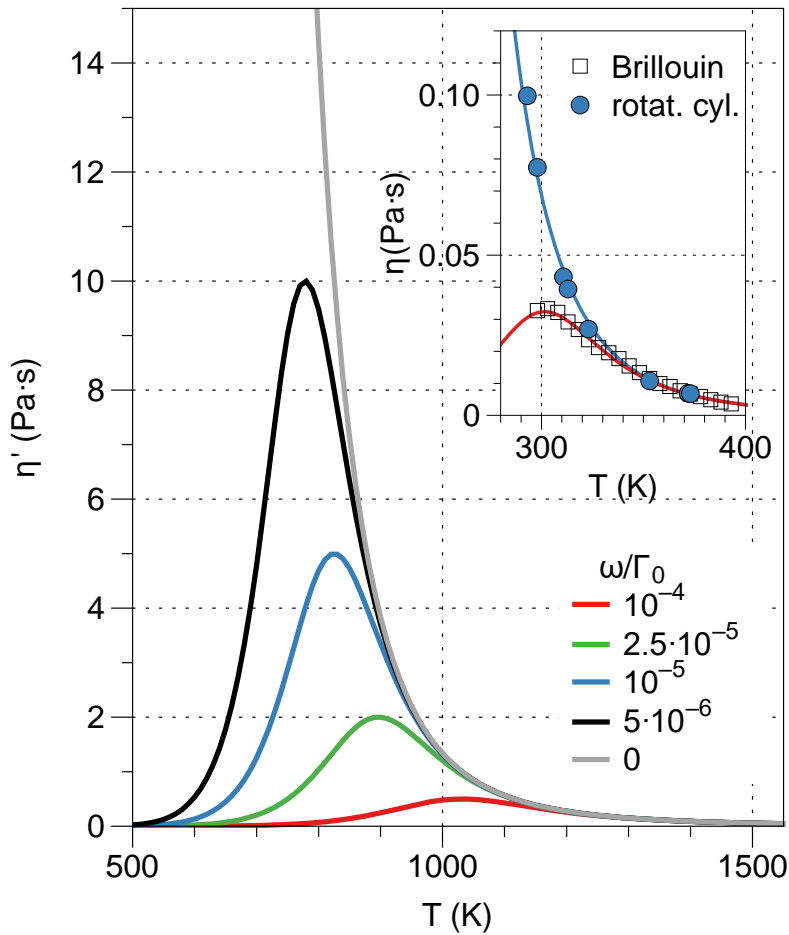
Figure 4-3 Simulated viscosity *vs*. temperature curves as determined using different probing frequencies, for a model substance. Inset: Comparison between the zero-frequency viscosity of a National Institute of Standards and Technology viscosity standard oil and the GHz-frequency data obtained from Brillouin light scattering.

Measurement of these quantities can be carried out using different techniques, including dynamical mechanical analysis (10^{-3}-10^2 Hz), ultrasonic characterization (10^4-10^6 Hz), and inelastic light scattering (10^9-10^{11} Hz). While each of these techniques has its advantages, they all offer access to a relatively narrow frequency range and thus limit the spectroscopic range. Hence, researchers resort to conducting relaxational spectroscopy, where varying the temperature, and consequently the rates of thermally activated processes, facilitates enhanced spectral coverage. With this approach, spectral features such as peaks reflecting resonant absorption of energy are cast from a frequency onto a temperature scale. It is useful, in this

context, to illustrate what to expect in terms of the temperature dependence of the mechanical loss or frequency dependent viscosity coefficients. In **Figure 4-3** we show a series of simulated viscosity *vs.* temperature curves as determined using different probing frequencies, for a model substance. These curves are generated using **Equation 4.12** after dividing all sides by ω and substituting **Equation 4.9** for Γ_j, each with the same values for all parameters, except for the frequency ω.

Accordingly, at zero frequency **Equation 4.12** yields the familiar monotonic decrease of the viscosity with temperature. Indeed, this data would yield a straight line if plotted as the log η vs. $1/T$ plot. However, at finite probing frequencies, the curves exhibit maxima that occur at higher temperatures the higher the frequency. On the high-temperature sides of the maxima, viscosity values determined at different probing frequencies all converge. This is the case when the characteristic relaxation time has dropped below the reciprocal of even the highest frequency. The relaxation process then comes to completion well within the period of the selected phonon. At low temperatures the viscosities drop off sooner the higher the probing frequency. The fact that viscosities vanish when approaching zero temperature, or equivalently, increase with temperature in the low-temperature regime reflects the fact that no viscous processes are sufficiently activated to effect any measurable energy dissipation within the period of the probe. The maximum viscosities correspond to the resonance between probing frequency and relaxation rate, causing the strongest dissipation of energy.

We identify relaxation mechanisms based on their activation energy, E_a, activation entropy, S_a, and attempt frequencies, Γ_0. The temperature at which viscous dissipation peaks is an easily recognizable and unambiguous quantity in relaxational spectroscopy. In general, as with any type of spectroscopy, the more separated spectral features are, the more reliably they can be assigned

to the underlying mechanisms. We now examine how relaxational spectroscopy is affected in this regard by the probing frequency. The relaxation peak maximum is characterized by the condition $(\omega/\Gamma_0)e^{-S_a/k_B}e^{E_a/k_BT^*} = 1$. Solving for the peak position on the temperature scale, T^*, yields

$$T^* = \frac{E_a}{S_a - k_B \ln(\omega/\Gamma_0)}.$$
(4.13)

For this peak temperature, variations of determining factors propagate as

$$\Delta T^* = \frac{\partial T^*}{\partial E_a}\Delta E_a + \frac{\partial T^*}{\partial \Gamma_0}\Delta\Gamma_0 + \frac{\partial T^*}{\partial S_a}\Delta S_a = \frac{1}{S_a - k_B\ln(\omega/\Gamma_0)}\left(1 + E_a\frac{k_B\Delta\Gamma_0/\Gamma_0 + \Delta S_a}{S_a - k_B\ln(\omega/\Gamma_0)}\right).$$
(4.14)

Given that E_a is positive, $(\omega/\Gamma_0)e^{-S_a/k_B} < 1$ and $S_a - k_B\ln(\omega/\Gamma_0) > 0$. However, with increasing frequency, the magnitude of the denominator decreases, which means that the factor magnifying the changes in E_a, Γ_0, and S_a grows. In other words, the higher the probing frequency the more dispersed relaxation peaks are on the temperature scale, and the easier it is to identify the different contributions to a distribution of relaxation mechanisms. This is one advantage of high-frequency probing.

4.3 High-Frequency Viscosity Measurements

Brillouin light scattering (BLS) provides a unique way to determine the complex mechanical modulus by probing materials in the GHz frequency regime. BLS is based on the interaction between light and thermal phonons, which exist naturally in condensed matter at finite temperatures. Considering that the method is contact free and non-invasive, the scattering medium is not perturbed during the measurement; there is no external actuation and the system remains in thermodynamic equilibrium. Light is scattered due to the changes in the dielectric constant associated with density fluctuations. In BLS, the spectrum of scattered light from propagating phonons contains peaks at frequencies that are Doppler-shifted relative to that of the

incident light. Peaks associated with longitudinal and shear deformation modes can be distinguished, and hence, both the longitudinal and shear moduli can be determined using this technique. For a given mode, the frequency shift, ω, is proportional to the velocity of sound and, consequently, can be related to the elastic storage modulus of the scattering medium according to

$$M' = \rho_0 \omega^2 / q^2, \tag{4.15}$$

where ρ_0 is the average density of the scattering medium, $q = 2n/\lambda \sin \theta/2$, is the wavevector, θ is the angle between the incident and scattered light, n is the refractive index of the scattering medium, and λ the wavelength of the light. Conversely, phonon wave attenuation causes peak broadening of the Brillouin peaks, and hence, the loss modulus is obtained as

$$M'' = \omega \eta' = \omega \rho_0 \Delta\omega / q^2, \tag{4.16}$$

where $\Delta\omega$ is the full width at half maximum of the Brillouin peak. Hence, both components of the complex mechanical modulus are derived from a single spectrum. Details with regard to the technique and data analysis can be found in the pertinent literature.[35–39] Here we summarize the most salient points. Although the procedural spatial resolution of the BLS technique is about 25 µm using conventional optics and 1 µm using microscope optics, the phenomenological resolution is of the order of 100 nm. This is about half the wavelength of the phonon probed in the measurement, i.e., the size of the region that is under tensile deformation at any given moment, which corresponds to the length of the dog bone sample in an equivalent tensile testing experiment.

Importantly, because of the high frequency, heat exchange between the scattering location and its surroundings is negligible, and the measured quantities represent the elastic response of the materials in the adiabatic (or isentropic) limit, i.e., they relate to only the potential energy change associated with the elastic deformation. Similarly, the measured viscous dissipation occurs on the

same time scale as atomic jumps. The viscous processes detected using BLS are based on the momentum exchanged between structural moieties, and hence, most closely gauge the mechanisms underlying Eyring's theory.

4.4 Data

Our objective is to explore the connection between viscosity data obtained using rotating cylinder viscometry (or other suitable steady state techniques) and those obtained using BLS, i.e., comparing the viscoelastic response of glass forming liquids at 0 Hz and ~10^{10} Hz. Our evaluation is aimed at deriving new insights from this comparison. Here we focus on the analysis and the ensuing enhancement of the applicable conceptual framework. To this end we concentrate on viscosity data for a representative sodium borate system containing 32 mol.% Na_2O. The BLS data was measured in our lab using a Sandercock six-pass tandem Fabry-Pérot interferometer.[35, 39] The sample was suspended by a double-loop wire in a resistively heated furnace. The incident light, with a wavelength of 514 nm, entered the furnace vertically from the bottom and the scattered light was collected horizontally, i.e., at a 90° scattering geometry. Further details can be found in reference [38]. The zero-frequency data is obtained from the SciGlass database, as referenced by Cassar.[40] **Figure 4-4 (a)** shows both components of the complex mechanical modulus measured using BLS, whereas **Figure 4-4 (b)** shows the measured zero-frequency viscosity as well as the loss modulus data from (a) converted to zero frequency simply by dividing M" by ω. The nature of the various fit lines is discussed in the next section. Note how the viscosity data measured at zero frequency and at GHz-frequencies line up at high temperatures (low β). This demonstrates that the viscosity measured using BLS indeed yields the correct magnitudes, which is important for the data analysis discussed below. The data shown in the inset of **Figure 4-3** for a viscosity standard serves the same validation purpose.

4.5 Analysis and Discussion

4.5.1 The Maxwell-Wiechert Model and its Limitations

It has long been accepted that, considering the structural complexity and disorder in most glass forming liquids, it is sensible to assume that more than one Maxwell element is required to describe the viscoelastic response of such a liquid. The above **Equation 4.11** is therefore expanded to a linear combination of terms,

$$M^* = M_0 + \Delta M_0 \psi(\beta) + \left(\sum_{j=1,n} \frac{\omega^2}{(\omega^2 + \Gamma_j^2)} M_j \right) + i \left(\sum_{j=1,n} \frac{\omega \Gamma_j}{(\omega^2 + \Gamma_j^2)} M_j \right). \tag{4.17}$$

Here we also expanded the leading term, corresponding to the static modulus, to include a temperature dependent factor $\psi(\beta)$, where $\beta = 1/k_B T$. The nature and purpose of this factor is explained in the following. Substituting **Equation 4.9** in **Equation 4.17** leaves us with three fitting parameters per element, M_j, $E_{a,j}$, and $\Gamma_{0,j} e^{S_{a,j}/k_B}$, where the latter factor can evidently be optimized as a grouping. We begin by fitting the loss modulus, which is relatively straightforward. Peak positions are controlled by $E_{a,j}$ and $\Gamma_{0,j} e^{S_{a,j}/k_B}$, allowing us to swiftly narrow down reasonable initial guesses for the parameters, and the magnitude is regulated by M_j. It is also well known that, the number of terms to be used in **Equation 4.17** can easily become ambiguous. Increasing the number of terms after achieving a less than satisfactory fit, typically requires re-optimizing the parameter values previously obtained. In other words, peak positions and magnitudes are not unique but depend on the number of terms used. We therefore aim to achieve the best possible fits with as few terms in **Equation 4.17** as possible, to which end we constrain the range of values each parameter can assume. This prevents parameters from drifting to physically unreasonable values, such as negative M_j values, which are phenomenologically not meaningful but can improve the fit. Similarly, and perhaps less obviously, we want to avaoid

factors such as $\Gamma_{0,j} e^{S_{a,j}/k_B}$ and $e^{-\beta E_{a,j}}$ from straying by more than a couple of orders of magnitude from experiential estimates.

We can simultaneously fit both the loss and storage moduli to optimize the aforementioned three parameters per term, by appropriately constructing a cost function and Jacobian matrices, after making the aforementioned adjustment to the first term in **Equation 4.17**. The need for this adjustment, which we have discussed in earlier publications,[36, 38, 41] becomes obvious when comparing the peak magnitude of *M"* with the change in magnitude of *M'* between the low and high temperature limits. While the former is barely 6.5 GPa the latter is about 55 GPa, more than eight times larger. The problem with this is that *M'* and *M"*, as defined in **Equation 4.11**, are two components of a complex quantity and therefore must obey the Kramers-Kronig transformation. Accordingly, one would expect that the peak loss modulus values amounts to half the change in the storage modulus. Hence, the overall change in storage modulus cannot simply be attributed to the sum of all relaxational moduli M_j. Indeed, the relaxational modulus is a concept based purely on the dynamics of a structurally unchanging system.
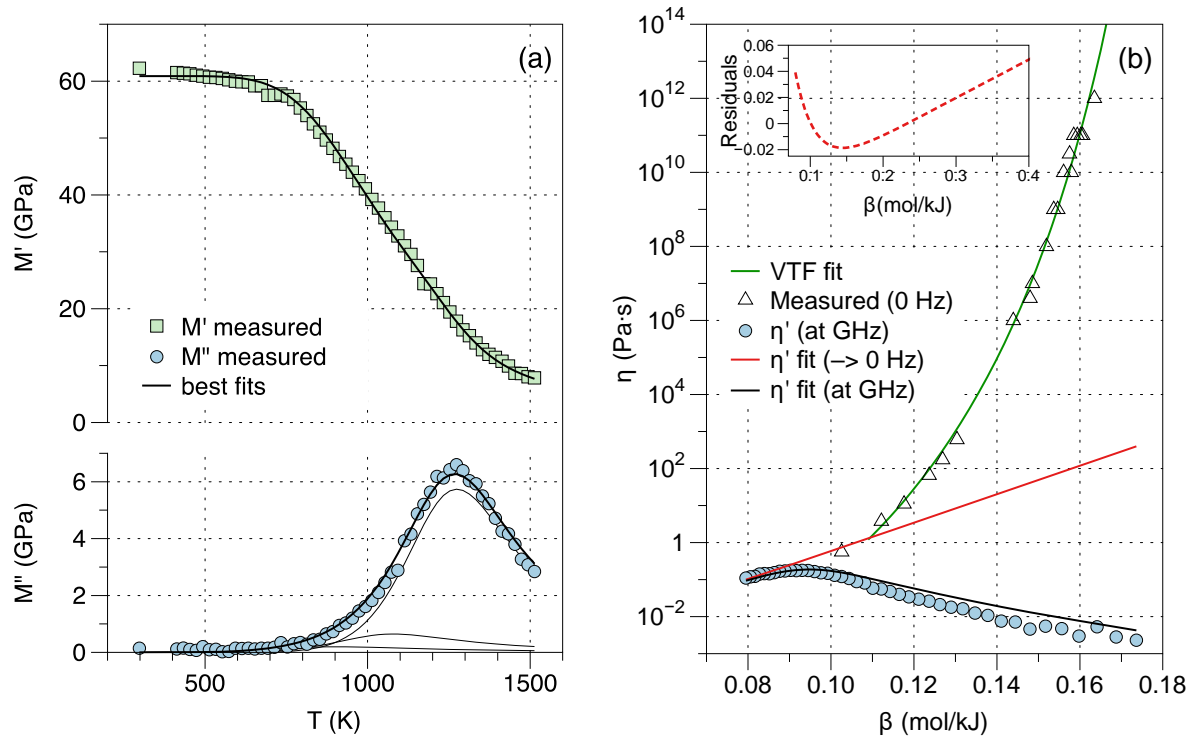
Figure 4-4 (a) Real and imaginary components of the complex mechanical modulus as a function of temperature measured using Brillouin light scattering, and best fits using a linear combination of Maxwell elements (see text). Note that the scales for M' and M" are different. (b) Measured zero-frequency viscosity and high-frequency viscosity converted from M" in (a). The black and green lines represent best fits using applicable model (see text). The red, nearly straight line represents a conversion to zero frequency of the expression that yields the best fit of the high-frequency viscosity. The inset shows the deviation of the red line from linear, i.e., from Arrhenius behavior.

Instead, we must account for an intrinsic structural reconfiguration when the material transitions from liquid to glass.[42–44] This is accomplished by the first term in **Equation 4.17**, which for now only applies to the static modulus. Essentially, the change in elastic modulus is described by the so-called logisitic function, $\psi(\beta)$. We can think of $\psi(\beta)$ as describing the change in a property of a material as it relates to a change in its thermodynamic state. As this thermodynamic change occurs, related changes in potential energy, structural order parameters, and physical properties can be observed. And while they all transition between a starting and ending value, they likely do not follow the same path. Hence, the logistic function is ultimately an abstract, but effective model expression. This construct has been employed in fields including epidemiology,[45, 46] behavioral sciences,[47] ecology,[48] economics,[49] and chemistry.[50] The logistic function is derived

from a type of reaction equation in which both the beginning and ending state weigh in, i.e. (in simplified form),

$$\frac{\partial \psi(\beta)}{\partial \beta} = H\psi(\beta)(1 - \psi(\beta)^\nu), \tag{4.18}$$

where H is a coefficient describing the rate of change with respect to the independent variable (i.e., driving force), and ν serves to distribute the weight of influence of either the beginning or ending state on the progress of the transformation (skewedness). This differential equation has the closed form solution,

$$\psi(\beta) = \left(1 + C_0 e^{-\nu H(\beta - \beta_C)}\right)^{-1/\nu}, \tag{4.19}$$

where β_C corresponds to the location at which the value of the function $\psi(\beta_C)$ must be known to define the integration constant C_0. For example, with $\nu = 1$, **Equation 4.19** describes the partitioning in a two-level system and H represents the energy difference between levels. We used the function in this form in our earlier publications.[36, 38, 41] However, it is safe to assume that if the potential energy of the system changes in a certain way as a function of β, other properties do not follow the exact same pattern. For example, it may be the case that the modulus changes more rapidly as the structure settles into the solid glass configuration than at high temperature, when the structure is in flux, even though the energy changes slow near T_g. Such a scenario is described by values of $\nu > 1$. We therefore treat β_C, ν and H as additional fitting parameters, especially for the applications of $\psi(\beta)$ discussed in the next section. Specifically, H controls the steepness of the changeover, ν the degree of asymmetry, and β_C is expected to closely approximate $1/k_B T_g$. With this, the best fits of the BLS data using **Equation 4.17** are shown in **Figure 4-4 (a)**. In addition to the temperature dependent static modulus, we used three relaxational terms of which one dominates, while the other two terms improve fitting the details.

Accordingly, the dominant relaxation mechanism is characterized by an activation energy of 89.0 kJ/mol, while that of the secondmost important mechanism is 56.1 kJ/mol. We further analyze these figures in the next section.

Next, we examine how these findings compare to the zero-frequency viscosity data from the literature for the same sodium borate system. To this end we divide the measured loss modulus data and each parameterized term of the fitting function by the probing frequency, which yields

$$\eta' = \sum_{j=1,n} \frac{\Gamma_j}{\left(\omega^2 + \Gamma_j^2\right)} M_j = \sum_{j=1,n} \frac{\Gamma_{0,j} e^{Sa/k_B} e^{-\beta E_{a,j}}}{\left(\omega^2 + \Gamma_{0,j}^2 e^{2Sa/k_B} e^{-2\beta E_{a,j}}\right)} M_j,$$

(4.20)

and plot the results as a function of β in **Figure 4-4 (b)**, where they appear as circular symbols along with the best fit line towards the bottom. The maximum in the data can be identified as a shallow bump because of the log scale of the ordinate. We then set the frequency in **Equation 4.20** to zero, simplifying the expression to $\lim_{\omega \to 0} \eta' = \sum_{j=1,n} \left(M_j / \Gamma_{0,j}\right) e^{-Sa/k_B} e^{\beta E_{a,j}}$. The resulting curve is the red line, which appears to be linear and ascends towards increasing β. On the high-temperature side of the maximum, the red line forms the tangent to the fitting curve and measured data. The zero-frequency viscosity data from the literature is plotted as triangular symbols, exhibiting the characteristic curvature of a moderately fragile liquid ($m = 25$). The solid green line fitting this data is based on the Vogel-Tammann-Fulcher (VTF) equation, $\eta = \eta_0 e^{B/(T-T_0)}$. While at high temperatures we observe good agreement between viscosity data obtained at zero frequency and at 20 GHz, both in terms of magnitude and asymptotic temperature dependence, the loss modulus data converted to zero frequency significantly fails when extrapolated to low temperatures. Note that the red line deviates slightly from linear (see inset with residuals) as a result of the contributions from three relaxation mechanisms, but the curvature this produces is nowhere near that exhibited by the measured data.

4.5.2 Non-Linear Corrections

In our earlier publications we concluded that BLS simply does not resolve viscous dissipation losses at low temperatures, and therefore, a correct extrapolation may not be expected. On the other hand, the combination of both components of the complex modulus does reveal how the structure transitions from readily dissipating mechanical energy to storing it elastically. Furthermore, a related recent study has yielded important new insights into the matter. When investigating ionic conductivity in mixed network forming glasses, we discovered a strong correlation between the activation energy for cation hopping and the adiabatic elastic modulus as determined using BLS.[51] Indeed, a number of decades ago already, Frenkel[52] and subsequently Anderson and Stuart[53] used elastic moduli in their formulation of TST to describe atomic transport in liquids and amorphous materials. This approach is based on the notion that for an atom to jump from one stable site to the next atoms in the vicinity of the trajectory reversibly spread apart to open a passageway, which requires an elastic deformation. We elaborated on our observation and improved upon the Anderson-Stuart model. Our analysis shows that the activation energy is supplied to the site of the hopping event by a fortuitous overlap of phonons, focused not on the hopping atom alone but on a small region surrounding this atom, i.e., the affected volume, involving about 30 neighbors. These neighbors undergo displacements beyond their normal vibrational motions, which synchronize with the motion of the hopping atom so as to allow for the elementary transport event. The volume affected by the hopping process can be evaluated by comparing the activation energy (energy per hopping atom) with the adiabatic bulk modulus (energy per volume), with knowledge of the average phonon amplitude (e.g., as derived from the Debye-Waller factor).[51] Multiplying the affected volume so obtained by the atomic number density $\rho_{N,j}$ yields the number of atoms participating in the hopping process. The reason

why the atomic transport activation energy correlates specifically with the adiabatic modulus has to do with the fact that the rate of deformation of the affected volume must be commensurate with the instantaneous velocity of jumping atom.

The data in **Figure 4-4 (a)** informs that the elastic modulus increases with decreasing temperature, significantly exceeding the relaxational modulus. This implies that upon cooling, the structure of the supercooled liquid changes, allowing for higher packing density, relaxation of covalent bonds, and optimization of non-bonding interactions. Therefore, it stands to reason that (1) we must anticipate that the stiffness in all structure types increases upon cooling, and (2) the activation energies for the associated relaxation mechanisms follow along with the increases in moduli. Hence, for the improved version of our viscoelastic model we assume temperature dependences for the relaxational moduli and corresponding activation energies as described by

$$M_j(\beta) = M_{0,j} + \psi_j(\beta)\Delta M_j, \text{ and} \tag{4.21}$$

$$E_{a,j}(\beta) = E_{0,j} + \psi_j(\beta)\Delta E_j. \tag{4.22}$$

Substituting these expressions in **Equation 4.9** yields $\Gamma_j(\beta) = \Gamma_{0,j}e^{S_{a,j}/k_B}e^{-\beta E_{a,j}(\beta)}$ and in **Equation 4.17** it yields

$$M^* = M_0 + \Delta M_0 \psi(\beta) + \left(\sum_{j=1,n}\frac{\omega^2}{\left(\omega^2 + \Gamma_j^2(\beta)\right)}M_j(\beta)\right) + i\left(\sum_{j=1,n}\frac{\omega\Gamma_j(\beta)}{\left(\omega^2 + \Gamma_j^2(\beta)\right)}M_j(\beta)\right). \tag{4.23}$$
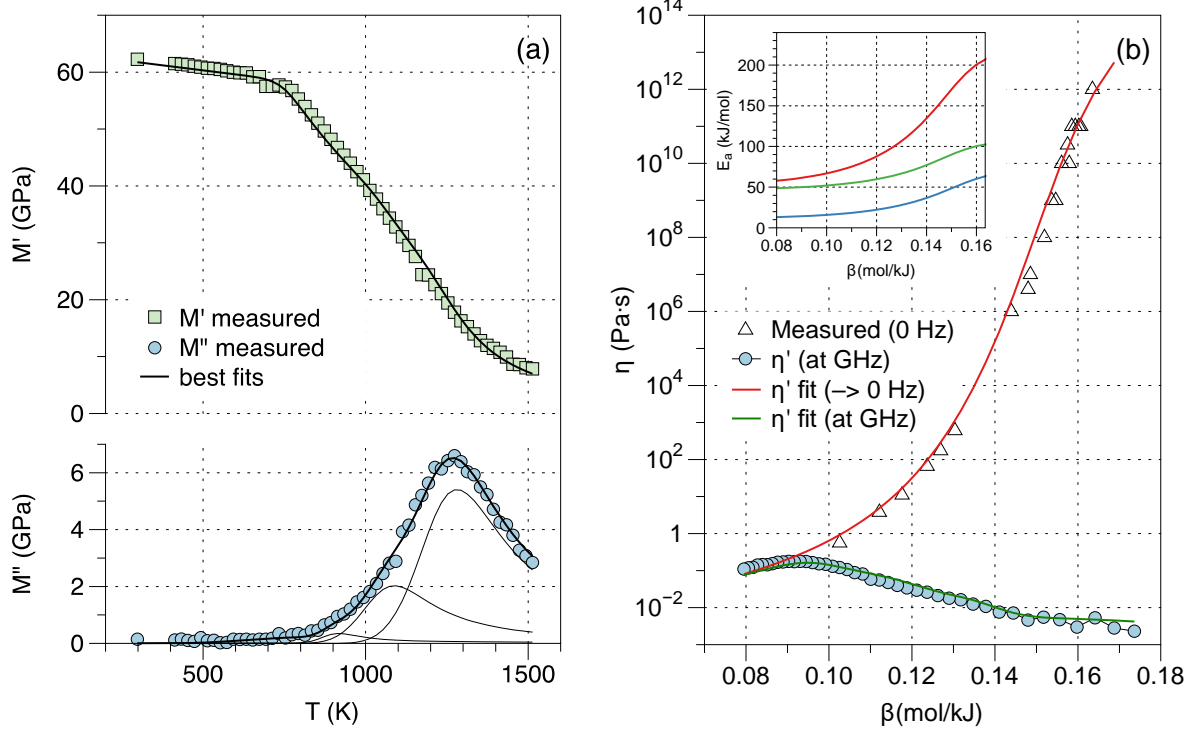
Figure 4-5 (a) Real and imaginary components of the complex mechanical modulus as a function of temperature measured using Brillouin light scattering, and best fits using the enhance viscoelastic model in which both relaxational moduli and activation energies for each relaxation mechanism possess an additional intrinsic temperature dependence introduced by the logistic function. Note that the scales for M' and M" are different. (b) Measured zero-frequency viscosity and high-frequency viscosity converted from M" in (a). The green line represents best fits using applicable model (see text). The red line represents a conversion to zero frequency of the expression that yields the best fit of the high-frequency viscosity assuming temperature dependent activation energies and relaxational moduli for each relaxation mechanism. The inset shows the best fit activation energies for the three relaxation mechanisms as a function of b.

Note that in **Equation 4.9**, Γ_j is already explicitly a function of β, but now it has a second implicit dependence on β. Also, strictly speaking we should consider a similar β-dependence of $S_{a,j}$. However, given the estimated magnitude of the entropy, this would not have a very noticeable effect on the fitting quality, and in light of the noise in the experimental data, the accuracy with which the entropy could be determined is questionable. We therefore fit the enhanced expression again with the grouping $\Gamma_{0,j} e^{S_{a,j}/k_B}$ as a single parameter. Finally, we formally allow for the logistic function to be specific to the relaxation mechanism. It turns out that very little adjustment pertaining only to the value of β_C is required. This is consistent with the notion that the logistic function originates with the concept of structural changes, and

consequently, all properties reflective of this structure should have a similar temperature dependence. Only the static modulus requires different fitting parameters. The possibility for the activation energy to be temperature dependent has been considered by other authors.[54–56] We arrived at this hypothesis independently, following a different trail of indications, thus lending the notion additional credibility.

The results of our analysis are summarized in **Figure 4-5**. The contents are structured similar to that in **Figure 4-4**. Again, pane (a) shows the experimental data obtained from BLS and the best-fit curves using **Equation 4.23**. Compared to **Figure 4-4 (a)**, now the temperature dependent activation energy causes the relaxation peaks to be more asymmetric, i.e., the low-temperature flank rises more abruptly, and the high-temperature tail is more stretched out. This requires a stronger weight to be attributed to low-activation energy peaks, making them more relevant to the fitting procedure. The important differences can be observed in **Figure 4-5 (b)**, which also shows the loss modulus data divided by the frequencies as circular symbols, overlayed by a line representing the function

$$\eta' = \sum_{j=1,n} \frac{\Gamma_j(\beta)}{\left(\omega^2 + \Gamma_j^2(\beta)\right)} M_j(\beta) = \sum_{j=1,n} \frac{\Gamma_{0,j} e^{S_a/k_B} e^{-\beta E_{a,j}(\beta)}}{\left(\omega^2 + \Gamma_{0,j}^2 e^{2S_a/k_B} e^{-2\beta E_{a,j}(\beta)}\right)} M_j(\beta), \tag{4.24}$$

evaluated using the parameters obtained by fitting the loss modulus in **Figure 4-5 (a)** using **Equation 4.23**. Finally, setting the frequency in **Equation 4.24** to zero, i.e.,

$$\lim_{\omega \to 0} \eta' = \sum_{j=1,n} \left(M_j(\beta)/\Gamma_{0,j}\right) e^{-S_a/k_B} e^{\beta E_{a,j}(\beta)}, \tag{4.25}$$

we obtain the red line, which now fits the zero-frequency viscosity very well. We emphasize that this data was not directly fit using **Equation 4.25**, but all parameters were determined by fitting an entirely different set of data, namely the high-frequency complex modulus obtained using BLS. Also, note that for the conversion and extrapolation according to **Equation 4.24** and **4.25**

we used the longitudinal modulus measured at high frequency, and compare the result to the zero-frequency shear viscosity. Consequently, we do not anticipate a perfect match between the red line and the triangular symbols in **Figure 4-5 (b)**. It turns out that for inorganic network glasses and their melts, the longitudinal modulus is about a factor 2 to 3 times higher than the shear modulus, which on the logarithmic scale barely exceeds the scatter in the zero-frequency viscosity data. Indeed, the red line runs consistently above the triangular symbols by about the expected amount.

The temperature dependent activation energies resulting from this analysis are plotted in the inset of **Figure 4-5 (b)** as a function β. Accordingly, that of the dominant term varies from just under 60 kJ/mol at high temperatures to about 200 kJ/mol near T_g. The high-temperature magnitudes are commensurate with the typical activation energy for atomic transport in a liquid, whereas those near T_g are still considerably lower than the bond energies in these oxide systems. Deviation from Arrhenius behavior is a direct consequence of the temperature dependence of the activation energy. However, the shape of the logistic function does affect the quality of agreement between the zero-frequency viscosity data and **Equation 4.25**. It appears that large values of ΔE_j and values of $\nu > 1$ are representative of more fragile liquids. We chose **Equation 4.19** as the form of the logistic function in our analysis for its roots in thermodynamics, but we continue to explore alternative forms.

By comparison, the VTF fit yields a pseudo-activation energy $R \cdot B = 63$ kJ/mol. In the VTF model, the factor B is compared to only a fraction of the available thermal energy; it therefore is not an activation energy in the sense of TST, and generally underestimates the actual energy required for the activated process. The values $\Gamma_{0,j} e^{S_{a,j}/k_B}$ range right around 10^{14} s^{-1}, which is consistent with activation entropies ranging from 10-20 J/mol•K and an affected volume of the

116

order of 10 $Å^3$. These values are all physically meaningful, and we therefore conclude that our model not only provides excellent numerical fits to the data, but also yields sensible insights with regard to the underlying phenomenology.

Finally, we have confirmed that our analysis approach is consistently applicable to other glass forming oxides, covering a wide fragility range. However, a full report on our composition dependent findings risks overwhelming the present account and is therefore planned for a future publication. For now, we summarize that the more fragile a liquid, the more rapidly the adiabatic storage modulus changes as a function of temperature.[36–38]

4.6 Conclusions

BLS provides access to unique materials characteristics of glass forming systems, namely the adiabatic complex mechanical modulus as a function of temperature across the glass transition. The technique yields a storage modulus that starts out in the tens of GPa at ambient conditions, decreases rapidly above the glass transition temperature, and towards high temperatures stabilizes at a single-digit finite value corresponding to the bulk modulus of the liquid. The associated loss modulus exhibits a maximum in the vicinity of steepest descent in the storage modulus. Based on this appearance, a description of mechanical response using the MW model for viscoelasticity therefore seems indicated, except that the two components of the complex modulus do not observe the Kramers-Kronig transformation. This discrepancy can be eliminated by accounting for a temperature dependence of the static modulus, modeled using the logistic function, which has the storage modulus grow larger as the system transitions from a liquid to glass on account of the structural changes that occur during this process. With this correction, the high-frequency complex modulus is well described. However, when converting the loss modulus to viscosity, and extrapolating the MW expression to zero frequency, it only fits the viscosity

117

obtained using rotating cylinder viscometry asymptotically in the high-temperature limit. To remedy this shortfall we must consider that the relaxational moduli and, importantly, the activation energies for viscous dissipation for all Maxwell elements, since the two quantities are correlated, also exhibit a temperature dependence. Only then, using a similarly parameterized logistic function to describe this temperature dependence, can we achieve a satisfactory description of the zero-frequency viscosity. Hence, the structural changes in the glass transition regime not only affect the static modulus, but all mechanical responses of the supercooled liquid structure, which includes the activation energies for atomic motion, as these rely on elastic deformations of their surroundings. Note that the activation free energy is strictly a feature of the energy landscape, namely the difference between the free energy of the activated complex and that of the ground state. Then, because the deviation from Arrhenius behavior of the viscosity is a direct consequence of the change in activation energies and entropies with temperature, the fragility of a glass forming liquid can be regarded as a measure of the rate of change with temperature in the energy landscape topography.

4.7 References

1 H.S. Chen and D. Turnbull, 'Viscosity of Metallic Glass of Gold-Silicon-germanium Alloy,' *Journal of Metals* **20**, A10 (1968).

2 A.J. Easteal, E.J. Sare, C.T. Moynihan, and C.A. Angell, 'Glass-Transition Temperature, Electrical Conductance, Viscosity, Molar Volume, Refractive Index, and Proton Magnetic Resonance Study of Chlorozinc Complexation in the System $ZnCl_2 + LiCl + H_2O$,' *J. Solution Chem.* **3**, 807 (1974).

3 G.S. Fulcher, 'Analysis of recent measurements of the viscosity of glasses,' *J. Am. Ceram. Soc.* **8**, 339 (1925).

4 W. Haller, J.H. Simmons, and A. Napolitano, 'Critical Immiscibility Measurements of Technical Glasses By a Viscosity Drift Method,' *Am. Ceram. Soc. Bull.* **49**, 424 (1970).

5 H. Le Chatelier, 'The viscosity of glass,' *Comptes Rendus Hebdomadaires des Seances de l'Academie des Sciences* **179**, 517 (1924).

6 O.V. Mazurin, M.V. Streltsina, and A.S. Totesh, 'Viscosity and Transformation Temperature of Phase-Separated Sodium Borosilicate Glasses,' *Phys. Chem. Glasses* **10**, 63 (1969).

7 C.T. Moynihan, C.R. Smalley, C.A. Angell, and E.J. Sare, 'Conductance, Viscosity, Density, Proton Magnetic Resonance Spectra, and Glass Transition Temperatures of Calcium Nitrate Tetrahydrate-Cadmium Nitrate Tetrahydrate Melts. An Ideal Fused Salt System,' *J. Phys. Chem.* **73**, 2287 (1969).

8 A. Napolitano and E.G. Hawkins, 'Viscosity of Standard Soda-Lime-Silica Glass,' *Journal of Research of the National Bureau of Standards Section a-Physics and Chemistry* **A 68**, 439 (1964).

9 A. Napolitano, J.H. Simmons, D.H. Blackburn, and R.E. Chidester, 'Analysis of Low-Temperature Viscosity Data for 3 NBS Standard Glasses,' *Journal of Research of the National Bureau of Standards Section A-Physics and Chemistry* **A 78**, 323 (1974).

10 M. Prodhomme, 'Transformation Temperature and Viscosity of Glass,' *Revue Internationale Des Hautes Temperatures Et Des Refractaires* **12**, 79 (1975).

11 J.E. Shelby, 'Viscosity and Thermal-Expansion of Alkali Germanate Glasses,' *J. Am. Ceram. Soc.* **57**, 436 (1974).

12 T. Takamori and M. Tomozawa, 'Viscosity and Microstructure of Phase-Separated Borosilicate Glasses,' *J. Am. Ceram. Soc.* **62**, 373 (1979).

13 A.Q. Tool, 'Viscosity and the Extraordinary Heat Effects in Glass,' *Journal of Research of the National Bureau of Standards* **37**, 73 (1946).

14 S.A. Arrhenius, 'Über die Reaktionsgeschwindigkeit bei der Inversion von Rohrzucker durch Säuren,' *Z. Phys. Chem.* **4**, 226 (1889).

15 C.A. Angell, 'Strong and Fragile Liquids Relaxations in Complex Systems,' *National Technical Information Service, US Department of Commerce* 3 (1984).

16 C.A. Angell, A. Dworkin, P. Figuiere, A. Fuchs, and H. Szwarc, 'Strong and Fragile Plastic Crystals,' *J. Chim. Phys. Phys.-Chim. Biol.* **82**, 773 (1985).

17 C.A. Angell, 'Structural Instability and Relaxation in Liquid and Glassy Phases Near the Fragile Liquid Limit,' *J. Non-Cryst. Solids* **102**, 205 (1988).

18 C.A. Angell, 'Formation of Glasses From Liquids and Biopolymers,' *Science* **267**, 1924 (1995).

19 R. Bohmer, K.L. Ngai, C.A. Angell, and D.J. Plazek, 'Nonexponential Relaxations in Strong and Fragile Glass Formers,' *J. Chem. Phys.* **99**, 4201 (1993).

20 L.M. Wang, C.A. Angell, and R. Richert, 'Fragility and thermodynamics in nonpolymeric glass-forming liquids,' *J. Chem. Phys.* **125**, 074505 (2006).

21 L.M. Wang, V. Velikov, and C.A. Angell, 'Direct determination of kinetic fragility indices of glassforming liquids by differential scanning calorimetry: Kinetic versus thermodynamic fragilities,' *J. Chem. Phys.* **117**, 10184 (2002).

22 C.A. Angell, 'Entropy and fragility in supercooling liquids,' *Journal of Research of the National Institute of Standards and Technology* **102**, 171 (1997).

23 L.M. Martinez and C.A. Angell, 'A thermodynamic connection to the fragility of glass-forming liquids,' *Nature* **410**, 663 (2001).

24 R. Richert and C.A. Angell, 'Dynamics of glass-forming liquids. V. On the link between molecular dynamics and configurational entropy,' *J. Chem. Phys.* **108**, 9016 (1998).

25 S. Sastry, 'The relationship between fragility, configurational entropy and the potential energy landscape of glass-forming liquids,' *Nature* **409**, 164 (2001).

26 D.L. Sidebottom, 'Connecting Glass-Forming Fragility to Network Topology,' *Frontiers in Materials* **6**, 144 (2019).

27 D.L. Sidebottom, 'The fragility of alkali silicate glass melts: Part of a universal topological pattern,' *J. Non-Cryst. Solids* **516**, 63 (2019).

28 H. Eyring, 'Viscosity, plasticity, and diffusion as examples of absolute reaction rates,' *J. Chem. Phys.* **4**, 283 (1936).

29 D. Frisch, H. Eyring, and J.F. Kincaid, 'Pressure and temperature effects on the viscosity of liquids,' *J. Appl. Phys.* **11**, 75 (1940).

30 J.F. Kincaid, H. Eyring, and A.E. Stearn, 'The theory of absolute reaction rates and its application to viscosity and diffusion in the liquid state,' *Chemical Reviews* **28**, 301 (1941).

31 N. Hirai and H. Eyring, 'Bulk Viscosity of Liquids,' *J. Appl. Phys.* **29**, 810 (1958).

32 J. Perez, 'Homogeneous Flow and Anelastic/Plastic Deformation of Metallic Glasses,' *Acta Metallurgica* **32**, 2163 (1984).

33 Q. Hao, G.J. Lyu, E. Pineda, J.M. Pelletier, Y.J. Wang, Y. Yang, and C. Qiao, 'A hierarchically correlated flow defect model for metallic glass: Universal understanding of stress relaxation and creep,' *International Journal of Plasticity* **154**, 103288 (2022).

34   N.W. Tschoegl, '*The Phenomenological Theory of Linear Viscoelastic Behavior*,' (Springer Verlag, Berlin, 1989)

35   J. Kieffer, 'Brillouin Light Scattering,' in *Modern Glass Characterization*, edited by M. Affatigato (Wiley & Sons, Hoboken, NJ, 2015), p. 107.

36 J. Kieffer, J.E. Masnik, O. Nickolayev, and J.D. Bass, 'Structural Developments in Supercooled Alkali Tellurite Melts,' *Phys. Rev. B* **58**, 694 (1998).

37 J. Kieffer, J.E. Masnik, B.J. Reardon, and J.D. Bass, 'High-Frequency Relaxational Spectroscopy in Liquid Borates and Silicates,' *J. Non-Cryst. Solids* **183**, 51 (1995).

38 J.E. Masnik, J. Kieffer, and J.D. Bass, 'The Complex Mechanical Modulus as a Structural Probe: Case of Alkali Borate Liquids and Glasses,' *J. Chem. Phys.* **103**, 9907 (1995).

39 J.R. Sandercock, 'Trends in Brillouin Scattering - Studies of Opaque Materials, Supported Films, and Central Modes,' in *Light Scattering in Solids III*, edited by M. Cardona and G. Güntherodt (Springer, 1982), p. 173.

40 D.R. Cassar, 'Viscnet: Neural Network for Predicting the Fragility Index and the Temperature-Dependency of Viscosity,' *Acta Materialia* **206**, 116602 (2021).

41 J. Kieffer, 'Structural Transitions in Glasses and Glass-Forming Liquids (Morey Award Lecture),' *Ceramic Bulletin* **81**, 73 (2002).

42 L. Huang and J. Kieffer, 'Polyamorphic Transitions and Thermo-Mechanical Anomalies in Network Glasses,' *Glasstechnische Berichte - Glass Science and Technology* **77**, 124 (2004).

43 L. Huang, L. Duffrène, and J. Kieffer, 'Structural transitions in silica glass: thermo-mechanical anomalies and polyamorphism,' *J. Non-Cryst. Solids* **349**, 1 (2004).

44 J. Kieffer, 'Structural Transitions and Polyamorphism in Glass-Forming Oxides,' *J. Non-Cryst. Solids* **307-310**, 644 (2002).

45 S. Mehrolia, S. Alagarsamy, and V.M. Solaikutty, 'Customers response to online food delivery services during COVID-19 outbreak using binary logistic regression,' *International Journal of Consumer Studies* **45**, 396 (2021).

46 D. Xiong, L. Zhang, G.L. Watson, P. Sundin, T. Bufford, J.A. Zoller, J. Shamshoian, M.A. Suchard, and C.M. Ramirez, 'Pseudo-likelihood based logistic regression for estimating COVID-19 infection and case fatality rates by gender, race, and age in California,' *Epidemics* **33**, 100418 (2020).

47 M. Amatria, D. Lapresa, J. Arana, M.T. Anguera, and B. Garzon, 'Optimization of Game Formats in U-10 Soccer Using Logistic Regression Analysis,' *Journal of Human Kinetics* **54**, 163 (2016).

48 J. Pearce and S. Ferrier, 'Evaluating the predictive performance of habitat models developed using logistic regression,' *Ecological Modelling* **133**, 225 (2000).

49 S. Ben Jabeur, 'Bankruptcy prediction using Partial Least Squares Logistic Regression,' *Journal of Retailing and Consumer Services* **36**, 197 (2017).

50 A.J. Dood, J.C. Dood, D.C.R. de Arellano, K.B. Fields, and J.R. Raker, 'Analyzing explanations of substitution reactions using lexical analysis and logistic regression techniques,' *Chemistry Education Research and Practice* **21**, 267 (2020).

51 W. Wang, R. Christensen, B. Curtis, S.W. Martin, and J. Kieffer, 'A New Kinetic Model Linking Elastic Properties and Ion Conductivity in Mixed Network Former Glasses,' *Phys. Chem. Chem. Phys.* **20**, 1629 (2018).

52 J. Frenkel, '*Kinetic Theory of Liquids*,' (Oxford University Press, London, 1947)

53 O.L. Anderson and D.A. Stuart, 'Calculation of activation energy of ionic conductivity in silica glasses by classical methods,' *J. Am. Ceram. Soc.* **37**, 573 (1954).

54 V. Aquilanti, K.C. Mundim, M. Elango, S. Kleijn, and T. Kasai, 'Temperature dependence of chemical and biophysical rate processes: Phenomenological approach to deviations from Arrhenius law,' *Chem. Phys. Lett.* **498**, 209 (2010).

55 V.H. Carvalho-Silva, V. Aquilanti, H.C.B. de Oliveira, and K.C. Mundim, 'Deformed Transition-State Theory: Deviation from Arrhenius Behavior and Application to Bimolecular Hydrogen Transfer Reaction Rates in the Tunneling Regime,' *J. Comput. Chem.* **38**, 178 (2017).

56 B. Schmidtke, N. Petzold, R. Kahlau, M. Hofmann, and E.A. Rossler, 'From boiling point to glass transition temperature: Transport coefficients in molecular liquids follow three-parameter scaling,' *Physical Review E* **86**, 041507 (2012).

Chapter 5 Application of Variable Activation Free-Energy Model to Viscous Processes in Inorganic Oxide Glass-Formers

Abstract

We have developed the workflow for analyzing steady-state viscosity data using our new Variable Activation Free Energy (VAFE) model, reviewing salient points underlying our model and how they factor into the derived formalism and reporting on how our model performs when fitting viscosity data of 847 oxide glass formers. The VAFE model is an enhanced descriptive model for viscosity of glass-forming liquids that not only fits experimental data well but produces quantitative and physically meaningful parameters. Our model takes the structural evolution resulting from traversing the glass transition regime, and thus the variation in the activation barrier, for the viscous process into account. We compared representative fits of the VAFE model with those of the VFT and MYEGA equations and find our model to be more robust to extrapolation and possessing more reasonable behavior in the infinite-temperature limit which simply encodes non-enthalpic contributions to the rate coefficient. It is demonstrated that VAFE model fits can be utilized to gain insight into the effect of the component speciation and composition of glass forming liquids on the viscous process by comparing magnitudes of the fitting parameters. These values can indicate which factors are dominant in dictating the viscosity of specific glass forming compositions and how these factors and their sensitivities to changes in temperature vary as a function of composition. Through analysis using the VAFE

model, we link the temperature-dependent change in potential energy due to structural changes in glass formers to fragility. This enables the reconciliation of temperature-dependent changes in the average ground-state potential energy of the glass forming liquid with changes in viscous activation enthalpy and the ability to estimate the number of atoms involved in the viscous relaxation process which ranges from approximately 10 to 50 atoms for the oxide glass formers studied.

5.1 Introduction

Accurate knowledge of the viscosity of glass forming liquids and its variation with temperature, pressure, and chemical environment is a fundamental aspect of numerous fields of study and technologies, which include macromolecular and polymeric sciences[1,2], ionic and complex liquids[3,4], geophysics[5,6], food and drug sciences[7–9], ceramics[10,11], and metallurgy[12,13]. The ability to navigate the regime of state variables in which the molecular system must be conditioned to prevent it from accessing its thermodynamically stable crystalline state is key to achieving the unique properties associated with materials that are amorphous and monolithic at all length scales. Reliable prediction of the viscosity is essential for regulating working temperatures, establishing proper annealing conditions, suppressing crystal growth, and carrying out physical processing, molding, and shaping of glass and glass-ceramics products.[14–16]

Furthermore, the rapid increase in viscosity with decreasing temperature is perceived to reflect an essential characteristic of the glass transition phenomenon and has therefore spurred a distinct field of scientific study.[2,7,12,17–20] In particular, there are aspirations that a better understanding of what causes such an accentuated change in the structural relaxation rates of glass forming systems may provide insights into the nature of the amorphous state of matter, a mystery that has thus far remained impervious to conventional structural probes. To this end, it is necessary to connect viscosity with the underlying molecular scale processes. In the early 1930s, Eyring derived his model for the viscosity coefficient, which provides a formalism that can be used to quantify the elementary mechanisms of this complex process on the basis of transition state theory.[21] Calculation of viscosity requires the evaluation of the relaxation rate where the system

must overcome and activation barrier from one equilibrium state to another. The relaxation rate is shown to principally depend on the factors described in the following equation,

$$\Gamma \propto \left(\frac{Q_a}{Q_g}\right) e^{\frac{-E_a}{k_B \cdot T}},$$ (5.1)

where Q_g is the ground-state partition function, Q_a is the activated-state partition function, k_B is the Boltzmann constant, E_a is the activation energy required for the process to occur, and T is the temperature.[21] The difference between the natural logarithms of the activated and ground state partition functions is equal to S_a, or the entropy of activation. This is the difference in entropy, or difference in the number of equivalent energy microstates, between the activated and grounds states. The amount of energy dissipated in viscous flow is inversely proportional to the relaxation rate, so Eyring's equation for viscosity is written as,

$$\eta = h \frac{\lambda_z}{\lambda_x \lambda_y \lambda^2} e^{\frac{-S_a}{k_B}} e^{\frac{E_a}{k_B \cdot T}} = h\rho_N e^{\frac{-S_a}{k_B}} e^{\frac{E_a}{k_B \cdot T}},$$ (5.2)

where h is Planck's constant and $\rho_N = \lambda_z/(\lambda_x \lambda_y \lambda^2)$. The various l-parameters represent the characteristic length scales on which the elementary relaxation mechanism takes place. Specifically, Eyring conceived of two layers of a liquid being sheared passed one another in opposite directions as a result of an applied shear stress $\pm\tau_{zx}$. Rather than sliding past one another steadily and simultaneously as a collective, the molecular entities jump individually from one equilibrium position to the next in a stochastic fashion. In due course all molecules jump eventually with an average bias in the direction of the applied shear stress. In this description, λ_z is the distance between the liquid layers, λ_x and λ_y make up the per atom contact area of the layers, and λ is the atomic jump distance of the mechanism. The length parameters λ, λ_x, λ_y, and λ_z are all on the order of the interatomic spacing and together can be combined to represent the

126

reciprocal volume, ρ_N, involved in the jump mechanism. **Equations 5.1** and **5.2** assume that the energy and entropy of activation are constant. That is that these values, and therefore the potential energy surface of the structure they arise from, do not change as a function of temperature. This formalism adequately describes the temperature dependence of the viscosity coefficient for simple liquids, resulting in a linear relationship between the logarithm of the viscosity and inverse temperature, 1/T. However, this equation is unable to capture the complex viscous characteristics of most glass-forming liquids.

For most glass forming liquids, the temperature dependence of viscosity deviates from the semilogarithmic linearity of Eyring's equation in ways reflected by a steeper slope at low temperatures and a shallower slope at high temperatures. The underlying reason for the deviation from Arrhenius behavior in the temperature dependence of the viscosity has been a factor of intense scrutiny.[18,20,22,23] Austen Angell plotted viscosity data for various types of glass forming liquids vs. reciprocal temperature normalized with respect to the glass transition temperature, T_g, thereby devising the so-called Angell plot shown in **Figure 5-1**, which casts the viscosity profiles onto a set of master curves. Based on this observation, he conceived the concept of strong vs. fragile behavior to categorize the temperature dependence of the viscosity for glass forming systems.[24–28] This paradigm has enabled researchers to better gauge, label, and interpret their findings. The more the $\log_{10}(\eta)$ vs. T_g/T data deviates from linearity, the more "fragile" the liquid is said to be, while nearly linear, or Arrhenius, behavior is designated as "strong".[29] To quantify this phenomenon, various fragility indices have been suggested to date. The most commonly utilized of these is the kinetic fragility, m, which is based on the slope of the log viscosity versus inverse temperature relationship at the glass transition temperature.[30]
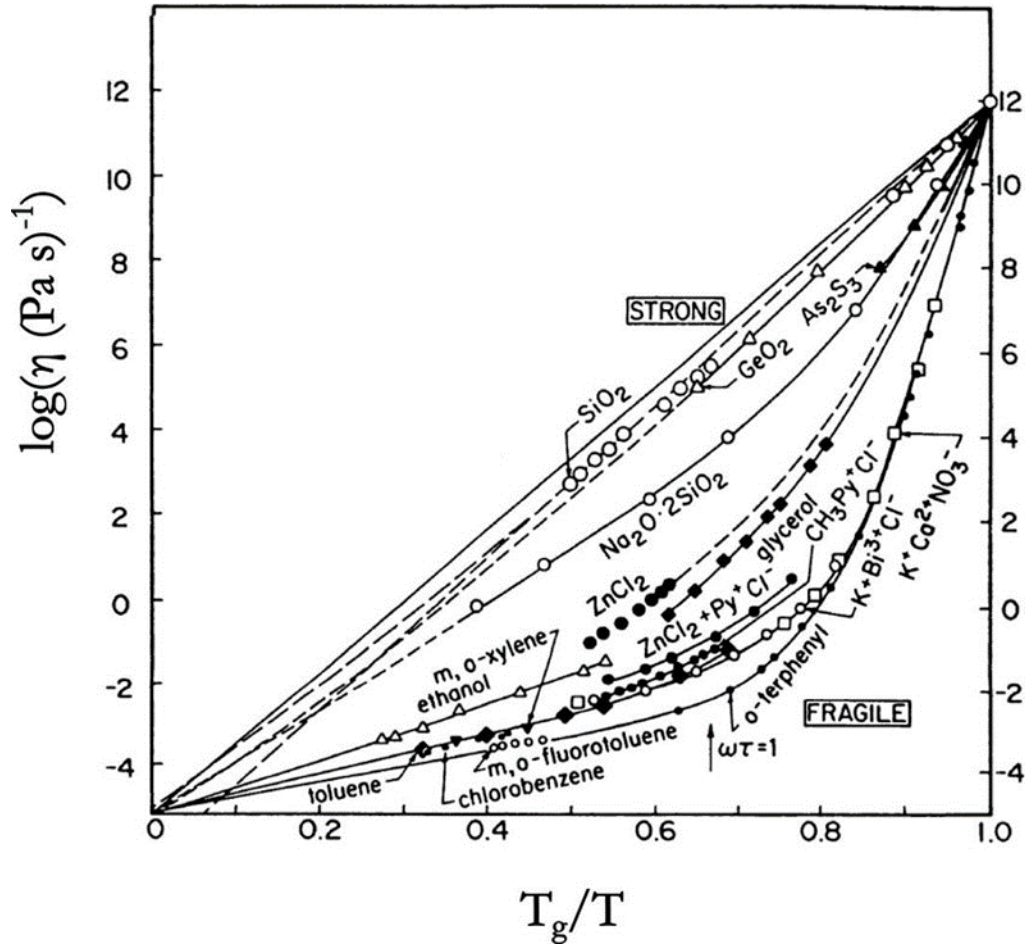
Figure 5-1 Angell Plot depicting the pattern of liquid viscosity-temperature relations for Tg-based normalization showing contrast between network and molecular or simple ionic liquid behavior.[24]

$$m = \lim_{T \to T_g} \frac{\partial \log_{10} \eta}{\partial \left(T_g/T\right)} \tag{5.3}$$

Despite the progress made towards the development of theoretical frameworks, categorization, and quantitative tools, the structural and physicochemical origin of this non-Arrhenius behavior remains an open question. The most widely used models to date are very successful at interpolating the viscosity-temperature relationship and have some success in extrapolation but yield little insight into the microscopic structural and mechanistic processes affecting viscosity in these glass-forming liquids when relaxation takes on non-Arrhenius character. In our earlier

128

publication,[31] we introduced the basic framework of an enhanced descriptive model for viscosity of glass-forming liquids that not only fits experimental data well but produces quantitative and physically meaningful parameters that can be reconciled with long-successful physics-based models such as transition state theory. Based on the same phenomenological approach as pioneered by Eyring, our model takes the structural evolution resulting from traversing the glass transition regime, and thus the variation in the activation barrier, for the viscous process into account.

In this previous publication, we derived our formalism starting with the complex mechanical modulus of a moderately modified sodium borate glass forming system, obtained in the adiabatic (at ~10^{10} Hz) limit using Brillouin light scattering. We showed that, using our new model, the loss modulus measured at high frequencies can be extrapolated to zero frequency and accurately yield the viscosity measured using steady-state viscometry. Moreover, the temperature dependence of the activation energy for viscous relaxation can be evaluated through combined analysis of the storage and loss modulus. In this context, the importance of utilizing the adiabatic modulus arises from the fact that the atomistic jump processes that underly viscous relaxation also occur on a time scale that does not allow for heat exchange, even with the immediate surroundings. Note that in Eyring's equation, the attempt frequency for atomic hopping, G_0 has been expressed in terms of the generic phonon energy quantum, $G_0 = k_B T/h$, which does not contain materials specific information. With the knowledge of the adiabatic storage modulus of, say for shear deformation, G', we can formally replace $h\rho_N$ in **Equation 5.2** with G'/G_0,[31] where the value for G_0 can be gained from vibrational spectroscopy measurements such as Raman scattering or infrared absorption spectroscopies.

However, short of such measurements, the term $h\rho_N$ can also be treated as a fitting parameter. In the present work, we developed the workflow for analyzing steady-state viscosity data using our new model. We begin by reviewing the salient points underlying our model and how they factor into the derived formalism. We then report on how our model performs when fitting viscosity data of 847 oxide glass formers and how to interpret the results.

5.2 Temperature Dependence of the Activation Free Energy

The dependence of the viscous activation barrier on temperature has been previously asserted by other authors where it is generally believed that, should the activation energy depend on temperature, it increases with decreasing temperature.[32–39] In accordance with this perspective, there have been a modest number of viscosity models put forth that include a temperature-dependent activation energy.[34,40] Starting with **Equation 5.2** and combining the energy and entropy of activation into an activation free energy using the standard thermodynamic definition,

$$G_a = E_a - TS_a, \tag{5.4}$$

and replacing $1/(k_B T)$ with the thermodynamic beta, β, Erying's equation is now in a compact form

$$\eta = h\rho_N e^{\beta G_a}, \tag{5.5}$$

which is more conducive to the following derivation. Next, we take the logarithm of the equation as is commonly done for linearization.

$$\ln(\eta) = \ln(h\rho_N) + \beta G_a \tag{5.6}$$

Allowing for G_a to be a function of β, we take the derivative of **Equation 5.6** with respect to β using the chain rule to get

130

$$\frac{d\ln(\eta)}{d\beta} = G_a(\beta) + \beta \frac{dG_a(\beta)}{d\beta}. \tag{5.7}$$

For a perfectly strong glass former, $dG_a/d\beta = 0$ and G_a is a constant independent of temperature, resulting in a constant slope of $\log_{10}(\eta)$ vs. T_g/T profile, which conforms with Eyring's equation. However, when the $\log_{10}(\eta)$ vs. T_g/T profile exhibits curvature, it must follow that $dG_a/d\beta \neq 0$. Moreover, since the activation free energy compares the energy levels between two specific locations in the free energy landscape, namely the ground state and activated state (or saddle point), a change in the activation free energy with temperature reflects a change in this landscape brought about by structural rearrangements and specific volume changes associated with the material transitioning between liquid and glass. So $dG_a/d\beta$ is the important term here, but we do not know its functional form *a-priori*.

At this juncture, there exist several options. One is to make no direct assumptions about the functional form for $G_a(\beta)$ and expand it as a Taylor series, which in practice amounts to a polynomial regression where the coefficients are determined by fitting to the experimental data. This approach has several disadvantages, the most significant among which is that there is a tendency to over-fit, especially for sparse data sets, and as a result, leads to nonsensical intercepts with the ordinate. Instead, we opted to choose a definitive functional form with a relatively small number of parameters. The approach we have taken is both rooted in thermodynamic and kinetic formalisms and can thus be considered as describing the transition from a liquid to a glass (or vice versa) as a reversible rate phenomenon. The function selected is based on Richard's generalized differential equation, which has the structure of a generic rate equation, shown here applied to the free energy of activation.[41]

$$\frac{dG_a(\beta)}{d\beta} = H \cdot G_a(\beta) \left(1 - \left(\frac{G_a(\beta)}{\Delta G_a} \right)^{\nu} \right) \tag{5.8}$$

Integration of **Equation 5.8** with respect to β yields the generalized logistic function, defined here as $\psi(\beta)$. The logistic function was originally developed to describe population growth but has since been used to model chemical reactions and the spread of communicable diseases, it is commonly used in machine learning applications as an activation function, and it is even present in the functional form governing Fermi-Dirac statistics for the energy distribution of fermions at a given temperature.[42–46]

$$G_a(\beta) = \Delta G_a \psi(\beta) + C_1, \tag{5.9}$$

where

$$\psi(\beta) = \left(\frac{1}{1 + C_0 e^{(-v \cdot H(\beta - \beta_g))}}\right)^{1/v}. \tag{5.10}$$

Equation 5.8 is integrated as a boundary value problem, typically by choosing the value of $\psi(\beta)$ where $\beta = \beta_g$, i.e., at the glass transition temperature, which defines the integration constant C_0. Naturally, the expression for $G_a(\beta)$ is also accepting of a bias C_1. Furthermore, based on the observation that by and large $\log_{10}(\eta)$ vs. T_g/T profiles exhibit their steepest slope at T_g, we also require that the function's inflection point (the root of the second derivative) be located at the glass transition temperature. Finally, we normalize the value to unity, so that within the domain of interest $\beta = 0$ to $\beta = \beta_g$ the function varies between 0 and 1 and also to enforce that the curvature in the viscosity profiles is always greater than or equal to zero. With these constrains, the expression for $\psi(\beta)$ becomes,

$$\psi(\beta) = \left(\frac{1 + v}{1 + v e^{(-v \cdot H(\beta - \beta_g))}}\right)^{1/v} \tag{5.11}$$

where the steepness of the slope is primarily governed by H, while the parameter v is responsible for the degree of asymmetry of the function. A special case for this function results when $v = 1$.

This reduces **Equation 5.11** to the two-level system model commonly used to describe phase relations in thermodynamics. Here, we make no *a-priori* assumption about the value of v and allow these parameters to be optimized via a nonlinear fitting procedure. In the next section the meaning of the parameters v and H is further elaborated on in the context of physicochemical quantities.

Combining **Equations 5.9** and **5.11** results in the description of a variable activation free energy (VAFE), in the present context, one that is temperature dependent. As mentioned above, we already validated our VAFE model by fitting the adiabatic complex mechanical modulus of a sodium borate glass obtained using Brillouin light scattering. In that case, we modified a three-term Maxwell-Weichert model with our VAFE enhancement..[31] This affects the relaxational modulus terms that appear in both the storage and loss modulus, but the effect of the correction is especially noticeable in the storage modulus, as it directly reflects the shape of the logistic function. Demonstrating that viscosity data is equivalent whether it is measured at 0 Hz or 10^{10} Hz frequencies and that values are mutually convertible substantiates the robustness of the VAFE concept. This conformity allows for a more definitive interpretation of structural relaxation mechanisms and their relationship to materials chemistry, and it opens new ways for measuring viscosity.

In the following we describe insights we gained by using the VAFE formalism for viscous dissipation in its zero-frequency limit to analyze a steady-state viscosity data set of 847 oxide glasses.[47] The form of our VAFE model is essentially the same as Eyring's equation, except that the enthalpy and entropy of activation are now both functions of the independent variable χ,

133

where χ is simply equal to T_g/T to put the equation in a form commensurate with that of an Angell plot.

$$\ln \eta(\chi) = \ln(h\rho_N) - \frac{S_a(\chi)}{k_B} + \frac{E_a(\chi)}{k_B T_g} \cdot \chi \tag{5.12}$$

The enthalpy of activation, $E_a(\chi)$, and entropy of activation, $S_a(\chi)$, are given by

$$E_a(\chi) = E_0 + \Delta E \; \psi(\chi) \text{ and} \tag{5.13}$$

$$S_a(\chi) = S_0 + \Delta S \; \psi(\chi), \tag{5.14}$$

which comes directly from our earlier integration using Richard's differential equation. E_0 and S_0 are static quantities that relate closely to the activation enthalpy and entropy in the high temperature liquid state. The values ΔE and ΔS correspond to the magnitude of change in the activation enthalpy and entropy between the high temperature liquid state and the material at its glass transition temperature, while the function $\psi(\chi)$ determines how this occurs with respect to a change in the temperature. The values of the parameters $\ln(h\rho_N)$, S_0, ΔS, E_0, ΔE, H, v, and T_g are unknown for each composition and a nonlinear fitting method is required. The parameters $\ln(h\rho_N)$ and S_0 are both constants and therefore indistinguishable from one another in terms of fitting procedures so these values are combined and fit as a single parameter ($\ln(h\rho_N) - S_0/k_B$). The value of T_g can be calculated as a function of the other parameters so long as the value of the viscosity at the glass transition temperature is known. Since T_g is defined as the temperature at which the viscosity of the supercooled liquid reaches a value of 10^{12} Pa·s, this value is always a known quantity by construction. The value of T_g can therefore be written as,

$$T_g = \frac{E_0 + \Delta E}{k_B \left(\ln(10^{12}) + \frac{S_0}{k_B} + \frac{\Delta S}{k_B} + \ln(h\rho_N) \right)} \tag{5.15}$$

since $\psi(\chi)$ is equal to unity at the glass transition temperature. The parameter v is also not treated as a fitting parameter but instead as a hyperparameter that has a constant value across all glass compositions and is varied manually over each set of fits of the entire viscosity data set to find the optimal value. This is done to simplify and increase the stability of the fitting process because the value of v has the smallest effect on the quality of the fits. Analytically, the value of v determines the degree of asymmetry of $\psi(\chi)$, where the two-level simplification, $v = 1$, is symmetric. Based on the general behavior of $\log_{10}(\eta)$ vs. χ profiles, regardless of the degree of fragility, we already know that v cannot be negative and is unlikely to be less than unity because the that would indicate a slowing in the rate of change of viscosity as T_g is approached from above. This would be indicated by negative curvature in the profile which has not been reported. A constrained trust-region robust fitting algorithm based on Newton's method is used to fit the model to the viscosity profiles of the oxides glass-formers. Each glass composition is refit 50 times using bounded randomized initial values for the parameters and the fit with the minimum residual squared error for each composition is kept. A range of v-values greater than or equal to unity were tested and found them to minimally affect the quality of the fits. Although changing v does affect the values of the other parameters, with increasing magnitude of v this effect gradually vanishes. Holding all other parameters constant and taking $v = 1$ as the basis for comparison, an increase in the value of v from 1 to 2 results in a 20% increase in the value of $\log_{10}(\eta)$ at the infinite temperature intercept – the location most greatly affected by this change. In comparison, changing the value of v from 6 to 7 only results in a 0.7% increase in $\log_{10}(\eta)$ and by $v = 100$, the percent change is in parts per million. The model appears to converge as v

approaches infinity. Therefore, we adopt the expression for generalized logistic function, $\psi(\chi)$ in limit of the infinite v, namely

$$\lim_{v\to\infty} \psi(\chi) = \lim_{v\to\infty} \left(\frac{1+v}{1+ve^{(v\cdot\beta_g\cdot H(1-\chi))}}\right)^{1/v} = e^{\left(\beta_g\cdot H(X-1)\right)}. \tag{5.16}$$

This limiting behavior approaching an exponential form can be seen in the characteristics the differential form of $\psi(\chi)$, Richard's differential equation, as the value of v is increased in **Figure 5-2**. Using this simplified model for $\psi(\chi)$, we fit all 847 viscosity profiles with our VAFE model. Care is taken to properly constrain the values of $(\ln(h\rho_N) - S_0/k_B)$, ΔS, E_0, ΔE, and H, such that fits become unique and the fit values are physically meaningful.
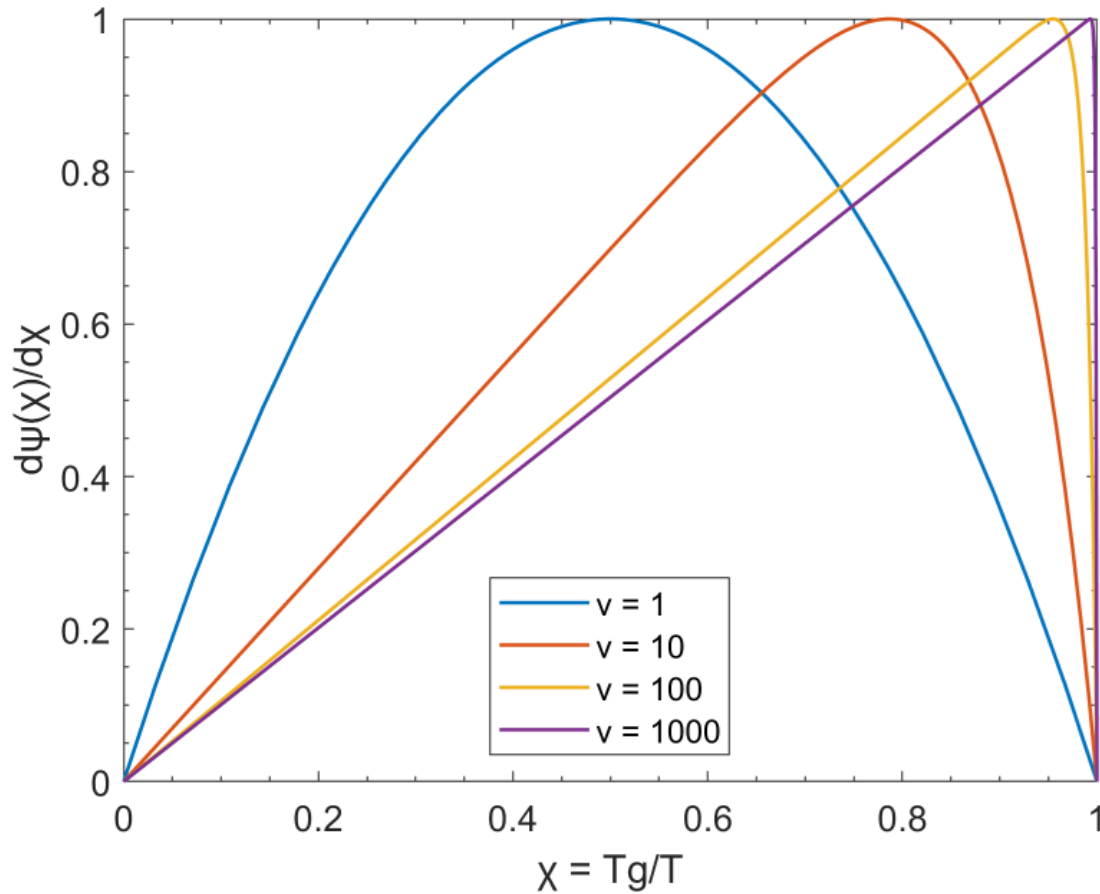
Figure 5-2 The shape of $d\psi(\chi)/d\chi$, Richard's differential equation as the parameter v is increased. The limiting behavior is that of an exponential function.

One such method that has been successful, at least for application within the current oxide glass-former data set, results in a reduction in the number of fitting parameters from 5 down to 3 through enforcing the following relationships:

$$\Delta E = H \cdot \beta_g \cdot E_0, \text{ and} \tag{5.17}$$

$$\frac{\Delta S}{k_B} = H \cdot \beta_g \cdot \left(\frac{S_0}{k_B} - \ln(h\rho_N)\right) \tag{5.18}$$

The rationale for imposing these constraints is that changes in enthalpies and entropies of activation are large only when H, which represents the distinctiveness between the liquid and glassy states, is also large as one would expect for a fragile glass former. The physical basis for this relationship is further discussed below.

5.3 Results and Discussion

In the following, we show a few representative fits of the VAFE model compared with the VFT and MYEGA equations, which have become among the most successful viscosity fitting equations for glass-forming liquids. The VFT equation, or Vogel-Fulcher-Tammann equation, was developed independently in 1920s by the three scientists for which it has been named and is mathematically identical to the later derived Williams-Landel-Ferry (WLF) equation from the field of polymer chemistry.[48–52] These are empirical models that have now been in use for about a century for fitting and interpolating the temperature-dependence of fragile liquids.

$$\log_{10} \eta(\chi) = \log_{10} \eta_0 + \frac{B}{\left(\frac{T_g}{\chi}\right) - T_0} \tag{5.19}$$

The parameters η_0, B, and T_0 set the vertical offset, the scale, and the location of the vertical asymptote for the expression, respectively. The parameter B is sometimes referred to erroneously as an activation energy or instead as a pseudoactivation energy. This measure cannot be thought

137

of as an activation energy in the Boltzman probability sense because the available thermal energy

it is compared to is truncated by T_0 in the denominator of the expression, which results in values

of B being much smaller than activation energies from the perspective of transition-state

theory.[53] To date, despite much effort, T_0 does not appear to have any physical interpretation as it

neither corresponds reliably to the glass transition temperature nor the Kautzmann temperature

and is best thought of simply as a fitting parameter.[54,55] For these reasons, the VFT equation and

its parameters are not likely to provide valuable insight into the physics underlying fragile

behavior and glass-formation.[38] It has also been documented that while the VFT equation

produces good fits for moderately fragile liquids, the quality of fits decrease with increasing

fragility.[28]

The MYEGA equation takes inspiration from the Adam-Gibbs equation, which modifies the

temperature-dependence of the viscosity through scaling with the configurational entropy, which

is also a function of temperature.[56,57] The MYEGA equation modifies this expression by

assuming a different functional form for the configurational entropy based on topological

constraint theory, where the configurational entropy is related to the topological degrees of

freedom per atom and network constraints are considered to be either intact or broken. This

yields the following expression,[58]

$$\log_{10}\eta(\chi) = \log_{10}\eta_\infty + (12 - \log_{10}\eta_\infty) \cdot \chi e^{\left(\left(\frac{m}{(12-\log_{10}\eta_\infty)}-1\right)(\chi-1)\right)} \tag{5.20}$$

The parameters η_∞ and m are the extrapolated infinite temperature viscosity and the kinetic

fragility index (**Equation 5.3**), respectively. The third parameter, T_g, is encompassed by the

parameter $\chi = T_g/T$ in the current expression.

We begin our comparison of the three models by exploring the case for strong glass former in

Figure 5-3. All three models are able to fit the data well. The VAFE and VFT models overlay

one another completely, while the MYEGA model deviates slightly from the others at high

temperatures. The enthalpy and entropy of activation produced from the VAFE model are nearly

constant as expected from a strong glass former.
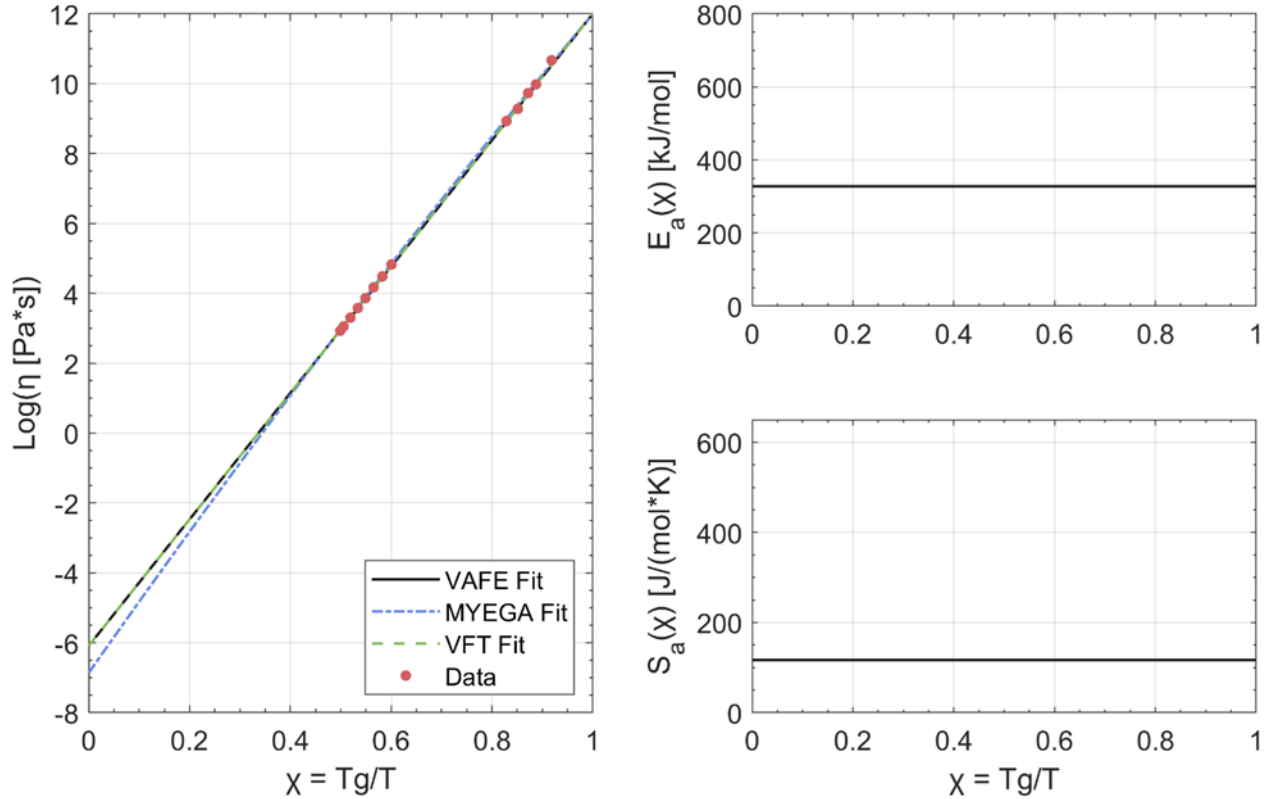
Figure 5-3 Comparison of VAFE (black), MYEGA (blue), and VFT (green) equation fits of viscosity data (red dots) for a strong glass former. The temperature-dependent activation enthalpy, $E_a(\chi)$, and entropy, $S_a(\chi)$, from the VAFE model are shown on the right.

Next, we compare the case of a very fragile glass-former ($m = 103$), shown in **Figure 5-4**. Once

again, all three models fit the data well with a greater level of agreement between the VAFE and

MYEGA equations at lower temperatures. However, at higher temperatures, beginning around

twice T_g, the model predictions begin to disagree to a greater extent. The higher temperature data

is approximately linear, seemingly having entered the Arrhenius regime, but the continued curvature of the MYEGA model produces an almost horizontal line at temperatures greater than $1.67 \cdot T_g$ or values below $\chi = 0.6$. This suggests a viscous activation energy nearing zero within the liquid phase, which should not be the case. Looking at the enthalpy and entropy of activation predicted by the VAFE model, we see large activation barriers near T_g that drop off dramatically with increasing temperature as a result of the highly fragile nature of this glass former. At even higher temperatures, however, the activation energy from the VAFE model remains finite and approaches 80 kJ/mol which is reasonable for a high temperature inorganic glass melt.
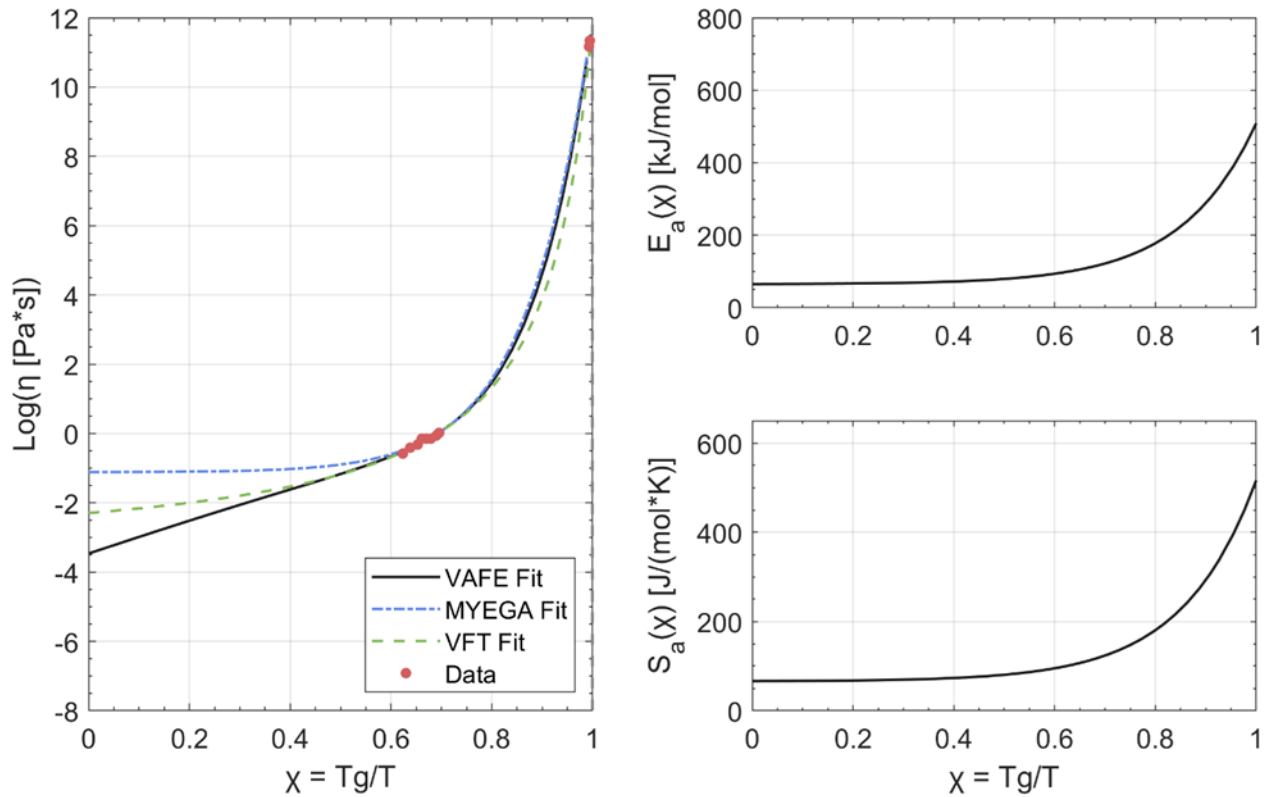
Figure 5-4 Comparison of VAFE (black), MYEGA (blue), and VFT (green) equation fits of viscosity data (red dots) for a fragile glass former. The temperature-dependent activation enthalpy, $E_a(\chi)$, and entropy, $S_a(\chi)$, from the VAFE model are shown on the right.

Lastly, we look at a moderately fragile glass ($m = 41$) in **Figure 5-5**. To fit the higher

temperature data, the MYEGA model overestimates the viscosity values in the low temperature

liquid while the VFT equation underestimates them in this region. Here, the VAFE model

showcases its ability to fit the higher degree of curvature of the low temperature viscosity profile

while still recovering linear behavior that approaches the Arrhenius character of the high

temperature liquid.
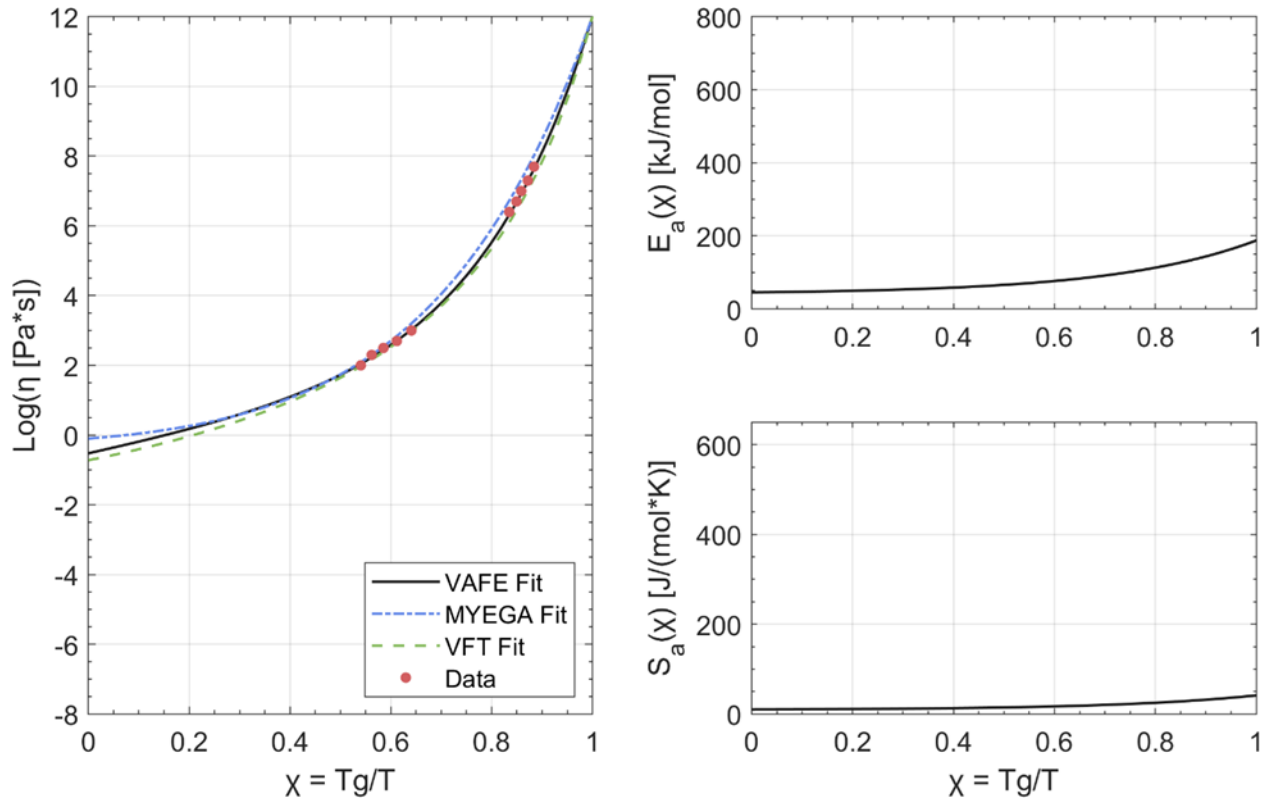
Figure 5-5 Comparison of VAFE (black), MYEGA (blue), and VFT (green) equation fits of viscosity data (red dots) for a glass former of moderate fragility possessing a low activation enthalpy and entropy. The temperature-dependent activation enthalpy, $E_a(\chi)$, and entropy, $S_a(\chi)$, from the VAFE model are shown on the right.

From trends our VAFE model reveals for the oxide glass data fits, and as predicted in the

original Angell plots, the behavior of the viscosity profile for fragile systems appears to regain

Arrhenius type, or linear character in the high temperature liquid regime. The divergence

between our model and the VFT or MYEGA equations at high temperatures originates from the functional form of the models. Our model allows for a return to linearity due to the presence of the E_0 term, while the simple double exponential viscosity dependence of the MYEGA equation enforces either no curvature or continuous curvature throughout the profile. The $e^{1/T}$ type viscosity dependence of the VFT equation allows the profile to approximate linearity at high temperatures but curvature is still present. The flattening of MYEGA profiles at high temperatures insinuates a reduction in activation energy approaching zero, which should not be the case unless the potential energy surface becomes completely flat. The ability to derive meaningful measures from the intercept with the ordinate by extrapolating a model to infinite temperature relies on preserving the phase character of, in this case the liquid. Evidently, the construct is hypothetical, but it is based on the premise that thermal energy is abundant so that the system can overcome all potential energy barriers with unit probability and freely explore all possible microstates. This allows one to focus on the analysis of non-enthalpic contributions to the rate coefficient, such as activation entropy, attempt frequency, geometry factors, etc. Therefore, the microstates must be representative of the physical state and structural description of the material for which the extrapolation is being considered. This means that particles can move without any constraints. The substance still occupies a finite volume commensurate to that of the liquid, particles still interact with one another, and their trajectories cross potential energy wells, whose shape defines the frequencies of fundamental vibrational modes, as often as they pass over the cusps associated with activated states while conquering the repulsive forces of neighboring particles.

While the VAFE concept is designed to account for changes in the energy landscape that result from a system transitioning between glass and liquid, it is also sensitive to the temperature range over which this transition occurs. Beyond the upper bound of this range, when the transformation to liquid is complete, we can assume constancy of structure up to the boiling point, which is consistent with the return to linearity in the temperature dependence of the viscosity. Accordingly, a linear extrapolation towards infinite temperature makes sense for viscosity models of glass-forming liquids, and for data sets extending to sufficiently high temperatures a return to linearity is manifest. Similarly, for our equation that becomes Arrhenius in form for high temperature liquids, its apparent that the energy terms drop out and the infinite temperature intercept is just an indication of the combined values of the characteristic attempt frequency, the high frequency shear modulus, and the entropy of activation for the viscous process in the high temperature liquid.

In **Figure 5-6**, we test the extrapolation robustness of the VAFE model in comparison with the VFT and MYEGA models. This is done by removing the high temperature viscosity data from the profile before fitting each model and then comparing the fits with the full viscosity data set. The data set in **Figure 5-6** is composed of 17 data points. Only the lowest temperature data composing about 35% of the total data set was used for fitting. The fits are identical for all three models for the low temperature data points on which they were fit. However, upon extrapolation it is apparent that neither the VFT nor MYEGA models accurately predict the high temperature data based on low temperature fits. The VFT model underpredicts the viscosity values in the high temperature liquid while the MYEGA model overpredicts the viscosity values.

143
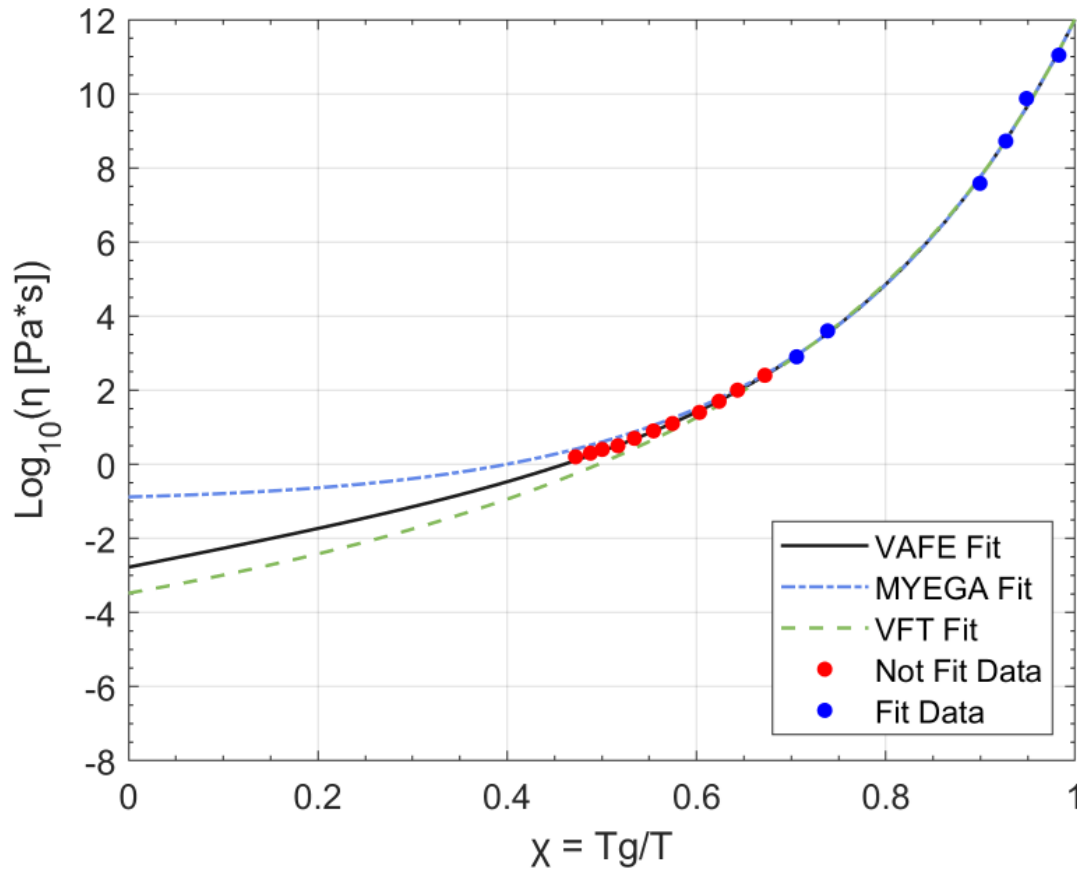
Figure 5-6 Comparison of the robustness of the VAFE (black), MYEGA (blue), and VFT (green) equations to extrapolation. The models have been fit only on the blue data points.

Figure 5-7 shows a distribution of activation enthalpies and entropies for all 847 oxide glass compositions both in the high temperature liquid, E_0 and S_0, and at the glass transition temperature, E_{Tg} and S_{Tg}. Activation enthalpies in the high temperature liquids are centered around 80 kJ/mol with a range from about 35 kJ/mol to just over 300 kJ/mol. At T_g, the enthalpies of activation are centered around 300 kJ/mol but range from around 200 kJ/mol to above 700 kJ/mol. These values fall within reported ranges for viscous activation energies for inorganic glass formers.[59–61] Activation entropies in the high temperature liquid are centered at 40 J/(mol·K) and range from nearly 0 to about 135 J/(mol·K). At T_g, the entropies of activation center around 150 J/(mol·K) with a range from about 30 to 600 J/(mol·K).

144
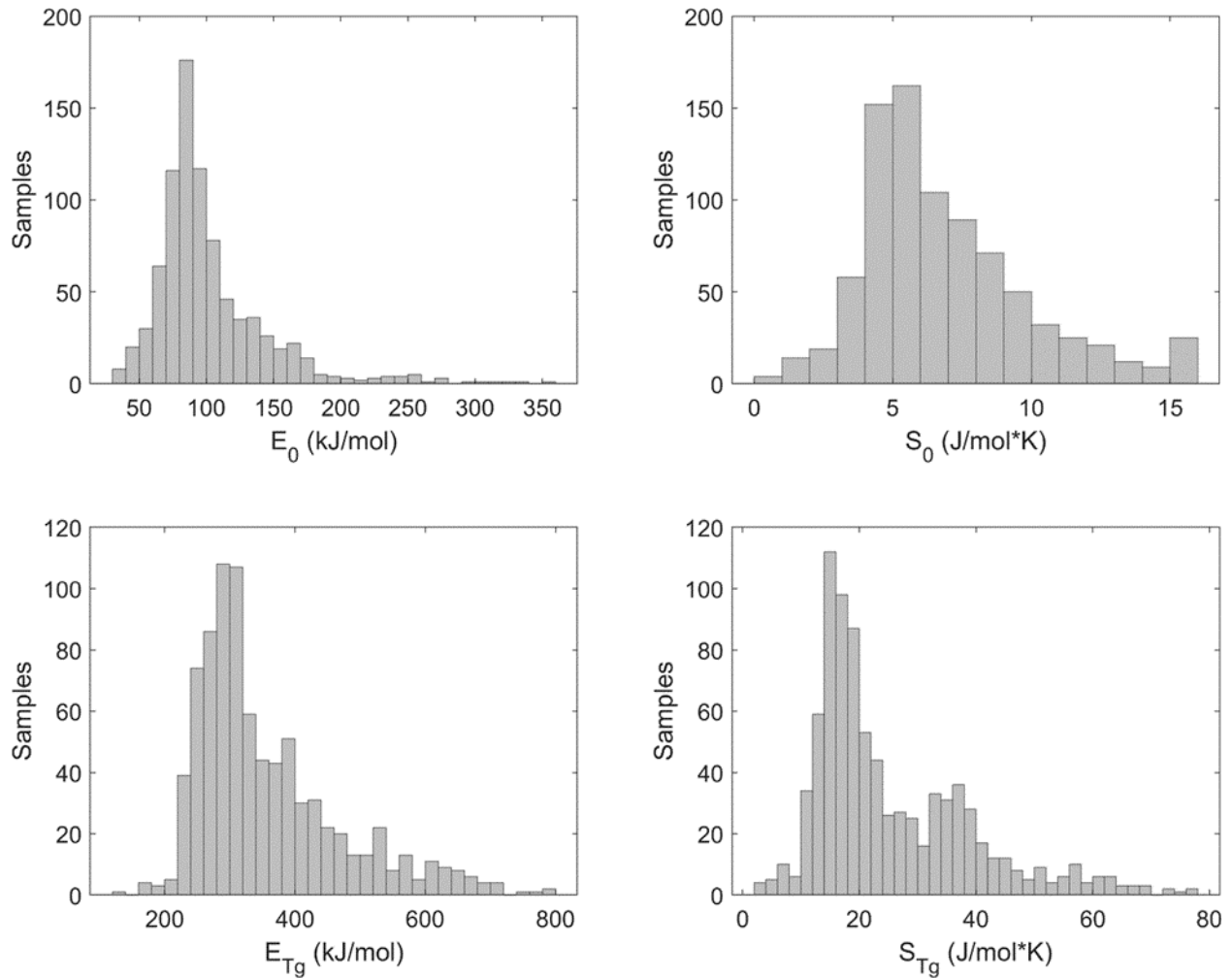
Figure 5-7 The distributions of activation enthalpies and entropies represented by the 847 compositions within the oxide data set. The activated values in the high temperature liquids, E_0 and S_0, are shown as well as values at T_g, E_{Tg} and S_{Tg}.

The effect of activation entropy on the activation free energy for viscosity is significant and should not be ignored.[20] In the VAFE model, we have made the assumption that the activation enthalpy and entropy are both modulated by the function $\psi(\chi)$. This means that while the magnitudes of E_0, ΔE, S_0, and ΔS can all differ as necessary, the temperature dependence of $E_a(\chi)$ and $S_a(\chi)$ overlap identically when scaled and shifted. This assumption produces good fits of the data and meaningful values for the activated quantities. A proportionality relationship between the values of activation enthalpies and activation entropies has been documented numerous times

145

and is often referred to as the Meyer-Neldel rule or the entropy-enthalpy compensation (EEC) effect.[20,62–66]

The infinite temperature intercepts of viscosity profiles are often shown to converge for all glass-forming liquids regardless of fragility.[28,67] However, based on the reasons listed previously about the interpretation of the infinite temperature limit, this is not necessarily true and is unlikely to be realistic. Based on the measured viscosity data we analyzed, such convergence would in many instances require a sign inversion in the slope of the viscosity curves at high temperatures. If we look at the distribution of infinite temperature intercept values in **Figure 5-8** extrapolated from our model, it is quite broad.
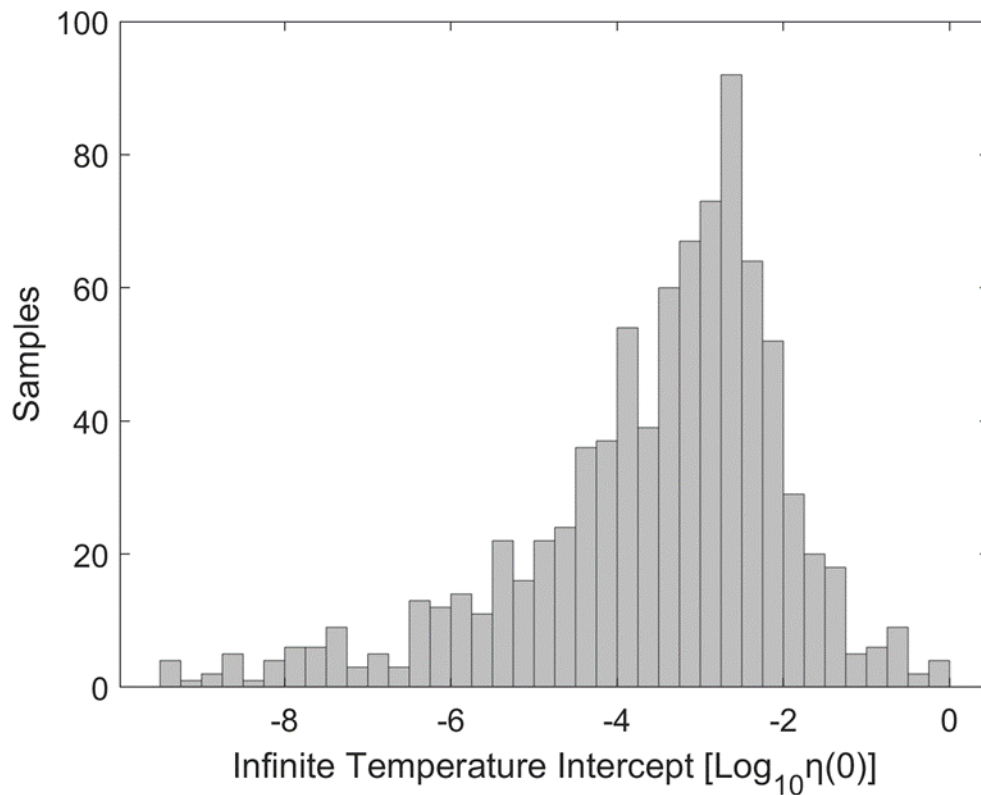
Figure 5-8 Distribution of infinite temperature intercept values for the 847 compositions within the oxide glass data set extrapolated from fits using the VAFE model.

The intercepts result from largely excellent fits of the experimental viscosity data, and even accounting for the magnification of small errors that occur with extrapolation from the terminal high temperature data point, which may exist in some of the fits, the intercept values will not be convergent as is often shown.

The fragility of a glass-forming liquid is most often defined as the slope of the $\log_{10}(\eta)$ vs. T_g/T relationship at the glass transition temperature, as shown in Equation 3. This is a simple metric to calculate, given sufficient viscosity data near T_g or viscosity data at other temperatures and a viscosity model equation. However, in the latter case, the accuracy of the estimation of the fragility index will depend on the successful extrapolation by the model. It is important to point out that this instantaneous slope in the viscosity curve at T_g is intended to describe behavior that is manifest throughout the entire glass transition regime. As such, this metric is relied upon to describe the curvature present across the entire viscosity profile. One should be cautious about the validity of this metric away from the glass transition temperature, however. As discussed previously, the infinite temperature intercepts of these viscosity profiles, representing non-enthalpic properties of the high temperature liquid, do not necessarily converge and therefore the curvature for any given profile, even when normalized as is the case for Angell plots, is not uniquely defined by a locally constructed fragility index m.

The VAFE model produces an alternative metric of fragility that accounts for the magnitude of the non-Arrhenius curvature across the entire viscosity profile. This metric arises directly from the derivation and application of $\psi(\chi)$. The parameters $H \cdot \beta_g$, or explicitly, $H/(k_B T_g)$, is a unitless quantity that goes to zero for a perfectly strong glass former. A correlation plot between $H \cdot \beta_g$ and the fragility index, m, is shown in **Figure 5-9**.

147
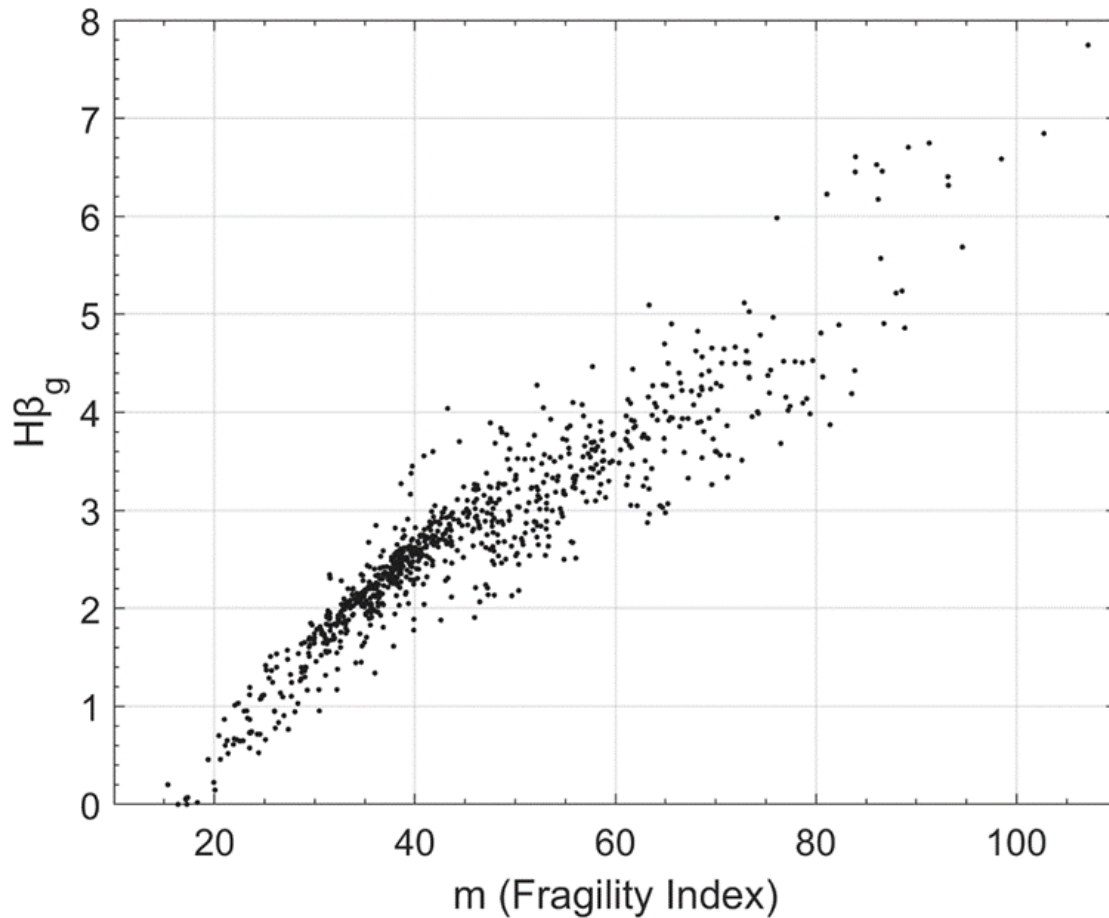
Figure 5-9 Correlation plot comparing the Fragility Index, m, with the parameter $H\beta_g$ of the VAFE model that controls curvature, and therefore the degree of fragility, within the viscosity profile.

The two metrics correlate well for relatively strong glass formers, but the correlation becomes weaker for more fragile glass formers. This is due to the increased variance in the infinite temperature intercept for fragile glass formers and the effect that has on the curvature of the profile, independent of the slope at T_g.

Parameter values that result from VAFE model fits can be utilized to gain insight into the effect of the component speciation and composition of glass forming liquids on the viscous process. E_0 and S_0 can be calculated to yield enthalpies and entropies of activation for high temperature melts, while $H\beta_g$ encodes information about fragility and how the activated values change with

148

temperature down to T_g. This information can be used to better understand what factors are dominant in dictating the viscosity of specific glass forming compositions and how these factors and their sensitivities to changes in temperature vary as a function of composition. For example, **Figure 5-10** shows a comparison of the values of E_0, S_0, and $H\beta_g$ for a mixed alkali borosilicate melt composed of 18 mol% B_2O_3 and 52 mol% SiO_2 while the remaining 30 mol% is varied in increments of 5 mol% between two of the three alkali oxides: Li_2O, Na_2O, and K_2O. Within the composition range available, introduction of a secondary alkali oxide results in an initial increase in the values of E_0 and S_0 and a corresponding decrease in fragility as indicated by $H\beta_g$. However, after this initial increase parameters for the lithium potassium borosilicate remain relatively constant upon increasing Li_2O content with minor increases in fragility. This is unlike the trends for sodium potassium borosilicate and lithium sodium borosilicate in that these glass formers show maximum values in E_0 and S_0 and a minimum in fragility at 15 mol% Na_2O and 10 mol% Li_2O content, respectively. This corresponds to approximately equal concentrations of each alkali species, which is the range in which the mixed alkali effect is typically most apparent. This makes sense, as E_0 increases in greater proportion than the compensating effect of S_0, and simultaneously the fragility decreases to a minimum leading to a more stabilized less atomically mobile glass melt. Evidence of the mixed alkali effect is typically not apparent in high temperature melts when inspecting viscosity *vs*. alkali mole fraction data. At low temperatures, these relationships show a dip in the viscosity for equimolar mixed alkali glasses, but upon increasing temperature this dip becomes shallower until it coincides approximately with viscosity magnitudes of the surrounding alkali compositions.
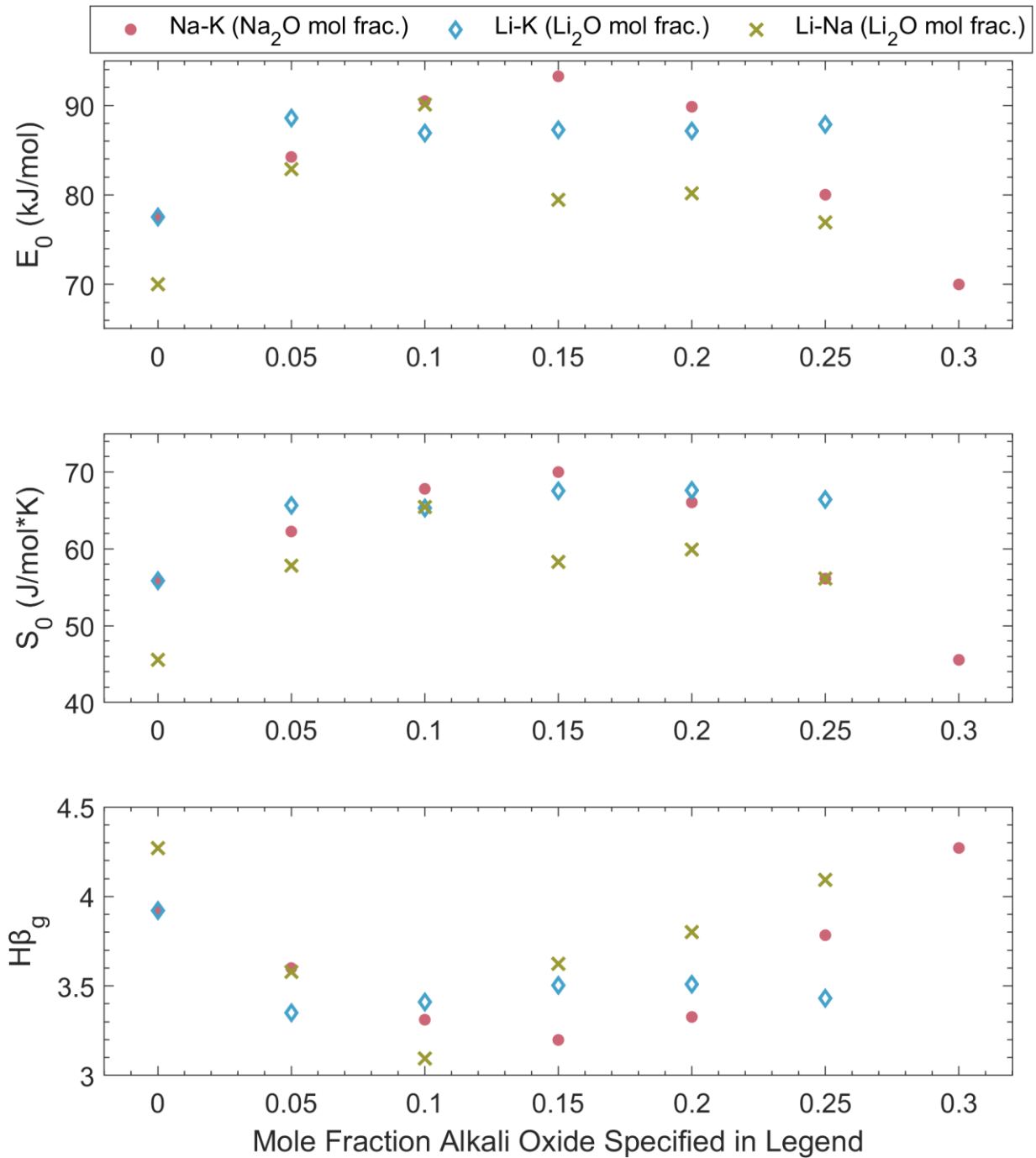
Figure 5-10 Comparison of VAFE model parameters E_0, S_0, and $H\beta_g$ for a mixed alkali borosilicate melt composed of 18 mol% B_2O_3, 52 mol% SiO_2, and 30 mol% alkali oxides. Glass compositions shown are the following: (1) Sodium potassium borosilicate (**dots** represent Na_2O mole fraction), (2) Lithium potassium borosilicate (**diamonds** represent Li_2O mole fraction), and (3) Lithium sodium borosilicate (**X** represents Li_2O mole fraction)

150

This would indicate a higher activation energy for mixed alkali glasses as the viscosity increases more with temperature which is exactly what we see in **Figure 5-10.** This suggests that while the mixed alkali effect appears to diminish with increasing temperature when looking at constant temperature viscosity-composition data, this effect may, in fact, remain even for high temperature melts as observed when inspecting activation energies.

The parameter, H, represents an energy with units of J/mol. For the oxide glass-formers within the data set we analyzed, the magnitude of H varies between approximately 0 and 44.5 kJ/mol or between 0 and 0.46 eV/atom, to better illustrate the argument that follows in view of illustrating the thermophysical meaning of H. Given that the glass transition does not involve phase boundaries, let us consider a generic homogeneous reaction, where a compact and rigid molecular configuration (G) is transformed into a more open and flexible one (L), i.e., $G \rightleftharpoons L$. The equilibrium constant is given by $K = e^{-\beta \Delta G_X} = e^{-\beta \Delta \varepsilon_0} e^{\Delta S_X / k_B}$, where $\Delta \varepsilon_0$ and ΔS_X are the differences in ground state energy and entropy between G and L, respectively. At some temperature T_E the chemical potentials of the two configurations are equal, i.e., $\Delta G_X = 0$, and in a first approximation we can eliminate the entropy term using $\Delta \varepsilon_0 = T_E \Delta S_X$ so that $\beta \Delta G_X = \Delta \varepsilon_0 (\beta - \beta_E)$, where $\beta_E = 1/k_B T_E$. Using the law of mass action, $K = a_L/a_G$, where a_L and a_G are the chemical activities of configurations L and G, respectively, and furthermore assuming ideal mixing behavior of the two species, we can evaluate the molar fraction of the configuration L as

$$x_L = 1 - \frac{1}{1+K} = 1 - \left(1 + e^{-\Delta \varepsilon_0 (\beta - \beta_E)}\right)^{-1}. \tag{5.21}$$

Hence, we obtain the complement of the logistic function, i.e., the vertically inverted expression in **Equation 5.11** for $v = 1$. Indeed, the molar fraction x_G of constituent G is directly described by

151

the logistic function. Accordingly, the parameter H represents a difference in the potential energy of the ground state of the glass and the ground state potential energy of the high temperature liquid.

Note that the vertical scale of the logistic function can be chosen arbitrarily to best match the quantity it is intended to describe. Often it is opted to range from zero to one to represent probabilities. **Figure 5-11** shows two schematics illustrating the ground state ($\varepsilon_{0,X}$) and activated state (ε^*) energy levels for the $G \rightleftharpoons L$ conversion system that is consistent with our VAFE analysis. Each schematic shows two curves: the red one representing the symmetric logistic function, shown here for reference, and the asymmetric blue curve representing the logistic function for a large v -value, which we postulate to represent that glass transition phenomenon more accurately. The reciprocal temperature range to the right of $T_g/T = 1$ is only shown to better differentiate between the curves. Also, for the asymmetric curve β_g is substituted for β_E, and it no longer corresponds to an equipartition between two states. The distance between the curves and the activated state line represents the activation energy for viscous dissipation in the liquid. Hence, the vertical axis is mapped onto a scale ranging from ~0.5 to ~6 eV/atom. Most important to point out is that both symmetric and asymmetric logistic curves are calculated for the same value of H. The uniqueness of this parameter can most easily be understood by considering the limit in which v by far exceeds unity, i.e., $\left(e^{-vH(\beta-\beta_g)}\right)^{1/v} \equiv e^{-H(\beta-\beta_g)}$. Moreover, the factor v has been associated with the chemical activity coefficient γ_i, which relates the chemical activity of species i to its molar fraction according to $a_i = \gamma_i \cdot x_i$.[68,69] This is best illustrated using Richard's differential equation (**Equation 5-8**) focusing on the term $x_i \cdot (1 - x_i^v)$, adapted here for a generic probability variable.
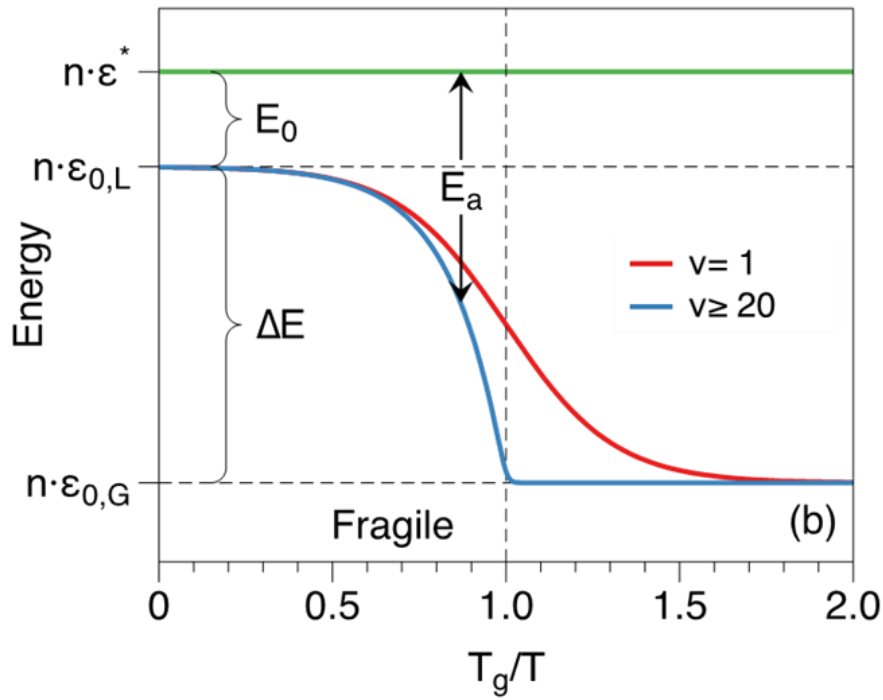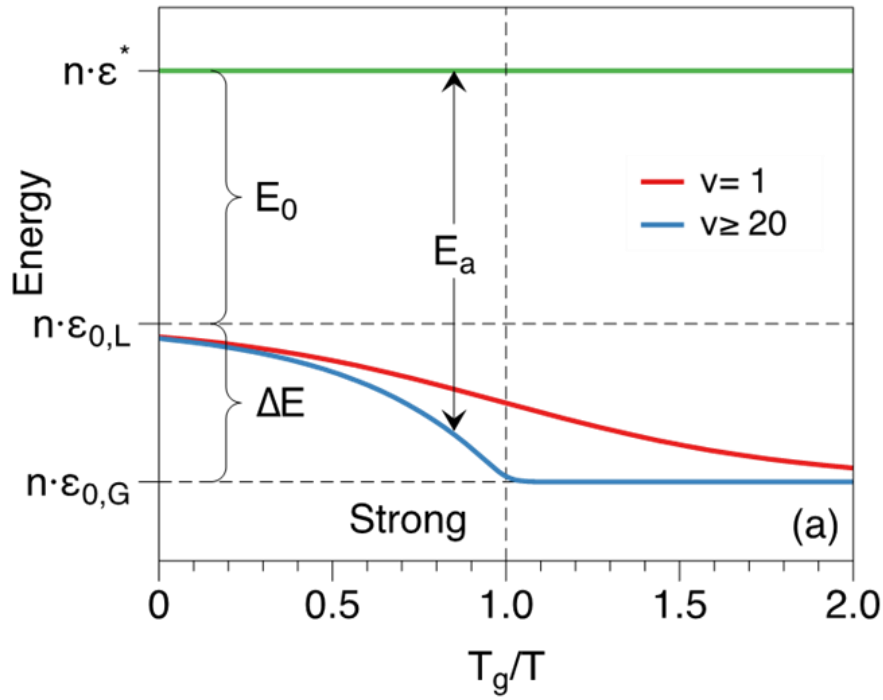
Figure 5-11 Temperature dependence of the ground state and activated state energies for (**a**) a strong and (**b**) a fragile glass forming system, and the relationship activation energy and two of the parameters, E_0 and ΔE of the VAFE model equation. (See text for further explanation of the depicted quantities.

153

Although, the standard thermodynamic definition of $\gamma_i \cdot x_i$. and x_i^ν cannot mathematically be reconciled with one another, they have similar effects on x_i. in that a value $\nu > 1$ suppresses the activity of species i, as does a value of $\gamma_i < 1$. Hence, as ν tends to infinity, the measure that counteracts the growth of species i, namely $(1 - x_i^\nu)$ is suppressed until x_i reaches 1. In other words, the proliferation of species i is self-catalyzed, and therefore grows exponentially. Applying this perspective to the glass transition phenomenon, the exponential growth of the activation free energy for viscous relaxation upon approaching T_g signifies that the smallest structural changes result in the largest increase in activation free energy.

As a glass-forming liquid cools, we expect the energy wells in the potential energy surface to deepen due to more efficient packing and increasingly stabilizing non-bonding interactions, whereas the configurations associated with the activated states may vary less in comparison because atoms that jump between sites must push past neighboring gateway atoms to within similar proximity. While this latter assumption is not crucial to the interpretation of our findings, the temperature-independent ε^*-level drawn in **Figure 5-11** appears to be the least speculative option. It follows that the change in activation energy, i.e., the difference between the ground state and the activated state energies, increase proportionally to $H \cdot \beta_g$, where the scale could be set by the constant baseline activation energy value E_0, which is the sole component remaining for the high temperature liquid. This has been the physical motivation for the constrained form of the VAFE model given by **Equations 5.17** and **5.18**. The relationship put forth so far between H and ΔE may suggest that the value of ΔE should therefore be equal to H. This is not the case. The value of ΔE is typically 10 to 35 times larger than H. This difference is to be expected based on what each energy represents. While H represents the change in the ground-state potential

energies of the entire liquid *vs*. glassy material taken on an average per atom (or molecular constituent) basis, ΔE represents the energy required to elevate those atoms that participate in a single elementary dissipative event of the viscous process from their ground state to the activated state. Hence, the discrepancy in magnitudes has to do with the number of atoms involved in the activated process. If increasing the temperature from just above T_g to well into the liquid domain raises the ground state energy of all atoms by H eV on average, it would reduce the activation energy for viscous dissipation by $n \cdot H = \Delta E$ eV, assuming constant ε^* across that temperature range, where n is the number of atoms participating in (or affected by) the underlying relaxation mechanism. Conversely, the ratio of $\Delta E/H = n$ should yield the number of affected atoms. In fact, our data indicates that in the vicinity of 10 to 50 atoms are involved in the activated process. This range of numbers is corroborated by the findings of a recent investigation of ionic conductivity in mixed network forming glasses. Using Brillouin light scattering (BLS), we discovered a strong correlation between the adiabatic elastic modulus and the activation energy for cation hopping.[70] Elastic moduli have been used in transition-state theory to describe atomic transport in liquids and amorphous materials first by Frenkel and later by Anderson and Stuart.[71,72] This description envisions the cooperation of atoms in the local environment of hopping atom that reversibly spread apart to open a passageway along the trajectory allowing an atom to jump from one stable site to the next. From the comparative analysis of BLS and ionic conductivity data, the activation energy for the hopping event is supplied to the site by a coincidence of overlapping phonons. However, this energy is not focused on the hopping atom alone but on a small region surrounding this atom. This affected volume involves about 30-40 neighboring atoms. Displacements of these neighboring atoms exceeding their normal

155

vibrational motions coincide with the motion of the hopping atom in such a way that it allows for the elementary transport event to take place. The affected volume of the hopping process is calculated by comparing the activation energy (energy per hopping atom) with the adiabatic bulk modulus (energy per volume). The product of the affected volume and the atomic number density gives the number of atoms that participate in the activated hopping process. Interestingly, in the derivation of the MYEGA equation, the configurational entropy of the glass-forming liquid is posited to be a function of the topological degrees of freedom per atom which is calculated as[56]

$$f(T) = 3e^{-\frac{H_{MYEGA}}{k_B T}}.$$

(**5.22**)

The parameter, H_{MYEGA} (the subscript has been added for clarity), is described as the energy difference between intact and broken network constraints. Though this expression is lost from the final MYEGA expression as a result of generalization, the value of H_{MYEGA} can be approximated for compositions within the present oxide data set according to

$$H_{MYEGA} = \left(\frac{m - (12 - \log_{10}\eta_\infty)}{(12 - \log_{10}\eta_\infty)}\right) \cdot k_B T_g.$$

(**5.23**)

This expression makes use of the simplifying assumption that the temperature at which linear behavior is regained, and the activation free energy no longer varies with increasing temperature, is approximately equal to $2 \cdot T_g$. The values of H_{MYEGA} are estimated and compared with values of H from the VAFE equation in a correlation plot in **Figure 5-12**. These values correlate strongly and possess similar magnitudes for the same compositions. Differences in the values likely result from the simplifying assumption in calculating H_{MYEGA} as well as key differences in the mathematical structure of the models. Though these values are arrived at using different methods and frameworks, they likely are describing the same phenomenon.

156
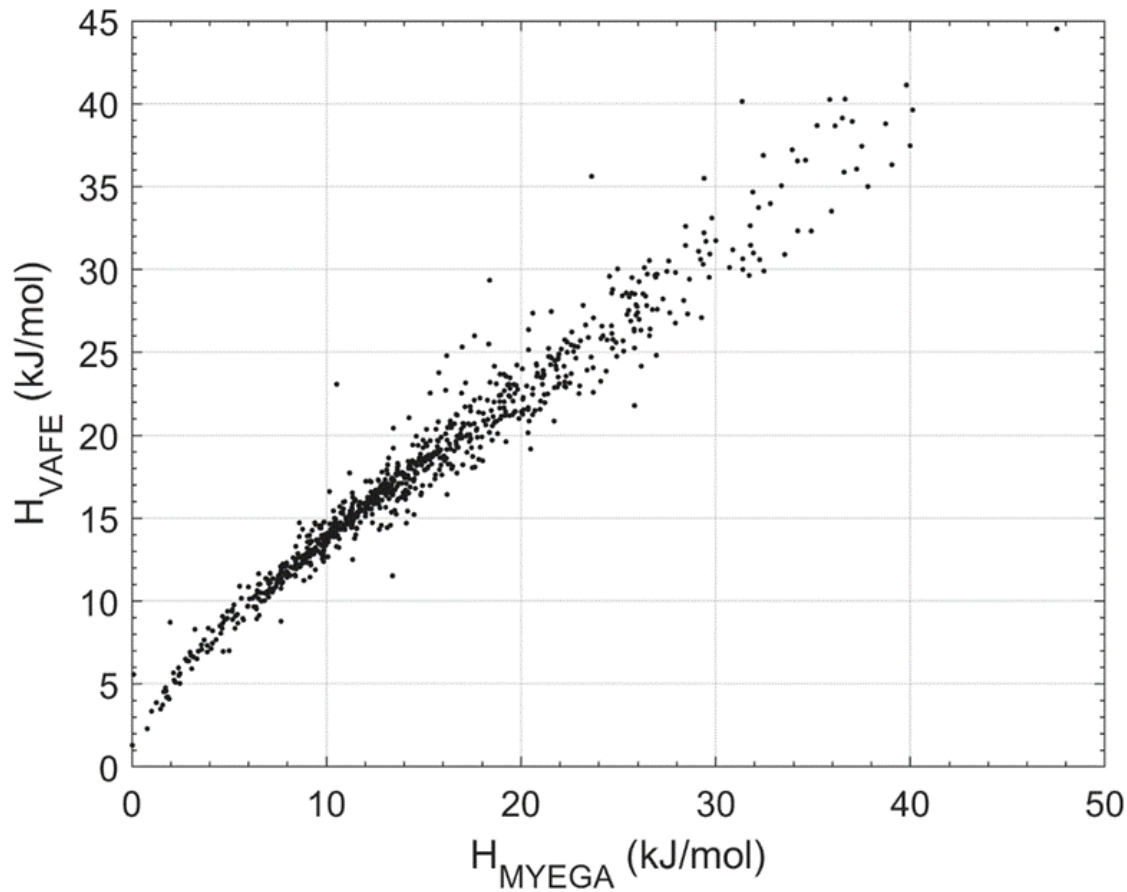
Figure 5-12 Comparison between the *H* value from the VAFE model corresponding to the change in the ground state potential energy of the glass forming liquid and a corresponding H_{MYEGA} calculated from parameters of the MYEGA equation.

Though viewed through the lens of breaking topological constraints, these changes in energy of the glass-forming liquid should be directly evident in the potential energy of the liquid. In fact, the breaking of topological constraints in glass-forming liquids has already been associated with reductions in the energy barriers for relaxation processes.[73–77] This lends credence to the idea that changes in the potential energy surface of the glass-forming liquid, as a result of temperature-mediated effects on relaxation, directly result in modification to viscous activation barriers.

5.4 Conclusions

The ability to reliably predict viscosity is essential for carrying out the physical processing of glass and glass-ceramics products to a high degree of fidelity and a better understanding of what causes such dramatic changes in the structural relaxation rates of glass forming systems may provide insights into the nature of the amorphous state of matter. To date, the underlying reason for the deviation from Arrhenius behavior in the temperature dependence of the viscosity has been a factor of intense scrutiny. Despite the progress made towards the development of theoretical frameworks, categorization, and quantitative tools, the structural and physicochemical origin of this non-Arrhenius behavior remains an open question.

In our earlier publication,[31] we introduced the basic framework of an enhanced descriptive model for viscosity of glass-forming liquids that not only fits experimental data well but produces quantitative and physically meaningful parameters that can be reconciled with long-successful physics-based models such as transition state theory. Based on the same phenomenological approach as pioneered by Eyring, our model takes the structural evolution resulting from traversing the glass transition regime, and thus the variation in the activation barrier, for the viscous process into account. In the present work, we have developed the workflow for analyzing steady-state viscosity data using our new model, reviewing salient points underlying our model and how they factor into the derived formalism and reporting on how our model performs when fitting viscosity data of 847 oxide glass formers.

The form of our VAFE model is essentially the same as Eyring's equation, except that the enthalpy and entropy of activation are temperature-dependent quantities. The modulation of these values with temperature is based on Richard's generalized differential equation, which has

the structure of a generic rate equation. The approach we have taken is both rooted in thermodynamic and kinetic formalisms and can thus be considered as describing the transition from a liquid to a glass (or vice versa) as a reversible rate phenomenon. The function $\psi(\chi)$ determines how the activation enthalpy and entropy change with respect to a change in the temperature, while E_0 and S_0 are static quantities that relate closely to the activation enthalpy and entropy in the high temperature liquid state. The values ΔE and ΔS correspond to the magnitude of change in the activation enthalpy and entropy between the high temperature liquid state and the material at its glass transition temperature.

We compared representative fits of the VAFE model with those of the VFT and MYEGA equations. When fitting a very fragile glass-former ($m = 103$), at high temperatures the model predictions disagree. The higher temperature data is approximately linear, seemingly having entered the Arrhenius regime, but the continued curvature of the MYEGA model produces an almost horizontal line, suggesting a viscous activation energy nearing zero within the liquid phase, which should not be the case. Curvature in viscosity profiles for temperatures extrapolated from the high temperature liquids state should not occur. Upon heating a glass, once the transformation to liquid is complete, we can assume constancy of structure up to the boiling point, which is consistent with the return to linearity in the temperature dependence of the viscosity. The infinite temperature intercept is just an indication of the combined values of the non-enthalpic contributions to the rate coefficient, such as activation entropy, attempt frequency, geometry factors, etc.

We also tested the extrapolation robustness of the VAFE model in comparison with the VFT and MYEGA models by removing the high temperature viscosity data from the profile of a

159

moderately fragile glass former before fitting each model. The fits were then compared with the full viscosity data set. Neither the VFT nor MYEGA models accurately predicted the high temperature data when only fit on low temperature data.

It was demonstrated that VAFE model fits can be utilized to gain insight into the effect of the component speciation and composition of glass forming liquids on the viscous process. Enthalpies and entropies of activation as well as information about fragility and how the activated values change with temperature down to T_g obtained from the model can be used to better understand which factors are dominant in dictating the viscosity of specific glass forming compositions and how these factors and their sensitivities to changes in temperature vary as a function of composition.

The VAFE model also links the temperature-dependent change in potential energy due to structural changes in glass formers to fragility. The parameter H represents a difference in the potential energy of the ground state of the glass and the ground state potential energy of the high temperature liquid. The change in activation energy, i.e., the difference between the ground state and the activated state energies, increase proportionally to $H \cdot \beta_g$, where the scale could be set by the constant baseline activation energy value E_0. The value of ΔE, the change in activation enthalpy, is typically 10 to 35 times larger than H. While H represents the change in the ground-state potential energies of the entire liquid *vs*. glassy material taken on an average per atom (or molecular constituent) basis, ΔE represents the energy required to elevate those atoms that participate in a single elementary dissipative event of the viscous process from their ground state to the activated state. Hence, the discrepancy in magnitudes has to do with the number of atoms

involved in the activated process. Our data indicates that in the vicinity of 10 to 50 atoms are involved in the activated process.

A value, H_{MYEGA}, was estimated from fits using the MYEGA equation and compared with values of H from the VAFE equation The values correlated strongly and possess similar magnitudes for the same compositions. Though these values were arrived at using different methods and frameworks, they likely describe the same phenomenon. The breaking of topological constraints in glass-forming liquids, such as those at the core of the MYEGA equation derivation, has already been associated with reductions in the energy barriers for relaxation processes, like those of the VAFE model.[73–77] This supports that changes in the potential energy surface of the glass-forming liquid, as a result of temperature-mediated effects on relaxation, directly result in modification to viscous activation barriers.

5.5 References

1. Ojo, A. T. & Lee, P. I. A Mechanistic Model for Predicting the Physical Stability of Amorphous Solid Dispersions. *J. Pharm. Sci.* **110**, 1495–1512 (2021).

2. Xu, X. L., Douglas, J. F. & Xu, W. S. Thermodynamic-Dynamic Interrelations in Glass-Forming Polymer Fluids. *Macromolecules* **55**, 8699–8722 (2022).

3. Ohno, H. Functional design of ionic liquids. *Bull. Chem. Soc. Jpn.* **79**, 1665–1680 (2006).

4. Shmukler, L. E., Fedorova, I. V, Fadeeva, Y. A. & Safonova, L. P. The physicochemical properties and structure of alkylammonium protic ionic liquids of RnH4-nNX (n=1-3) family. A mini-review. *J. Mol. Liq.* **321**, 114350 (2021).

5. Tolstikhin, I. & Hofmann, A. W. Early crust on top of the Earth's core. *Phys. Earth Planet. Inter.* **148**, 109–130 (2005).

6. Gonnermann, H. M. Magma Fragmentation. *Annu. Rev. Earth Planet. Sci.* **43**, 431–458 (2015).

7. Freed, K. F. The Descent into Glass Formation in Polymer Fluids. *Acc. Chem. Res.* **44**, 194–203 (2011).

8. Mahato, S., Zhu, Z. W. & Sun, D. W. Glass transitions as affected by food compositions and by conventional and novel freezing technologies: A review. *Trends Food Sci. Technol.* **94**, 1–11 (2019).

9. Valenti, S., Cazorla, C., Romanini, M., Tamarit, J. L. & Macovez, R. Eutectic Mixture Formation and Relaxation Dynamics of Coamorphous Mixtures of Two Benzodiazepine Drugs. *Pharmaceutics* **15**, 196 (2023).

10. Kieffer, J. Structural Transitions in Glasses and Glass-Forming Liquids (Morey Award Lecture). *Ceram. Bull.* **81**, 73–78 (2002).

11. Takamori, T. & Tomozawa, M. Viscosity and Microstructure of Phase-Separated Borosilicate Glasses. *J. Am. Ceram. Soc.* **62**, 373–377 (1979).

12. Kelton, K. F. Kinetic and structural fragility-a correlation between structures and dynamics in metallic liquids and glasses. *J. Physics-Condensed Matter* **29**, 23002 (2017).

13. Yang, M. *et al.* Research progress on high-entropy bulk metallic glasses. *Sci. Sin. Mech. Astron.* **50**, 67003 (2020).

14. Varshneya, A. K. & Mauro, J. C. *Fundamentals of inorganic glasses. Fundamentals of Inorganic Glasses* (2019). doi:10.1016/C2017-0-04281-7.

162

15.   LEWIS, M. H., METCALF-JOHANSEN, J. & BELL, P. S. Crystallization Mechanisms in Glass-Ceramics. *J. Am. Ceram. Soc.* **62**, (1979).

16.   Martendal, C. P. & de Oliveira, A. P. N. Glass viscosity at crystallization temperature: an approach. *J. Therm. Anal. Calorim.* **130**, (2017).

17.   Dubey, K. S., Ramachandrarao, P. & Lele, S. Thermodynamic and viscous behaviour of undercooled liquids. *Thermochim. Acta* **280**, 25–62 (1996).

18.   Sidebottom, D. L. Connecting Glass-Forming Fragility to Network Topology. *Front. Mater.* **6**, 144 (2019).

19.   Wang, L. M., Liu, R. P. & Tian, Y. J. On glass formation thermodynamics: Enthalpy vs. Entropy. *Acta Phys. Sin.* **69**, 196401 (2020).

20.   Xu, W. S., Douglas, J. F. & Sun, Z. Y. Polymer Glass Formation: Role of Activation Free Energy, Configurational Entropy, and Collective Motion. *Macromolecules* vol. 54 (2021).

21.   Eyring, H. Viscosity, plasticity, and diffusion as examples of absolute reaction rates. *J. Chem. Phys.* **4**, (1936).

22.   Rosa, A. C. P., Cruz, C., Santana, W. S., Brito, E. & Moret, M. A. Non-Arrhenius behavior and fragile-to-strong transition of glass-forming liquids. *Phys. Rev. E* **101**, 42131 (2020).

23.   Silva, V. H. C., Aquilanti, V., de Oliveira, H. C. B. & Mundim, K. C. Uniform description of non-Arrhenius temperature dependence of reaction rates, and a heuristic criterion for quantum tunneling vs classical non-extensive distribution. *Chem. Phys. Lett.* **590**, 201–207 (2013).

24.   Angell, C. A. Structural instability and relaxation in liquid and glassy phases near the fragile liquid limit. *J. Non. Cryst. Solids* **102**, (1988).

25.   Angell, C. A. Strong and Fragile Liquids Relaxations in Complex Systems. in *National Technical Information Service, US Department of Commerce* 3–11 (1984).

26.   Angell, C. A., Dworkin, A., Figuiere, P., Fuchs, A. & Szwarc, H. Strong and fragile plastic crystals. *J. Chim. Phys.* **82**, (1985).

27.   Böhmer, R., Ngai, K. L., Angell, C. A. & Plazek, D. J. Nonexponential relaxations in strong and fragile glass formers. *J. Chem. Phys.* **99**, (1993).

28.   Angell, C. A. Formation of glasses from liquids and biopolymers. *Science (80-.).* **267**, (1995).

29.   Arrhenius, S. Über die Reaktionsgeschwindigkeit bei der Inversion von Rohrzucker durch

Säuren. *Zeitschrift für Phys. Chemie* **4U**, (1889).

30.   Böhmer, R. & Angell, C. A. Correlations of the nonexponentiality and state dependence of mechanical relaxations with bond connectivity in Ge-As-Se supercooled liquids. *Phys. Rev. B* **45**, (1992).

31.   Beg, C. & Kieffer, J. Fragility and the rate of change of the energy landscape topography. *J. Non-Crystalline Solids X* **14**, (2022).

32.   Dyre, J. C. Colloquium: The glass transition and elastic models of glass-forming liquids. *Rev. Mod. Phys.* **78**, (2006).

33.   Kivelson, D., Tarjus, G., Zhao, X. & Kivelson, S. A. Fitting of viscosity: Distinguishing the temperature dependences predicted by various models of supercooled liquids. *Phys. Rev. E - Stat. Physics, Plasmas, Fluids, Relat. Interdiscip. Top.* **53**, (1996).

34.   Kivelson, D. & Tarjus, G. SuperArrhenius character of supercooled glass-forming liquids. *J. Non. Cryst. Solids* **235–237**, (1998).

35.   Hecksher, T., Nielsen, A. I., Olsen, N. B. & Dyre, J. C. Little evidence for dynamic divergences in ultraviscous molecular liquids. *Nat. Phys.* **4**, (2008).

36.   Bässler, H. Viscous flow in supercooled liquids analyzed in terms of transport theory for random media with energetic disorder. *Phys. Rev. Lett.* **58**, (1987).

37.   Galimzyanov, B. N. & Mokshin, A. V. A novel view on classification of glass-forming liquids and empirical viscosity model. *J. Non. Cryst. Solids* **570**, (2021).

38.   Ikeda, M. & Aniya, M. Bond strength-coordination number fluctuation model of viscosity: An alternative model for the vogel-fulcher-tammann equation and an application to bulk metallic glass forming liquids. *Materials (Basel).* **3**, (2010).

39.   Han, D., Wei, D., Cao, P. H., Wang, Y. J. & Dai, L. H. Statistical complexity of potential energy landscape as a dynamic signature of the glass transition. *Phys. Rev. B* **101**, (2020).

40.   Sanditov, D. S. Deformation-activation model of viscous flow of glass-forming liquids. *J. Non. Cryst. Solids* **400**, (2014).

41.   Richards, F. J. A flexible growth function for empirical use. *J. Exp. Bot.* **10**, (1959).

42.   Yin, X. *et al.* (Invited) Kinetic Insight into the Degradation Mechanism of PGM-Free ORR Catalysts. *ECS Meet. Abstr.* **MA2018**-**01**, (2018).

43.   Lee, S. Y., Lei, B. & Mallick, B. Estimation of COVID-19 spread curves integrating global data and borrowing information. *PLoS One* **15**, (2020).

44. Hinton, G. *et al.* Deep neural networks for acoustic modeling in speech recognition: The shared views of four research groups. *IEEE Signal Process. Mag.* **29**, (2012).

45. Fermi, E. Sulla quantizzazione del gas perfetto monoatomico. *Rend. Lincei* **3**, (1926).

46. Dirac, P. On the theory of quantum mechanics. *Proc. R. Soc. London. Ser. A, Contain. Pap. a Math. Phys. Character* **112**, 661–677 (1926).

47. Cassar, D. R. ViscNet: Neural network for predicting the fragility index and the temperature-dependency of viscosity. *Acta Mater.* **206**, (2021).

48. Fulcher, G. S. ANALYSIS OF RECENT MEASUREMENTS OF THE VISCOSITY OF GLASSES. *J. Am. Ceram. Soc.* **8**, (1925).

49. Scherer, G. W. Editorial Comments on a Paper by Gordon S. Fulcher. *J. Am. Ceram. Soc.* **75**, (1992).

50. Vogel, H. The law of the relation between the viscosity of liquids and the temperature. *Phys. Z.* **22**, (1921).

51. Tamman, G. & Hesse, W. The dependence of viscosity upon the temperature of supercooled liquids. *Zeitschrift fuer Anorg. und Allg. Chemie* **156**, (1926).

52. Williams, M. L., Landel, R. F. & Ferry, J. D. The Temperature Dependence of Relaxation Mechanisms in Amorphous Polymers and Other Glass-forming Liquids. *J. Am. Chem. Soc.* **77**, (1955).

53. Wang, G. & Kieffer, J. Contiguous High-Mobility Interphase Surrounding Nano-Precipitates in Polymer Matrix Solid Electrolyte. *ACS Appl. Mater. Interfaces* (2022) doi:10.1021/acsami.2c15871.

54. Kauzmann, W. The Nature of the Glassy State and the Behavior of Liquids at Low Temperatures. *Chem. Rev.* **43**, (1948).

55. Diederichsen, K. M., Buss, H. G. & McCloskey, B. D. The Compensation Effect in the Vogel-Tammann-Fulcher (VTF) Equation for Polymer-Based Electrolytes. *Macromolecules* **50**, (2017).

56. Mauro, J. C., Yue, Y., Ellison, A. J., Gupta, P. K. & Allan, D. C. Viscosity of glass-forming liquids. *Proc. Natl. Acad. Sci. U. S. A.* **106**, (2009).

57. Adam, G. & Gibbs, J. H. On the temperature dependence of cooperative relaxation properties in glass-forming liquids. *J. Chem. Phys.* **43**, (1965).

58. Boolchand, P., Lucovsky, G., Phillips, J. C. & Thorpe, M. F. Self-organization and the physics of glassy networks. *Philos. Mag.* **85**, 3823–3838 (2005).

59.   Qin, Q. & McKenna, G. B. Correlation between dynamic fragility and glass transition temperature for different classes of glass forming liquids. *J. Non. Cryst. Solids* **352**, (2006).

60.   Doremus, R. H. Viscosity of silica. *J. Appl. Phys.* **92**, (2002).

61.   Mauro, J. C., Kurkjian, C. R., Gupta, P. K. & Kob, W. Viscosity of silica and doped silica melts: evidence for a crossover temperature. *J. Am. Ceram. Soc.* **105**, (2022).

62.   Psurek, T., Soles, C. L., Page, K. A., Cicerone, M. T. & Douglas, J. F. Quantifying changes in the high-frequency dynamics of mixtures by dielectric spectroscopy. *J. Phys. Chem. B* **112**, (2008).

63.   Yelon, A., Movaghar, B. & Branz, H. M. Origin and consequences of the compensation (Meyer-Neldel) law. *Phys. Rev. B* **46**, (1992).

64.   Dyre, J. C. A phenomenological model for the meyer-neldel rule. *J. Phys. C Solid State Phys.* **19**, (1986).

65.   Liu, L. & Guo, Q. X. Isokinetic relationship, isoequilibrium relationship, and enthalpy-entropy compensation. *Chemical Reviews* vol. 101 (2001).

66.   Gelin, S., Champagne-Ruel, A. & Mousseau, N. Enthalpy-entropy compensation of atomic diffusion originates from softening of low frequency phonons. *Nat. Commun.* **11**, (2020).

67.   Debenedetti, P. G. & Stillinger, F. H. Supercooled liquids and the glass transition. *Nature* vol. 410 (2001).

68.   Papp, K. *et al.* Absolute Quantitation of Serum Antibody Reactivity Using the Richards Growth Model for Antigen Microspot Titration. *Sensors* **22**, 3962 (2022).

69.   Prechl, J., Papp, K., Kovacs, A. & Pfeil, T. The Binding Landscape of Serum Antibodies: How Physical and Mathematical Concepts Can Advance Systems Immunology. *Antibodies* **11**, 43 (2022).

70.   Wang, W., Christensen, R., Curtis, B., Martin, S. W. & Kieffer, J. A new model linking elastic properties and ionic conductivity of mixed network former glasses. *Phys. Chem. Chem. Phys.* **20**, 1629–1641 (2018).

71.   MacDougall, F. H. Kinetic Theory of Liquids. By J. Frenkel. *J. Phys. Colloid Chem.* **51**, (1947).

72.   ANDERSON, O. L. & STUART, D. A. Calculation of Activation Energy of Ionic Conductivity in Silica Glasses by Classical Methods. *J. Am. Ceram. Soc.* (1954) doi:10.1111/j.1151-2916.1954.tb13991.x.

73.   Bauchy, M. Topological Constraint Theory and Rigidity of Glasses. in *21st Century Nanoscience – A Handbook* (2019). doi:10.1201/9780367333003-13.

74.   Krishnan, N. M. A. *et al.* Enthalpy landscape dictates the irradiation-induced disordering of quartz. *Phys. Rev. X* **7**, (2017).

75.   Mauro, J. C. & Smedskjaer, M. M. Minimalist landscape model of glass relaxation. *Phys. A Stat. Mech. its Appl.* **391**, (2012).

76.   Naumis, G. G. Energy landscape and rigidity. *Phys. Rev. E - Stat. Nonlinear, Soft Matter Phys.* **71**, (2005).

77.   Lacks, D. J. Energy landscapes and the non-newtonian viscosity of liquids and glasses. *Phys. Rev. Lett.* **87**, (2001).

Chapter 6 Summary and Future Directions

6.1 Research Summary

In this work, we explore atomic-scale transport properties in glasses and glass forming liquids. Focusing on the mechanistically similar phenomena of ion diffusion and viscous processes, we leverage the use of computational investigation methods and analysis of experimental data sets to gain new insights and develop a phenomenologically descriptive model of these behaviors. The goals of this research include: (1) contributions toward the knowledge of ionic mobility in glasses for the development of next-generation solid-state electrolyte batteries, improving on the safety, performance, and lifespan of the current technology with applications ranging from mobile electronics and electric vehicles to supporting infrastructure for a renewable energy grid and (2) advancements in our understanding of the glass transition phenomenon through improvements in viscosity modeling of glass formers to support the development and manufacturing of novel glasses. A ubiquitous feature of thermally activated transport processes, such as ionic conductivity and viscosity, in glass forming materials is their non-Arrhenius temperature dependence above T_g. Developing a framework for how changes in the free energy topography associated with the structure of these glassy materials control these processes is vital to their understanding. This is a common thread throughout this work.

In the second chapter, we use MD simulations to study atomic transport in a simple model system consisting of a covalently bonded species that forms a continuous three-dimensional network and mobile species that occupies and moves about the interstices of this network. This

approach reduces the structural complexity from that of actual materials that are being

considered as potential solid electrolytes, with the expectation to expose the essential attributes

of atomic mobility. By systematically varying the size of the mobile solute particles, while

keeping that of carbon in the supporting structure constant, different diffusive regimes have been

identified. The thermodynamic quantity best associated with variation in diffusive behavior is the

internal pressure of the system. For our analysis, we define a nominal packing fraction, f_s, as, a

quantitative metric for solute particle size where high packing fractions correspond to larger

solute particles and vice versa. Descending from high to low f_s, the internal pressure decreases

from positive values, where each solute particle overfills its interstice, to negative values, where

solutes experience a net tensile pull from the carbons. The internal tensile limit is crossed at the

pressure minimum, below which the solute detaches at least from some of the supporting

network elements. For as long as the curvature in the internal pressure vs. packing fraction is

positive, fluctuations in the solute sub-system density would tend to reconstitute the cohesive

state. Below the inflection point, the solute sub-system tends towards separation. We find that

solute diffusivity starts to rise at the inflection point in the pressure *vs*. f_s. The vibrational

spectrum for the configuration at this point is indicative of the particle motions exploring

locations on the potential energy surface characterized by highly anharmonic particle dynamics.

The onset of solute diffusion coincides with the maximum in the compressibility vs. f_S curve.

Furthermore, the solute mobility peaks when (1) the compressibility is negative, i.e., as the free

volume available to the solute increases (corresponding to a shrinking solute size) the pressure in

the system increases (corresponding to a reduction in tensile stress due to decohesion between

solute and network elements), and (2) decohesion is self-catalyzed because the compressibility

becomes more negative with decreasing atomic packing fraction, i.e., the increase in free volume

is accompanied by decreasing changes in the tensile stress due to distance-related reduction in solute-network interactions. However, further reduction in solute packing fraction causes particle mobility to rapidly plunge, because the solute adheres to the facet of network interstice. Hence, the optimal condition for high solute mobility is a potential energy surface characterized by extensive anharmonicity and strong but not complete solute-network decohesion.

In the third chapter, we expand this investigation to the physically more realistic system of a sodium silicate glass, modeled using the ReaxFF reactive potential for our MD simulations. The circumstances envisioned here also have the potential for implementation in the experimental laboratory. We explore the efficacy of increasing the local volume available to diffusing sodium ions on their mobility within a solid-state electrolyte. First, we simulate the ion-exchange of cesium with sodium in a melt-quench formed cesium silicate glass. We compare these results to those obtained for simulated melt-quenched sodium silicate and cesium silicate glasses. The ion-exchanged sodium silicate exhibits 4.5 to 6 times higher sodium cation diffusivities than the melt-quenched sodium silicate glass, so long as the ion exchange is performed on samples below their glass transition temperature. The increases in sodium ion mobility appear to be associated with an increase in free volume within the ion-exchange glasses which are 13% to 15% less dense than their melt-quenched counterparts at the same temperature. To directly probe the effect of increasing free volume on ion mobility, we also explore the effect of applying of an isotropic volumetric strain to a melt-quenched sodium silicate glass. The sodium ion mobility increases significantly with increasing volumetric strain for strains between 0 and 0.25. Upon exceeding these strains, diffusivities begin to decrease with increasing strain. As revealed by the trends in the potential energy as a function of strain, this reversal in the cation diffusivity occurs because the network bonds begin to break, no longer increasing volume uniformly within the structure

170

and instead creating cavities in the structure that inhibit diffusion. In these glasses, oxygen atoms tend to be under compressive stress while sodium and silicon tend to be under tension. There is a reduction in tensile stress on sodium when the glass is volumetrically strained. This results from weakened ionic bonding with surrounding oxygen atoms and facilitates sodium ion hopping due to the decreased energy required to escape their potential wells. Ion-exchange of a large ionic species with a similarly charged smaller species results in enhanced ionic conduction so long as the structure is able to resist densification. The mechanism of mobility enhancement for an ion-exchanged glass is similar to that of a volumetrically strained glass in that the tensile stress on sodium ions is reduced and undulations in the potential energy surface are attenuated. Our findings suggest that low temperature ion-exchange, replacing a large modifier cation with a smaller one, is a viable strategy for improving ionic conductivity in solid-state electrolytes based on robust inorganic glasses that are stable against volume relaxation.

In the fourth chapter, we transition to analyzing experimental sodium borate glass viscoelastic data and develop an enhanced viscoelastic model based on the Maxwell-Wiechert (MW) model. Based on previous observations of changes in the potential energy topography with temperature, this indicates corresponding structure-mediated changes in the activation energy of viscoelastic processes. Brillouin light scattering spectroscopy provides access to unique materials characteristics of glass forming systems, namely the adiabatic complex mechanical modulus as a function of temperature across the glass transition. A description of mechanical response for the sodium borate glass using the MW model for viscoelasticity indicates that the two components of the complex modulus do not observe the Kramers-Kronig transformation. However, this discrepancy can be eliminated by accounting for a temperature dependence of the static modulus, modeled using the logistic function, which has the storage modulus grow larger as the system

transitions from a liquid to glass on account of the structural changes that occur during this process. With this correction, the high-frequency complex modulus is well described. However, when converting the loss modulus to viscosity, and extrapolating the MW expression to zero frequency, it only fits the viscosity obtained using rotating cylinder viscometry asymptotically in the high-temperature limit. To reconcile this data, we must consider that the relaxational moduli and, importantly, the activation energies for viscous dissipation for all Maxwell elements, since the two quantities are correlated, also exhibit a temperature dependence. Only then, using a similarly parameterized logistic function to describe this temperature dependence, can we achieve a satisfactory description of the zero-frequency viscosity. Hence, the structural changes in the glass transition regime not only affect the static modulus, but all mechanical responses of the supercooled liquid structure, which includes the activation energies for atomic motion, as these rely on elastic deformations of their surroundings. Note that the activation free energy is strictly a feature of the energy landscape, namely the difference between the free energy of the activated complex and that of the ground state. Then, because the deviation from Arrhenius behavior of the viscosity is a direct consequence of the change in activation energies and entropies with temperature, the fragility of a glass forming liquid can be regarded as a measure of the rate of change with temperature in the energy landscape topography.

Building on this basic framework of an enhanced descriptive model for viscosity of glass-forming liquids that not only fits experimental data well but produces quantitative and physically meaningful parameters, in chapter 5 we have develop the workflow for analyzing steady-state viscosity data using our new model. We review salient points underlying our model and how they factor into the derived formalism and report on how our model performs when fitting viscosity data of 847 oxide glass formers. The form of our variable activation free energy

(VAFE) model is essentially the same as Eyring's long successful equation, except that the enthalpy and entropy of activation are temperature-dependent quantities based on Richard's generalized differential equation, which is used to describe the transition from a liquid to a glass (or vice versa) as a reversible rate phenomenon. We compare the performance of the VAFE model with those of the established VFT and MYEGA equations and find our model to be more robust to extrapolation and possessing more reasonable behavior in the infinite-temperature, which is just an indication of the combined values of the non-enthalpic contributions to the rate coefficient, such as activation entropy, attempt frequency, geometry factors, etc. We demonstrate that VAFE model fits can be utilized to gain insight into the effect of the component speciation and composition of glass forming liquids on the viscous process. Enthalpies and entropies of activation as well as information about fragility and how the activated values change with temperature down to T_g obtained from the model can be used to better understand what factors are dominant in dictating the viscosity of specific glass forming compositions and how these factors and their sensitivities to changes in temperature vary as a function of composition. The VAFE model also links the temperature-dependent change in potential energy due to structural changes in glass formers to fragility. From the model, the parameter H represents the change in the ground-state potential energies of the entire liquid *vs*. glassy material taken on an average per atom (or molecular constituent) basis, and ΔE represents the energy required to elevate those atoms that participate in a single elementary dissipative event of the viscous process from their ground state to the activated state. These parameters have a discrepancy in magnitudes equivalent to the number of atoms involved in the activated process. This allows us to calculate that in the vicinity of 10 to 50 atoms are involved in these activated processes.

6.2 Future Directions: Ion Mobility in Solid-State Electrolytes

Results of our research indicate that low temperature ion-exchange of a large modifier cation with a smaller one is a viable strategy for improving ionic conductivity in solid-state electrolytes. However, significant volume relaxation after the exchange has occurred diminishes the gains in conductivity. The use of more robust inorganic glass compositions with a greater degree of stability against volume relaxation for ion-exchange is a research direction worth pursuing. It is likely the expanded volumes associated with these ion-exchanged glasses may be retained to a greater extent for glass compositions containing multiple network formers some of which, like boron, can incorporate alkali oxides with a lower than commensurate degree of network depolymerization due the formation of four-coordinated boron. Glasses of this type may be more resistant to structural changes initiated by exchanging differently sized ions. This research can be pursued experimentally, which will of course come with its own challenges with respect to synthesizing good glass samples as well as design and iteration of the low temperature ion-exchange method to receive the highest exchange ratio at low enough temperatures to impede thermally initiated structural reconfigurations. As for continued computational investigations to support this research, such as the use of MD simulations, this will require the incorporation of improved methods in the melt-quenching of glasses. Currently, MD generated glasses are known to not produce the correct network unit speciation, Q^n distributions, where n is the number of bridging oxygen atoms attached to the network cation, that deviate significantly from those characterized in experimental glass samples. We have seen this in our own simulations using both our own in-house reactive force field, FLX, and the ReaxFF force field. This has also been reported in the literature.[1–6] The Q^n distribution is especially important for the mixed-network former (MNF) glasses discussed here because it is directly related to the incorporation of alkali

174

oxides and corresponding degree of network depolymerization that will affect the glass's

stability and resistance to volume relaxation upon ion-exchange. The reason for the inaccuracy in

the Q^n distribution for MD generated glasses is often hypothesized to result from the rapid

quench rates, on the order of 1 K/ps, and not the interatomic potential used. The hyper-quenching

of MD melt-quenched glasses is thought to produce these anomalous network unit distributions

for the same reason that produce glasses with higher fictive temperatures than real glass samples,

because the atoms composing the structure are not able reconfigure to the degree necessary to

settle into the lower energy conformations present in real glasses on timescales attainable for MD

simulations.[1–3,5,6] It has been suggested that the use of a thermostat based not only on the kinetic

temperature but also on the configurational temperature, which is defined in terms of the

derivatives of the potential energy as opposed to the kinetic energy, could yield more realistic

structures.[7–10]

I believe another worthy pursuit to build on the research reported in this work is the continued

development of an analysis framework for the velocity auto-correlation function (VACF) and

vibrational density of states (VDOS) incorporating the use of Prony's method, described in the

last section of Chapter 1. The method, as described in the chapter is inadequate for extracting

reliable information related to ionic diffusion due to the large number of Lorentzian terms

required and the poor fits at the zero-frequency intercept of the VDOS. However, this method

may be improved upon by incorporating details from the analysis reported in Chapter 2 revealing

the presence of higher harmonic frequency peaks associated with a lower fundamental

vibrational frequency, the number and intensity of which depend on the anharmonicity of the

potential energy surface affecting the particle motion. Next steps in the development of this

analysis framework would involve devising a process by which to build on Prony's method by

efficiently and reliably fitting sets of Lorentzian functions that are integer multiples of chosen

fundamental frequencies present in the low frequency portion of the VDOS.

6.3 Future Directions: Viscosity of Glass Forming Systems

The success of our VAFE model is demonstrated in Chapters 4 and 5 of this work. An area of

further analysis that is likely to be fruitful is a thorough investigation of the relationship between

composition and the physically meaningful model parameters yielding information about the

activation enthalpies, activation entropies, the temperature-dependent variation of these

quantities, and the value of H indicating the magnitude of change in the ground-state potential

energy between the high temperature liquid and glassy state. This analysis would contribute to a

better understanding of what factors are dominant in dictating the viscosity of specific glass

forming compositions and how these factors and their sensitivities to changes in temperature

vary with glass composition. This information could be used to simplify the selection of glass

compositions for engineering applications based on an improved understanding of how each

component of the glass affects the viscoelastic behavior of the glass during and after processing.

Another avenue of continued research and development of the VAFE model is pursuing an

improved model fitting methodology. The iteration of the VAFE model applied to the oxide

glass former viscosity data set in Chapter 5 requires that the model be reduced in complexity

from 5 parameters down to 3 parameters leveraging an apparent relationship between the change

in the activated values and the change in the ground-state potential energy. While this enforced

relationship both reduces complexity ensuring that the model parameter fits are unique and

intuitive and results in good fits of the data, it also introduces a well-motivated but potentially

physically unrealistic dependency. To both independently test the validity of this relationship and

possibly improve upon the VAFE model fits in the event that this relationship does not strictly

hold. Initial steps towards developing and implementing a new model fitting method has already begun within our research group at the time of writing. This method involves utilizing parameter values from fitting the 3-parameter version of the VAFE model on the oxide dataset used in Chapter 5 as a starting point. These parameters are used to generate plausible distributions of values for each of the original 5 parameters. From these distributions combinations of parameter values are selected to generate a large synthetic dataset of parameter values. The synthetic dataset generation is constrained such that each combination of parameters must enforce a T_g value that corresponds to a viscosity of 10^{12} Pa•s and ensure that the generated viscosity profile possesses no negative curvature. This synthetic data set is used to train a neural network to effectively fit viscosity data for glass formers and produce accurate parameters values for the 5-parameter VAFE model. This type of neural network physical model parameter estimation has been successful in applications for nonlinear model fitting across multiple fields.[11–15] The success of this method for the application discussed here remains to be seen, but initial results indicate that the final five-parameter fits yield parameter values that are decoupled from the those obtained using the three-parameter constrained interpolation fits. With that, the potential exists for uncovering new physically meaningful relationships between the high temperature melt enthalpy and entropy of activation, the magnitude of change in the activation enthalpy and entropy between liquid and glass transition, and the fragility (apparently relating to changes in the ground-state potential energy throughout the glass transition regime) progressing one step further toward uncovering the essential characteristics of the glass transition phenomenon.

6.4 References

1.	Voigt, U., Lammert, H., Eckert, H. & Heuer, A. Cation clustering in lithium silicate glasses: Quantitative description by solid-state NMR and molecular dynamics simulations. *Phys. Rev. B - Condens. Matter Mater. Phys.* (2005) doi:10.1103/PhysRevB.72.064207.

2.	Deng, L. *et al.* Structural features of sodium silicate glasses from reactive force field-based molecular dynamics simulations. *J. Am. Ceram. Soc.* (2020) doi:10.1111/jace.16837.

3.	Adkins, L. & Cormack, A. Large-scale simulations of sodium silicate glasses. in *Journal of Non-Crystalline Solids* (2011). doi:10.1016/j.jnoncrysol.2011.03.012.

4.	Machacek, J., Gedeon, O. & Liska, M. Group connectivity in binary silicate glasses. *J. Non. Cryst. Solids* (2006) doi:10.1016/j.jnoncrysol.2006.01.036.

5.	Yu, Y., Wang, B., Wang, M., Sant, G. & Bauchy, M. Reactive Molecular Dynamics Simulations of Sodium Silicate Glasses — Toward an Improved Understanding of the Structure. *Int. J. Appl. Glas. Sci.* (2017) doi:10.1111/ijag.12248.

6.	Li, X. *et al.* Cooling rate effects in sodium silicate glasses: Bridging the gap between molecular dynamics simulations and experiments. *J. Chem. Phys.* (2017) doi:10.1063/1.4998611.

7.	Travis, K. P. & Braga, C. Configurational temperature control for atomic and molecular systems. *J. Chem. Phys.* (2008) doi:10.1063/1.2815768.

8.	Beckedahl, D., Obaga, E. O., Uken, D. A., Sergi, A. & Ferrario, M. On the configurational temperature Nosè-Hoover thermostat. *Phys. A Stat. Mech. its Appl.* (2016) doi:10.1016/j.physa.2016.05.008.

9.	Patra, P. K. & Bhattacharya, B. A deterministic thermostat for controlling temperature using all degrees of freedom. *J. Chem. Phys.* (2014) doi:10.1063/1.4864204.

10.	Jepps, O. G., Ayton, G. & Evans, D. J. Microscopic expressions for the thermodynamic temperature. *Phys. Rev. E - Stat. Physics, Plasmas, Fluids, Relat. Interdiscip. Top.* (2000) doi:10.1103/PhysRevE.62.4757.

11.	Dufera, T. T., Seboka, Y. C. & Fresneda Portillo, C. Parameter Estimation for Dynamical Systems Using a Deep Neural Network. *Appl. Comput. Intell. Soft Comput.* **2022**, (2022).

12.	Samad, T. & Mathur, A. Parameter estimation for process control with neural networks. *Int. J. Approx. Reason.* **7**, (1992).

13.	Annaswamy, A. M. & Yu, S. H. θ-adaptive neural networks: A new approach to parameter estimation. *IEEE Trans. Neural Networks* **7**, (1996).

14.	Grimm, V., Heinlein, A., Klawonn, A., Lanser, M. & Weber, J. Estimating the time-

dependent contact rate of sir and seir models in mathematical epidemiology using physics-informed neural networks. *Electron. Trans. Numer. Anal.* **56**, (2021).

15.   Wei, Y. & Jiang, Z. Estimating Parameters of Structural Models Using Neural Networks. *SSRN Electron. J.* (2019) doi:10.2139/ssrn.3496098.